A Multiscale In Silico Study to Characterize the Atrial Electrical Activity of Patients With Atrial Fibrillation

A Translational Study to Guide Ablation Therapy

Zur Erlangung des akademischen Grades eines

DOKTORS DER INGENIEURWISSENSCHAFTEN (Dr.-Ing.)

von der KIT-Fakultät für

Elektrotechnik und Informationstechnik

des Karlsruher Instituts für Technologie (KIT)

genehmigte

DISSERTATION

von

Jorge P. Sánchez Arciniegas, M.Sc.

geb. in Quito, Ecuador

Tag der mündlichen Prüfung:	24. Juni 2021
Referent:	Prof. Dr. rer. nat. Olaf Dössel
Korreferent 1:	Dr. Beatriz Ana Gomis Trenor
Korreferent 2:	Dr. Francisco Javier Saiz Rodriguez

Karlsruhe Institute of Technology

UNIVERSITAT POLITÈCNICA DE VALÈNCIA

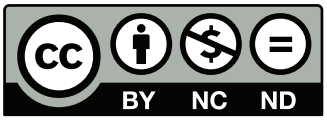

This doctoral thesis was carried out as a collaboration between the Institute of Biomedical Engineering (IBT) at the Karlsruher Institut für Technologie (KIT) and the Centro de Investigación e Innovación en Bioingeniería (Ci2B) from the Universitat Politècnica de València (UPV).

Supervisors

Prof. Dr. rer. nat. Olaf Dössel
Karlsruhe Institut für Technologie

Dr. Beatriz Ana Gomis Trenor
Universitat Politècnica de València

Dr.-Ing. Axel Loewe
Karlsruhe Institut für Technologie

External Evaluators

Dr. Alexander V. Panfilov
Universiteit Gent

Dr. Elisa Passini
University of Oxford

Dr. Esther Pueyo Paules
Universidad de Zaragoza

Reading Committee

Prof. Dr. rer. nat. Uli Lemmer
Karlsruhe Institut für Technologie

Prof. Prof. Dr.-Ing. Michael Heizmann
Karlsruhe Institut für Technologie

Prof. Dr.-Ing. Eric Sax
Karlsruhe Institut für Technologie

Dr.-Ing. Axel Loewe
Karlsruhe Institut für Technologie

Abstract

Atrial fibrillation is the most common cardiac arrhythmia. During atrial fibrillation, the atrial substrate undergoes a series of electrical and structural remodeling processes. The electrical remodeling is characterized by the alteration of specific ionic channels, which changes the morphology of the transmembrane voltage known as action potential. Structural remodeling is a complex process involving the interaction of several signalling pathways, cellular interaction, and changes in the extracellular matrix. During structural remodeling, fibroblasts, abundant in the cardiac tissue, start to differentiate into myofibroblasts, which are responsible for maintaining the extracellular matrix structure by depositing collagen. Additionally, myofibroblasts paracrine signalling with surrounding myocytes will also affect ionic channels.

Highly detailed computational models at different scales were used to study the effect of structural remodeling induced at the cellular and tissue levels. At the cellular level, a human fibroblast model was adapted to reproduce the myofibroblast electrophsyiology during atrial fibrillation. Additionally, the calcium handling in myofibroblast electrophysiology was assessed by fitting a calcium ion channel to experimental data. At the tissue level, myofibroblast infiltration was studied to quantify the increase of vulnerability to cardiac arrhythmia. Myofibroblasts alter the dynamics of reentry. A low density of myofibroblasts allows the propagation through the fibrotic area and creates focal activity exit points and wave breaks inside this area. Moreover, fibrosis composition plays a key role in the alteration of the propagation pattern. The alteration of the propagation pattern affects the electrograms computed at the surface of the tissue. Electrogram morphology was altered depending on the arrangement and composition of the fibrotic tissue.

Detailed cardiac tissue models were combined with realistic models of the commercially available mapping catheters to understand the clinically recorded signals. A noise model from clinical signals was generated to reproduce the signal artifacts in the model. Electrograms from highly detailed bidomain models were used to train a machine learning algorithm to characterize the atrial fibrotic substrate. Features that quantify the complexity of the signals were extracted to identify fibrotic density and fibrotic transmurality. Subsequently, fibrosis maps were generated using patient recordings as a proof of concept. A fibrosis map provides information about the fibrotic substrate without using a single cut-off voltage value of 0.5 mV. Furthermore, in this study, using information theory measurements such as transfer entropy combined with directed graphs, the wave propagation direction was tracked. Transfer entropy

with directed graphs provides crucial information during electrophysiology to understand wave propagation dynamics during atrial fibrillation.

In conclusion, this thesis presents a multiscale in silico study of atrial fibrillation mechanisms providing insight into the cellular mediators responsible for the extracellular matrix remodeling and its electrophysiology. Additionally, it provides a realistic setup to create in silico data that can be translated to clinical applications that could support ablation treatment.

Zusammenfassung

Vorhofflimmern ist die häufigste Herzrhythmusstörung. Während des Vorhofflimmerns wird das Vorhofsubstrat einer Reihe von elektrischen und strukturellen Umbauten unterzogen. Die elektrophysiologische Umgestaltung ist durch die Veränderung spezifischer Ionenkanäle gekennzeichnet, die die Morphologie des als Aktionspotential bekannten Transmembranspannungsverlaufs verändert. Die strukturelle Umgestaltung ist ein komplexer Prozess, der die Wechselwirkung mehrerer Signalwege, die zelluläre Wechselwirkung und Veränderungen in der extrazellulären Matrix umfasst. Während des strukturellen Umbaus beginnen Fibroblasten, die im Herzgewebe reichlich vorhanden sind, sich in Myofibroblasten zu differenzieren, die für die Aufrechterhaltung der extrazellulären Matrixstruktur durch Ablagerung von Kollagen verantwortlich sind. Zusätzlich beeinflussen parakrine Signale von Myofibroblasten mit umgebenden Myozyten auch die Ionenkanäle.

Hochdetaillierte Rechenmodelle in verschiedenen Maßstäben wurden verwendet, um die auf Zell- und Gewebeebene induzierte strukturelle Umgestaltung zu untersuchen. Eine Anpassung eines menschlichen Fibroblastenmodells wurde auf zellulärer Ebene vorgenommen, um die Elektrophysiologie von Myofibroblasten während des Vorhofflimmerns zu reproduzieren. Zusätzlich wurde der Einfluss des Calciumhandlings auf die Elektrophysiologie der Myofibroblasten durch Anpassen des Calciumionenkanals an experimentelle Daten untersucht. Auf Gewebeebene wurde die Infiltration von Myofibroblasten untersucht, um die Zunahme der Anfälligkeit für Herzrhythmusstörungen zu quantifizieren. Myofibroblasten verändern die Dynamik hin zu pathologisch kreisenden Erregungen. Eine geringe Dichte von Myofibroblasten ermöglicht die Ausbreitung der Depolarisationswelle durch den fibrotischen Bereich und erzeugt fokale Aktivitätsaustrittspunkte und Wellenbrüche innerhalb dieses Bereichs. Darüber hinaus spielt die Zusammensetzung der Fibrose eine Schlüsselrolle bei der Veränderung des Ausbreitungsmusters der Depolarisationswelle. Die Änderung des Ausbreitungsmusters beeinflusst die an der Oberfläche des Gewebes berechneten Elektrogramme. Die Elektrogrammmorphologie verändert sich in Abhängigkeit von der Anordnung und Zusammensetzung des fibrotischen Gewebes.

Detaillierte Herzgewebemodelle wurden mit realistischen Modellen der kommerziell erhältlichen Untersuchungskatheter kombiniert, um die klinisch aufgezeichneten Signale zu verstehen. Ein Rauschmodell wurde aus klinischen Signalen erstellt, um die Signalartefakte im Modell zu reproduzieren. Elektrogramme aus hochdetaillierten Bidomainmodellen wurden verwendet, um einen Algorithmus für maschinelles Lernen zur Charakterisierung des atrialen fibrotischen Substrats zu trainieren. Merkmale, die die Komplexität der Signale quan-

tifizieren, wurden extrahiert, um die Dichte und Transmuralität der Fibrose zu identifizieren. Anschließend wurden Fibrosekarten unter Verwendung von Patientenaufzeichnungen als Proof of Concept erstellt. Die Fibrosekarte liefert Informationen über das fibrotische Substrat, ohne den häufig klinisch verwendeten Grenzwert von 0,5 mV zu verwenden. Darüber hinaus wurde in dieser Studie unter Verwendung von Messmethoden wie der Transferentropie aus der Informationstheorie in Kombination mit gerichteten Graphen die Wellenausbreitungsrichtung verfolgt. Die Transferentropie liefert in Kombination mit gerichteten Graphen wichtige elektrophysiologische Informationen, um die Dynamik der Wellenausbreitung während des Vorhofflimmerns zu verstehen.

Zusammenfassend stellt diese Arbeit eine In-Silico-Studie von der Zelle zu detaillierten Herzgewebemodellen vor, die Einblicke in die zellulären Mediatoren bietet, die für den Umbau der extrazellulären Matrix und ihrer Elektrophysiologie verantwortlich sind. Darüber hinaus präsentiert die Arbeit eine Simulationsumgebung zum Erstellen von realistischen In-Silico-Daten, die in klinische Anwendungen übersetzt werden können, um Ablationsbehandlungen zu unterstützen.

Resumen

La fibrilación auricular es la arritmia cardíaca más común. Durante la fibrilación auricular, el sustrato auricular sufre una serie de cambios o remodelados a nivel eléctrico y estructural. La remodelación eléctrica se caracteriza por la alteración de una serie de canales iónicos, lo que cambia la morfología del potential de transmembrana conocido como potencial de acción. La remodelación estructural es un proceso complejo que involucra la interacción de varios procesos de señalización, interacción celular y cambios en la matriz extracelular. Durante la remodelación estructural, los fibroblastos que abundan en el tejido cardíaco, comienzan a diferenciarse en miofibroblastos que son los encargados de mantener la estructura de la matriz extracelular depositando colágeno. Además, la señalización paracrina de los miofibroblastos afecta a los canales iónicos de los miocitos circundantes.

Se utilizaron modelos computacionales muy detallados a diferentes escalas para estudiar la remodelación estructural inducida a nivel celular y tisular. Se realizó una adaptación de un modelo de fibroblastos humanos a nivel celular para reproducir la electrofisiología de los miofibroblastos durante la fibrilación auricular. Además, se evaluó la exploración de la interacción del calcio en la electrofisiología de los miofibroblastos ajustando el canal de calcio a los datos experimentales. A nivel tisular, se estudió la infiltración de miofibroblastos para cuantificar el aumento de vulnerabilidad a una arritmia cardíaca. Los miofibroblastos cambian la dinámica de la reentrada. Una baja densidad de miofibroblastos permite la propagación a través del área fibrótica y crea puntos de salida de actividad focal y roturas de ondas dentro de esta área. Además, las composiciones de fibrosis juegan un papel clave en la alteración del patrón de propagación. La alteración del patrón de propagación afecta a los electrogramas recogidos en la superficie del tejido. La morfología del electrograma se alteró dependiendo de la disposición y composición del tejido fibrótico.

Se combinaron modelos detallados de tejido cardíaco con modelos realistas de los catéteres de mapeo disponibles comercialmente para comprender las señales registradas clínicamente. Se generó un modelo de ruido a partir de señales clínicas para reproducir los artefactos de señal en el modelo. Se utilizaron electrogramas de modelos de dos dominios altamente detallados para entrenar un algoritmo de aprendizaje automático para caracterizar el sustrato fibrótico auricular. Las características que cuantifican la complejidad de las señales fueron extraídas para identificar la densidad fibrótica y la transmuralidad fibrótica. Posteriormente, se generaron mapas de fibrosis utilizando el registro del paciente como prueba de concepto. El mapa de fibrosis proporciona información sobre el sustrato fibrótico sin utilizar un valor único de corte de 0,5 milivoltios. Además, utilizando la medición del

flujo de información como la entropía de transferencia combinada con gráficos dirigidos, en este estudio, se siguió la dirección de propagación del frente de onda. La transferencia de entropía con gráficos dirigidos proporciona información crucial durante la electrofisiología para comprender la dinámica de propagación de ondas durante la fibrilación auricular.

En conclusión, esta tesis presenta un estudio in silico multiescala que proporciona información sobre los mediadores celulares responsables de la remodelación de la matriz extracelular y su electrofisiología. Además, proporciona una configuración realista para crear datos in silico que pueden ser usados para aplicaciones clínicas y servir de soporte al tratamiento de ablación.

Resum

La fibril·lació auricular és l'arrítmia cardíaca més freqüent, en la qual el substrat auricular patix una sèrie de remodelacions elèctriques i estructurals. La remodelació de tipus elèctric es caracteritza per l'alteració d'un conjunt de canals iònics que modifica la morfologia del voltatge transmembrana, conegut com a potencial d'acció. La remodelació estructural és un fenomen complex que implica la relació entre diversos processos de senyalització, interaccions cel·lulars i canvis en la matriu extracel·lular. Durant la remodelació estructural, els abundants fibroblasts presents en el teixit cardíac comencen a diferenciar-se en miofibroblasts, els quals s'encarreguen de mantenir l'estructura de la matriu extracel·lular dipositant-hi col·lagen. A més, la senyalització paracrina dels miofibroblasts amb els miòcits circumdants també afectarà els canals iònics.

Es van utilitzar models computacionals molt detallats a diferents escales per estudiar la remodelació estructural induïda a nivell tissular i cel·lular. Es va fer una adaptació a nivell cel·lular d'un model de fibroblasts humans per reproduir-hi l'electrofisiologia dels miofibroblasts durant la fibril·lació auricular. A més, l'exploració de la interacció del calci amb l'electrofisiologia dels miofibroblasts va ser avaluada mitjançant l'adequació del canal de calci a les dades experimentals. A nivell tissular es va estudiar la infiltració de miofibroblasts per tal de quantificar l'augment de vulnerabilitat que això conferia per patir una arrítmia cardíaca. Els miofibroblasts canvien la dinàmica de la reentrada, i presentar-ne una baixa densitat permet la propagació a través de la zona fibròtica, tot creant punts de sortida d'activitat focal i trencaments d'ones dins d'aquesta àrea. A més, les composicions de fibrosi tenen un paper clau en l'alteració del patró de propagació, afectant els electrogrames recollits en la superfície del teixit. La morfologia dels electrogrames es va veure alterada en funció de la disposició i la composició del teixit fibròtic. Per comprendre els senyals clínicament registrats es van combinar models detallats de teixits cardíacs amb models realistes dels catèters de cartografia disponibles comercialment. Es va generar un model de soroll a partir de senyals clínics per reproduir-hi els artefactes de senyal. Es van utilitzar electrogrames de models de bidominis molt detallats per entrenar un algoritme d'aprenentatge automàtic destinat a caracteritzar el substrat fibròtic auricular. Les característiques que quantifiquen la complexitat dels senyals van ser extretes per identificar la densitat i transmuralitat fibròtica. Posteriorment, es van generar mapes de fibrosi mitjançant la gravació del pacient com a prova de concepte. El mapa de fibrosi proporciona informació sobre el substrat fibròtic sense utilitzar un sol valor de tensió de tall de 0,5 mV. A més, utilitzant la mesura del flux d'informació com l'entropia de transferència combinada amb gràfics dirigits, en aquest estudi

es va fer un seguiment de la direcció de propagació de l'ona. L'entropia de transferència amb gràfics dirigits proporciona informació crucial durant l'electrofisiologia per entendre la dinàmica de propagació d'ones durant la fibril·lació auricular.

En conclusió, aquesta tesi presenta un estudi multi-escala in silico que proporciona informació sobre els mediadors cel·lulars responsables de la remodelació de la matriu extracel·lular i la seva electrofisiologia. A més, proporciona una configuració realista per crear dades in silico que es poden traduir a aplicacions clíniques que puguen donar suport al tractament de l'ablació.

Acknowledgments

First, I would like to express my sincere gratitude to Prof. Dr. rer. nat. Olaf Dössel for the opportunity to work under his guidance towards this thesis in the stimulating environment at the Institute of Biomedical Engineering at Karlsruhe Institute of Technology (KIT). I am grateful for his exceptional motivation, confidence, encouragement, and interest in this work, as well as for the great opportunities concerning professional and educational training. To Dr. Axel Loewe for his countless hours of discussion on many different topics, all his support, and for teaching me how wonderful can be the life of a scientist.

I would also like to thank Dr. Beatriz Trenor for her supervision and constant motivation over these years. Additionally, particular gratitude to Prof. Javier Saiz for his valuable discussions and critical feedback during this work. A special thank to Dr. Edward Vigmond for hosting me at the Liryc Institute and many hours of long discussions on openCARP and different topics.

Moreover, I would like to thank all the people during my years in Valencia (Rafa, Chema, Sara, Maite, Jordi, Edison, Alejandro, JuanFran, and Laura). Furthermore, to all my colleagues from the IBT, which form a great team and with whom we all share many laughs and countless hours on setting up simulations. To Laura and Mark, with whom we share many hours of German and Spanish conversations and laughs.

Finally, I want to express my most profound gratitude to my family and especially to my wife, Karla, for always being at my side in this adventure called life, motivating me in the most challenging times, and for all her unconditional support.

Contents

Abbreviations

1D	one dimension
2D	two dimensions
AF	atrial fibrillation
APD	action potential duration
APD_{90}	action potential duration at its 90% of repolarization
ASME	American Association of Mechanical Engineering
BB	Bachmann's bundle
CMf	fibroblast/myofibroblast membrane capacitance
CT	crista terminalis
CV	conduction velocity
d_L	activation gating variable for I_{CaL}
DG	directed graph
dv/dt_{max}	maximum upstroke derivative
EGM	electrogram
f_L	voltage-dependent inactivation gating variable for I_{CaL}
g_{Cab}	maximum conductance of the background Ca^{2+} current
g_{CaL}	maximum conductance of the L-type calcium^{2+} current
g_{K1}	maximum conductance of the K^+ rectifier current
g_{Kv}	maximum conductance of the time-independent K^+ channel
g_{Nab}	maximum conductance of the background Na^+ current
g_{NaK}	maximum conductance of the Na^+/K^+ potassium pump current
I_{CaL}	L-type Ca^{2+} current
I_{K1}	time-independent K^+ current
I_{Na}	sodium current
I_{to}	transient outward K^+ current
K_{NaCa}	maximum conductance of the Na^+/Ca^{2+} current
K_{pCa}	maximum conductance of the Sarcoplasmic Ca^{2+} pump current
LA	left atria
LAA	left atrial appendage
LAT	local activation time
MV	mitral valve
NLEO	non linear energy operator
nSR	normal sinus rhythm

p2p	peak-to-peak amplitude
P_{Na}	maximum conductance of the Na^+ current
peAF	persistent atrial fibrillation
PM	pectinate muscle
PS	phase singularity
PV	pulmonary vein
r_{Kv}	activation gating variable for I_{Kv}
RA	right atria
RAA	right atrial appendage
RBF	radial basis function
RMP	resting membrane potential
RMPf	fibroblast/myofibroblast resting membrane potential
S1	first stimulus
S2	second stimulus
s_{Kv}	inactivation gating variable for I_{Kv}
ShEn	Shannon entropy
SmpEn	sample entropy
SpEn	spectral entropy
TE	transfer entropy
TGF-β1	transforming growth factor-β1
TV	tricuspid valve
VW	vulnerable window

Chapter 1

Introduction

1.1 Motivation

Atrial fibrillation (AF) is the most common arrhythmia and is characterized by irregular electrical activity. The estimated worldwide prevalence of AF in adults is between 2% and 4%, and undiagnosed AF is expected to increase 2.3-fold in the general population. Increasing age is a prominent AF risk factor, but other comorbidities (arterial hypertension, diabetes mellitus, obesity, autoimmune diseases, among others) are potent contributors to AF development and progression [1]. However, AF development and maintenance resulting from the interaction with substrate remodeling known as fibrosis is still under study.

The atrial substrate is a complex structure composed of approximately 75% cardiac myocytes of the tissue volume [2]. The remaining 25% of the volume can contain different types of cells, i.e., non-cardiomyocytes, that can be electrically connected and could affect cardiac electric propagation [3–6].

During persistent atrial fibrillation, the atrial substrate undergoes electrical and structural remodeling. This involves ion channel remodeling [7], fibroblast differentiation [8], changes in the extracellular matrix and inflammatory processes [9]. Inflammatory signaling plays a key role in the electrical and structural remodeling [10], causing alteration of the action potential [11] and differentiation of fibroblasts into myofibroblasts [12, 13]. Myofibroblasts are the cells responsible for maintaining the extracellular matrix and can be electrically connected to the cardiac myocytes [8, 14, 15].

This heterogeneity of the atrial substrate alters the cardiac propagation wavefront, and the dynamics of arrhythmia [16]. Electro-anatomical mapping of the atrial tissue gives a global overview of different patterns of propagation and shows regions that are associated with fibrosis or structural remodeling [17, 18]. Different characteristics of the cardiac tissue can change the dynamics of excitation propagation and alter arrhythmia patterns and affect the morphology of the intracardiac signals. Fractionation of electrograms and a single cut-off voltage value of 0.5 mV are used in clinical practice to define low voltage areas but might be not sufficient to characterize the cardiac substrate [19].

Based on electrogram features at the surface of the tissue, Campos et al. classified different fibrosis types using in silico experiments [20]. However, quantification of fibrotic volume fraction and transmurality in the atrial substrate has not been reported yet. Data-driven approaches can help to overcome the use of a single voltage cut-off value to characterize the cardiac fibrotic substrate based on a more comprehensive, holistic set of criteria.

Additionally, structural modified cardiac substrate alters the propagation. During persistent AF, the electrical activity is chaotic, and the identification of the wavefront propagation is not trivial. Granger causality has been proposed as a measurement that globally characterizes the organization of the wavefront propagation and maps rotational drivers using low spatial resolution sequentially acquired data [21]. However, it requires sequentially recorded segments longer than 2.5 seconds, which are not commonly found in clinical electrophysiology studies. Transfer entropy quantifies the electrogram's information flow and can be used to characterize the wavefront propagation for short recorded segments.

Computational modeling provides a better insight into the mechanistic role of fibrotic tissue characteristics in the initiation and maintenance of arrhythmias [22]. Recently, detailed computational models of the atria have been applied to understand the fibrotic tissue composition and their effect on the electrical propagation [23–25] as well as the electrograms collected over these regions [22, 26, 27]. Relevant characteristics of the electrograms can show how tissue heterogeneities influence their morphology [28] and help on future therapies [17, 29].

1.2 Objectives of the Thesis

The main objective of this thesis is to study the electrical propagation in the atrial substrate in patients with atrial fibrillation using in silico experiments and data-driven techniques. Computer modeling and simulation will allow to reproduce the biophysical phenomena of the electrical propagation at different levels and data-driven techniques help to characterize the fibrotic substrate from electrogram signals and create maps that could be used to guide ablation therapies.

More specifically, this thesis aims to achieve a better understanding of the following research questions:

- Characterization of the fibroblast/myofibroblast electrophysiology and its impact on atrial myocyte action potential.
- Analysis of the role of calcium channels in myofibroblast electrophysiology and its intracellular calcium handling system.
- Quantification of the impact on arrhythmogenicity of myofibroblast infiltration in atrial tissue during atrial fibrillation.
- Investigation of fibrosis composition and the effect on electrogram signals.
- Analysis of the use of electrogram signals to characterize fibrotic substrate.
- Investigation of the use of non-parametric measurements to understand the electrical propagation in cardiac tissue.

1.3 Structure of the Thesis

Part I presents the motivation, the necessary medical and technical fundamentals, and the state of the art to put the research described in this thesis into context.

- Chapter 2 provides an overview of cardiac anatomy and the pathophysiology of AF and fibrosis.
- Chapter 3 reviews the computational models used in this thesis.
- Chapter 4 gives an overview of the clinical electro-anatomical systems used in electrophysiological studies.

Part II describes the in silico experiments to understand myofibroblast electrophysiology that conforms fibrotic tissue.

- Chapter 5 shows the results obtained using the myocyte model adaptation to simulate electrophysiological heterogeneity.
- Chapter 6 contains the simulation results of fibroblasts coupling to human atrial myocytes.
- Chapter 7 contains the in silico experiments of myofibroblast electrophysiology.

Part III describes the tissue level simulations, which analyze fibrosis's influence on the wave front propagation.

- Chapter 8 shows the effect of myocyte-myofibroblast coupling in the atrial tissue during atrial fibrillation.
- Chapter 9 contains the simulation results of the fibrotic tissue composition and the effect on electrograms signals.
- Chapter 10 shows the importance of using a realistic geometry of catheters in the in silico experiments.
- Chapter 11 shows the use of in silico simulations and machine learning to characterize the atrial fibrotic tissue composition.
- Chapter 12 shows the results of using a non-parametric statistic measurement to characterize the electrical propagation in cardiac tissue.

Part IV describes the translation of the created models to clinical applications to identify and characterize fibrotic substrate and wave front propagation.

- Chapter 13 gives an overview of the application of fibrosis maps to guide ablation therapies.
- Chapter 14 gives an overview of the directed graph information flow vector field map to show the electrical propagation in clinical data.

Part V presents the conclusions and possible future works from this thesis.

- Chapter 15 concludes the use of in silico studies and the translation to clinical applications.

- Chapter 16 gives a brief outlook for future studies.

During my research at the KIT and at the UPV, I published one journal paper, eight conference contributions as first author, and an additional journal publication is under review. As a co-author, two journal papers, one conference contribution were published, and an additional journal publication is under review. Moreover, I supervised four student final degree theses that partly form the basis of the work presented here. Both publications and student theses are referenced in the corresponding sections of this thesis.

PART I

FUNDAMENTALS

Chapter 2

Medical fundamentals

2.1 Atrial anatomy and physiology

In this chapter, the fundamentals of cardiac anatomy, physiology, modeling, and electro-anatomical mapping are described. These concepts are essential to understand the studies presented in the subsequent parts and to put them into context. After a brief description of atrial anatomy and physiology, cardiac electrophysiology is summarized. Then, the state of the art in clinical mapping systems is presented. For a more in-depth introduction to the different topics, interested readers are referred to the cited bibliography.

2.2 Atrial fibrillation

Atrial fibrillation (AF) is a global health care issue, with an increasing prevalence and incidence worldwide. Several theories have been proposed for the AF increase, including the rising prevalence of AF risk factors such as obesity, diabetes, auto-immune diseases, and aging of the population (Figure 2.1).

During AF the atrial substrate undergoes an electrical and structural remodeling which increases the tissue's vulnerability to fibrillation initiation and maintenance. As a consequence of AF, an increased risk of stroke and transient ischemic attack have been reported. Furthermore, AF-related strokes could lead to long-term disability or death.

2.3 Anatomy of the human heart

The heart is a four chamber hollow organ whose main function is to pump blood into the circulatory system. The human heart lies within the thorax, posterior to the sternum and costal cartilages, and rests on the diaphragm's superior surface. The heart occupies a space between the two lungs in an oblique position, with two-thirds to the left of the thorax's midline.

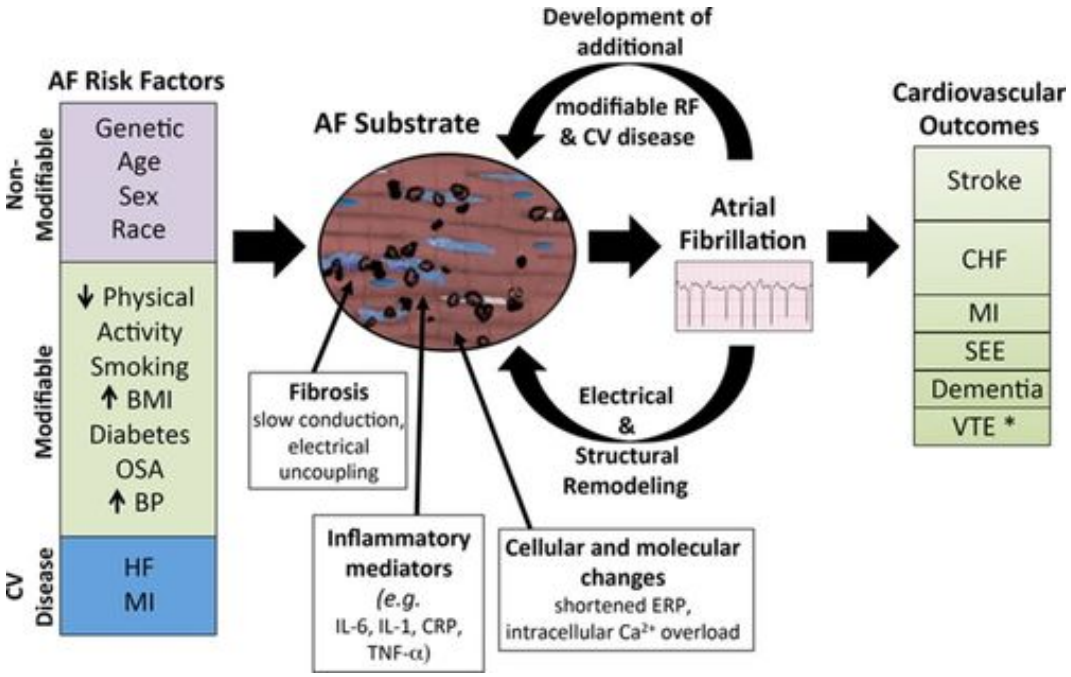

Figure 2.1: Atrial fibrillation risk factors can originate or modify the cardiac substrate. Atrial fibrosis, inflammatory mediators, cellular, and molecular changes can modify the substrate arising an electrical and structural remodeling and the development of additional risk factors and cardiovascular diseases. Atrial fibrillation is not a deadly arrhythmia but increases the risk of stroke, heart failure, myocardial infarction, dementia, and others. Adapted from [30]

The pericardium is a serous membrane that surrounds the heart. In the inferior region, the pericardium is attached to the diaphragm. In the anterior region, the superior and inferior pericardiosternal ligaments fix the pericardium to the sternum. The pericardial space contains a lubricating substance called pericardial fluid.

The two upper chambers, i.e. the atria, work as collecting chambers; the two lower chambers, i.e. the ventricles, pump blood out of the heart. The septum separates the heart into the left and right sides. The right side collects the blood coming from the circulatory system and pumps the blood for oxygenation. The oxygenated blood comes from the lungs to the heart's left side, which pumps the blood back to the circulatory system (Figure 2.2).

The right atrium has three anatomically distinct regions: the posterior wall, the anterior wall, and the interatrial septum. The posterior portion has a smooth wall and holds most of the structures of the right atrium. It receives blood through both the superior and inferior vena cavae and the coronary sinus. It also contains the fossa ovalis, the sinus node, and the atrioventricular node. The wall of the anterior portion of the right atrium is lined with horizontal, parallel ridges of muscle bundles called pectinate muscles.

The right ventricle wall has abundant, coarse trabeculae carnae. The right ventricle is communicated with the right atrium through the tricuspid valve. The right ventricle communicates with the lungs through the pulmonary trunk.

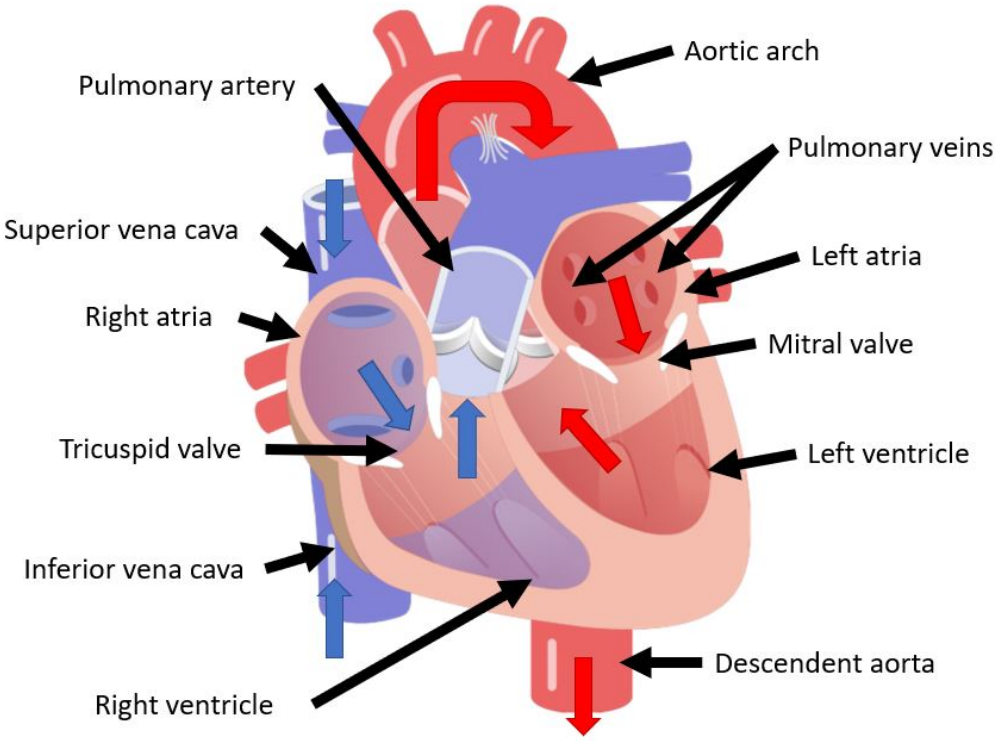

Figure 2.2: Anatomy and blood flow of the human heart. Blue arrows indicate the blood flow direction from the circulatory system with deoxygenated blood to the right atrium through the superior and inferior vena cava. Deoxygenated blood then passes to the right ventricle, which pumps the blood to the lungs through the pulmonary artery. Red arrows indicate the blood flow of oxygenated blood from the lungs to the left atrium through the pulmonary veins. Oxygenated blood passes to the left ventricle, and then it is pumped back to the circulatory system through the aorta.

The left atrium receives the oxygenated blood from the lungs through the left and right pulmonary veins. The pulmonary veins typically enter the heart as two pairs of veins inserting posteriorly and laterally into the left atrium (individuals with 3 or 5 pulmonary veins have also been identified). The posterior and anterior walls of the left atrium are smooth. The left atrial appendage is characterized by pectinate structures similar to the ones found in the right atrium.

The left ventricle communicates with the left atrium through the mitral valve. The left ventricle, as the right ventricle, has abundant trabeculae carneae. In contrast to the right ventricle, the muscular ridges tend to be relatively thin. However, the myocardium in the left ventricle wall is much thicker than the right one due to the amount of force that needs to be developed to pump the blood into the circulatory system.

2.4 Histology of the heart

The atrial substrate is a complex structure composed of approximately 75% cardiac myocytes of the tissue volume [2] and the remaining 25%, i.e., non-cardiomyocytes [3–6].

Myocytes in the myocardium are organized in bundles, separated by perimysial fibrous tissue. Within these bundles, strands of myocytes can be separated from each other by endomysial fibrous tissue. Structural remodeling due to heart disease is often associated with fibrosis and increased transverse fiber separation. In the atria, fibrosis between myofibers increases in volume with aging.

Single myocytes are nucleated specialized muscle cells with an almost cylindrical shape of 100 μm length and 10-25 μm diameter. However, in reality, myocytes have an irregular ellipsoidal shape and align along their principal axis.

Histological cuts from atrial tissues from animals with persistent AF using Masson's trichrome stain demonstrated a significant increase in diffuse collagenous stroma in the atria compared to controls (11.01±2.87% and 3.08±0.77%; $P < 0.01$) [31]. Cardiac healthy tissue presents a lower amount of collagenous fibers. Cardiac cells are electrically connected through channels known as gap junctions allowing action potentials to spread through the cardiac tissue.

Fibroblasts play a critical role in wound healing in various organs such as skin, lungs, liver, heart, among others. Fibroblasts' contribution to wound healing includes migration, differentiation, and recruitment of inflammatory cells. Differentiated fibroblasts in the heart are known as myofibroblasts and are responsible for secreting the extracellular matrix in response to injury signals. They secrete large amounts of matrix proteins, including collagen type I, collagen type III, collagen type IV, periostin, and fibronectin (Figure 2.3).

Morphologically, myofibroblasts are spindle shaped cells with large endoplasmic reticulum organelles. The characteristics of myofibroblasts are the expression of alpha-smooth muscle actin (αSMA) and the intermediate filament desmin. While these characteristics are well known, the electrophysiology and the molecular mechanisms in myofibroblast transdifferentiation in vivo are not well understood.

In patients with AF, various degrees and forms of atrial fibrosis can be found, which results in conduction disturbances. Atrial fibrosis may be sufficient to increase AF vulnerability, as shown in mice with selective atrial fibrosis due to overexpression of TGF-β1, a cytokine that is expressed during the inflammatory process [13]. The inflammatory process triggers the differentiation of fibroblasts into myofibroblasts. Myofibroblasts start depositing the extracellular matrix that underlie the structural remodeling and are obstacles for electrical propagation. Additionally, myofibroblasts can be electrically connected and introduce depolarization and repolarization heterogeneities within the cardiac tissue.

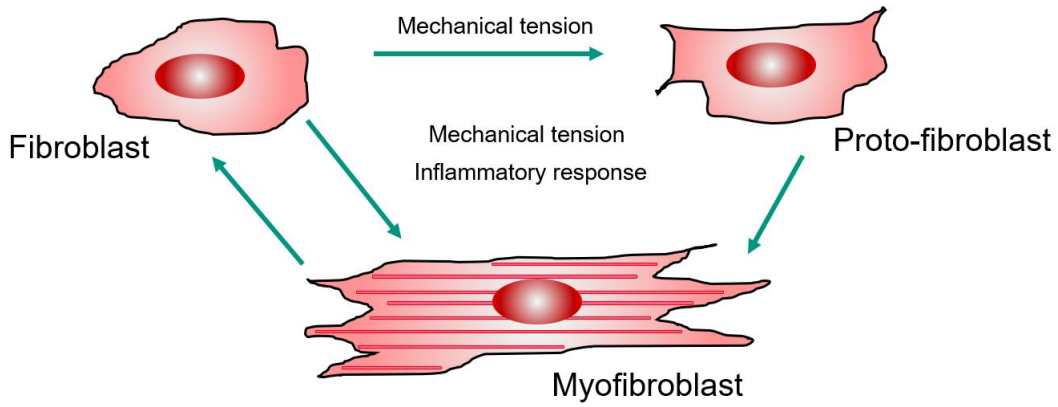

Figure 2.3: Fibroblasts (top left corner) are cells that can differentiate by different triggering stimuli. On the one hand, mechanical tension can differentiate fibroblasts into proto-fibroblasts (top right corner), which can also differentiate into myofibroblasts. On the other hand, mechanical tension or inflammatory cytokines can directly differentiate fibroblasts into myofibroblasts. Moreover, after the stimulus is over, some myofibroblasts can differentiate back into fibroblasts.

2.5 Eletrophysiology of the heart

At the microscopical level and under physiological conditions, the distribution of ions in the extracellular and intracellular medium across the cell membrane yields a resting membrane potential of approximately -80 mV in cardiac cells. Ions can move across the membrane through specific ion channels that can open and close in response to changes in membrane potential or ligands binding to receptors associated with the channel. The orchestrated interaction of the ion channels leads to a characteristic transmembrane potential waveform known as the action potential. The action potential can be divided into four phases concerning the flux of ions across the membrane (Figure 2.4 (blue trace)). Phase 4 corresponds to the resting potential. Phase 0 is the phase of rapid depolarization. The membrane potential shifts into a positive voltage range, mainly characterized by an influx of sodium ions. Phase 1 is the phase of rapid repolarization characterized by an efflux of potassium ions. Phase 2, the plateau phase, is the longest phase. It is unique among excitable cells and marks the phase of calcium entry into the cell and potassium efflux. Phase 3 is the phase of rapid repolarization that restores the membrane potential to its resting value. Gap junctions allow action potentials to spread through the cardiac tissue in a coordinated manner.

During AF, cardiomyocytes undergo an electrical remodeling of ion channels, which will shorten the action potential (Figure 2.4 (red trace)). Experimental studies have revealed a decrease in I_{CaL}, I_{to}, I_{sus}, and I_{Kur} currents as factors underlying action potential shortening. It has also been observed an increase in I_{K1}. Additionally, several studies have reported alterations in the proteins that form the gap junctions connexin 40 (Cx40) and/or connexin 43 (Cx43) in patients with AF. Other studies have reported lateralization of connexins, with an increased heterogeneity in Cx40 distribution and a reduction of Cx43 [32].

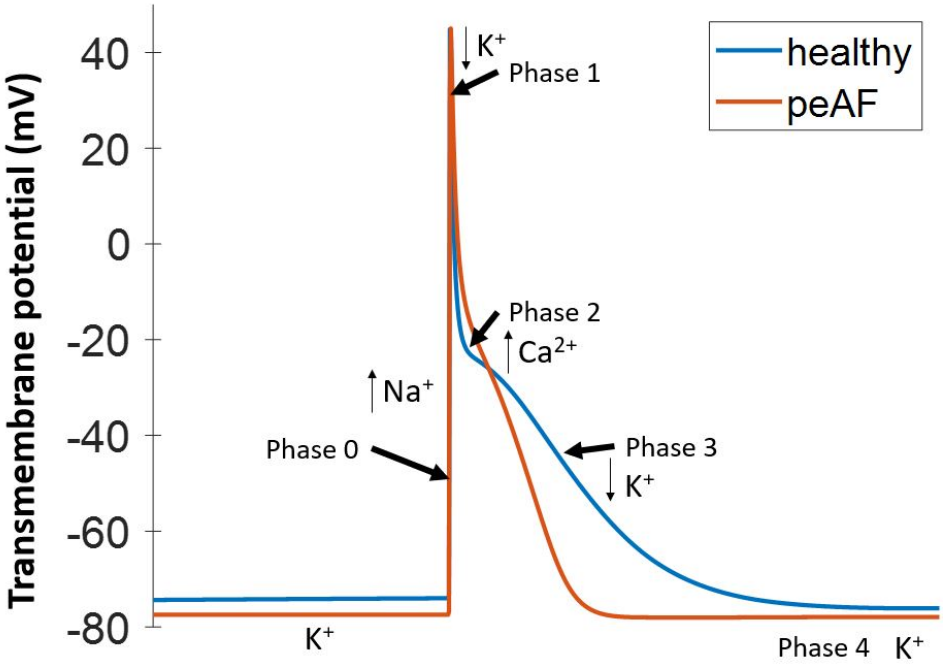

Figure 2.4: Physiologaical human atrial action potential (blue trace) and persistent atrial fibrillation action potential (red trace). The four characteristic phases of the action potential are shown with the main ion flux. Cardiac myocytes are in a resting state (Phase 4) mainly maintained by K^+. When the cell is stimulated, it depolarizes (Phase 0) characterized by an influx of Na^+. It is followed by rapid repolarization (Phase 1) and a plateau phase (Phase 3). The cell then recovers its resting state (Phase 4).

At the macroscopical level (Figure 2.5), the electrical activation of the heart starts at the sinus node. Sinus node cells are self-excitatory pacemaker cells. The activation propagates throughout the right atrium and to the left atrium through Bachmann's bundle from the sinus node. The atrioventricular node (AV node), located at the atria and ventricles boundary, provides the only conducting path from the atria to the ventricles. A specialized conduction system provides propagation from the AV node to the ventricles. This system is composed of a common bundle, called the bundle of His, which separates into two bundle branches propagating along each side of the septum, constituting the right and left bundle branches. The ventricular myocardium activation is performed from the apex to the base and from the endocardial side to the epicardial side.

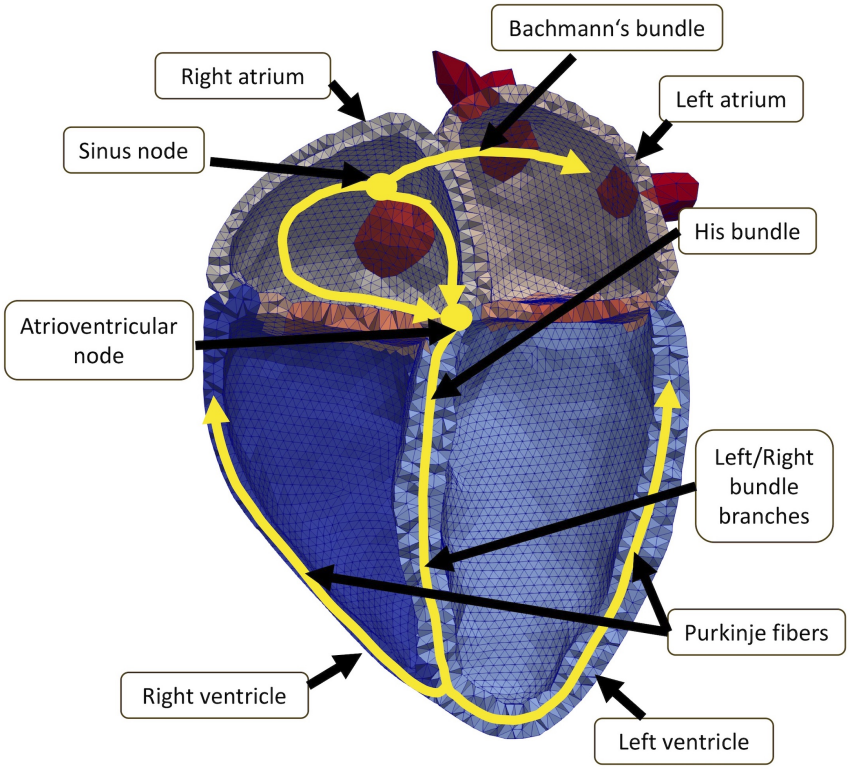

Figure 2.5: The heart's electrical activation starts at the sinus node, which is located in the right atrium. The depolarization wave travels across the right atrium to the atrioventricular node and the left atrium across the Bachmann's bundle. The depolarization wave passes to the ventricle from the atrioventricular node to the bundle of His. Its distal section splits into the left and right bundle branches and into the Purkinje fibers, which activate the ventricular myocardium.

Fibrosis, considered as structural remodeling of the cardiac substrate, can notably alter the electrical propagation (Figure 2.6). Fibrotic tissue has been shown to attract and anchor rotational activity. However, it is still unclear how fibrosis alters atrial fibrillation dynamics and increases the vulnerability to atrial fibrillation.

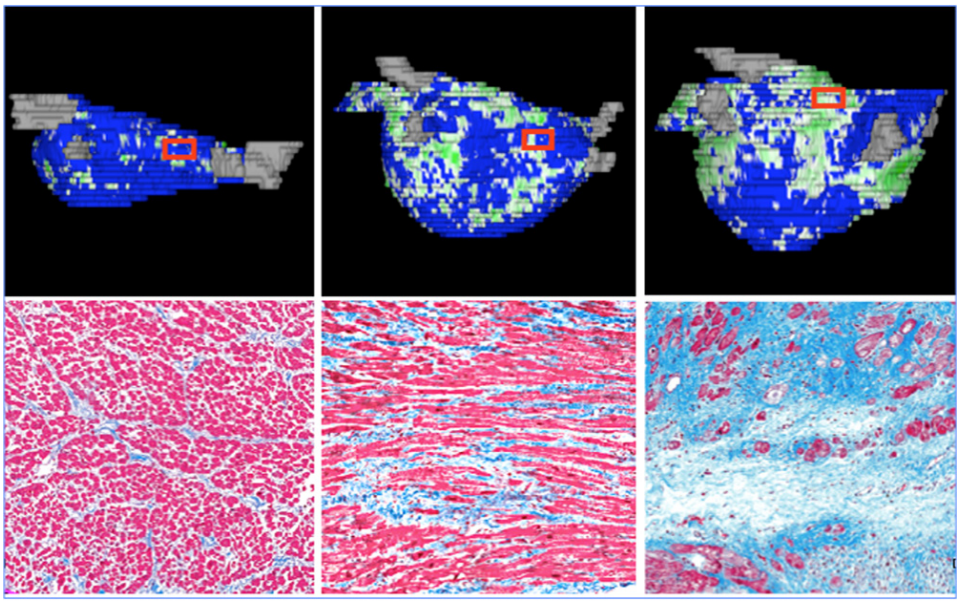

Figure 2.6: Late-gadolinium enhanced magnetic resonance and histological cuts from hearts that suffered from atrial fibrillation. a) Low density of fibrosis, where magenta color indicates cardiac myocytes in the tissue. b) Mid-fibrosis density where the amount of collagen (blue) was increased in the histological cut. c) High fibrosis density, histological cut reveals a considerable amount of collagen present in the tissue and a few cardiac myocytes. Adapted from [33].

Chapter 3

Computational modeling of cardiac electrophysiology

In this chapter, the basic concepts of computational models of cardiac electrophysiology are introduced. The mathematical formulations cover different scales from single cell ion channel to the tissue level of the electrical propagation and forward calculation of the intracardiac signals.

3.1 Cardiac cell modeling

In 1952 Alan Hodgkin and Andrew Huxley were the first scientists to describe the ionic mechanisms underlying the action potential initiation in the squid giant axon [34]. The neuron cell was modeled using an analogy to an electric circuit where the cell membrane is represented as a capacitor. Ion channels are represented as variable conductances. Specific ions can flow through ion channels driven by the electrochemical gradient, represented by voltage sources, and current sources representing ion pumps. The transmembrane voltage is determined by the sum of all currents across the membrane as described in Eq 3.1.

$$I_m = C_m \frac{dV_m}{dt} + \Sigma_\chi I_\chi \tag{3.1}$$

where I_m is the total current across the cell membrane, C_m is the cellular membrane capacitance, $\frac{dV_m}{dt}$ is the derivative of the transmembrane voltage with respect to the time, and I_χ is the ion current flow for a specific ion species (Na^+,K^+, Ca^{2+}).

In the Hodgkin-Huxley formulation, channel conductance is assumed to be controlled by gates that take on values between zero and one, representing the cells' portion in one state. Since cells have thousands of ion channels, the current flow produced by ion species passing through a channel is described by Eq. 3.2

$$I_\chi = \overline{g}_\chi \prod_n \eta_n (V_m - E_\chi)$$

where $\overline{g}_\chi$ is the maximum conductance of the channel and η_n is a product of all gating variables. The gating variable is assumed to follow first order dynamics (Eq. 3.2).

$$\frac{d\eta}{dt} = \alpha(V_m)(1-\eta) - \beta(V_m)\eta = \frac{\eta_\infty(V_m) - \eta}{\tau_\eta(V_m)}$$

where α and β are rates which can be cast into an equivalent form of a steady state value (η_∞) and a rate of change (τ_η).

3.2 Tissue and organ modeling

As previously mentioned in chapter 2, cardiac cells are electrically connected via gap junctions. The mathematical model that describes the electrical propagation's biophysical phenomena in cardiac tissue is known as the bidomain model. The bidomain model represents cardiac tissue as a homogeneous medium of the intracellular and the extracellular domains. The two computational domains coexist in the bidomain model and occupy the same geometrical space.

$$\nabla \cdot (\sigma_i \nabla \phi_i)) = \beta I_m \tag{3.2}$$

$$\nabla \cdot (\sigma_e \nabla \phi_e)) = -\beta I_m - I_{e,s} \tag{3.3}$$

$$I_m = C_m \frac{\partial V_m}{\partial t} + I_{ion}(V_m, v) - I_{trans} \tag{3.4}$$

$$V_m = \phi_i - \phi_e \tag{3.5}$$

ϕ represents the electrical potential, the indices i and e refer to the intracellular and extracellular spaces, respectively. σ is the conductivity tensor, β is the surface to volume ratio of the myocytes, and I_{ion} the total transmembrane ionic current density from the cellular model. The latter is dependent on V_m and a vector v of further state variables. I_{trans}, a transmembrane current density stimulus, and $I_{e,s}$, an extracellular current density, describe external stimuli. If a bath surrounds a tissue, the bath is treated as an extension of the extracellular space.
Adding (3.2) and (3.3) and incorporating it into (3.5) yields:

$$\nabla \cdot (\sigma_i + \sigma_e)\nabla \phi_e = -\nabla \cdot (\sigma_i \nabla V_m) - I_{e,s} \tag{3.6}$$

$$\nabla \cdot (\sigma_i \nabla V_m) = -\nabla \cdot (\sigma_i \nabla \phi_e) + \beta I_m \tag{3.7}$$

The monodomain model assumes that the intra- and extracellular domains have equal anisotropy ratios. Although it is a simplification of the bidomain model, it is still valid to study the electrical propagation in the cardiac tissue.

In case of equal anisotropy ratios, the tensors can be related by a scalar, λ, such as in Eq 3.8.

$$\sigma_e = \lambda \sigma_i \tag{3.8}$$

we can recast the bidomain equation in a simpler form. Plugging Eq. 3.8 into 3.2 and using 3.5 yields

$$\nabla \cdot \sigma_i \nabla \phi_i = \beta I_m - I_i \tag{3.9}$$

$$\nabla \cdot \sigma_i \nabla \phi_e = \nabla \cdot \sigma_i \nabla \phi_i - \nabla \cdot \sigma_i \nabla V_m = -\frac{1}{\lambda}(\beta I_m + I_e). \tag{3.10}$$

Subtracting 3.10 from 3.9 and multiplying with $\lambda/(1+\lambda)$ results in

$$\frac{\lambda}{1+\lambda}\nabla \cdot \sigma_i \nabla V_m = \beta I_m + \frac{1}{1+\lambda} I_e - \frac{\lambda}{1+\lambda} I_i. \tag{3.11}$$

Now, subtract 3.9 from 3.11 to obtain

$$\frac{\lambda}{1+\lambda}\nabla \cdot \sigma_i \nabla V_m = \beta I_m + \underbrace{\frac{1}{1+\lambda} I_e - \frac{\lambda}{1+\lambda} I_i}_{-\beta I_{tr}}. \tag{3.12}$$

$$(1+\lambda)\nabla \cdot \sigma_i \nabla \phi_e = -\nabla \cdot \sigma_i \nabla V_m - I_e - I_i \tag{3.13}$$

As indicated in Eq. 3.12, the combined effect of the intracellular and extracellular injected stimulus currents can be interpreted as a depolarizing transmembrane stimulus if we define

$$I_{tr} = -\frac{1}{\beta}\left(\frac{1}{1+\lambda} I_e - \frac{\lambda}{1+\lambda} I_i\right). \tag{3.14}$$

The choice $I_e = -I_i$ at any given site is equivalent to a transmembrane current stimulus of strength I_i/β, that is,

$$\beta I_{tr} = -\left(\frac{1}{1+\lambda} I_e - \frac{\lambda}{1+\lambda} I_i\right) = -\left(-\frac{1}{1+\lambda} I_i - \frac{\lambda}{1+\lambda} I_i\right) = -\left(-\frac{1+\lambda}{1+\lambda} I_i\right) = I_i. \tag{3.15}$$

This is consistent with the assumption that the injection of a positive current I_i into the intracellular space increases ϕ_i which exerts a depolarizing effect upon $V_m = \phi_i - \phi_e$.

In this case the current terms in Eq. 3.13 cancel out. As expected, any current injected in one domain is withdrawn at the same spot in the other domain. Therefore no current flow occurs as a consequence of I_e or I_i and no extracellular potential field is set up. All changes in ϕ_e are caused indirectly then via changes in V_m.

Eqs. 3.12-3.13 reveal that, unlike in the bidomain model where $\sigma_e \neq \lambda \sigma_i$ holds, the temporal evolution of the transmembrane voltage in Eq. 3.12 is fully independent of ϕ_e. Hence, if only the evolution of V_m is of interest, only Eq. 3.12 needs to be solved, but not the

elliptic PDE given by 3.13 which is a more expensive task. For more detailed considerations we refer the reader to the report by Nielsen et al [35].

The monodomain model is an approximation which can be used whenever the effect of extracellular fields upon tissue polarization can be ignored. As mentioned above, since the temporal evolution of the V_m in Eq. 3.12 is fully independent of ϕ_e, any changes in the extracellular potential fields cannot exert any influence upon V_m.

Therefore, under the assumption of equal anisotropy ratios one needs to solve only the parabolic PDE above with the intracellular conductivity set to twice the harmonic mean, $\sigma_i\sigma_e(\sigma_i+\sigma_e)^{-1}$. This yields

$$\nabla\cdot(\sigma_m\nabla V_m) = \beta I_m + \beta I_t r \tag{3.16}$$

where the bidomain equivalent monodomain conductivity σ_m is given as

$$\sigma_m = \sigma_i\sigma_e(\sigma_i+\sigma_e)^{-1}. \tag{3.17}$$

Simulations were run using two different software packages. One of the software was developed during this thesis in the UPV, in which the source code was based on the acceleration of the cardiac monodomain simulations using GPUs [36]. As part of the research project at KIT, simulations were then migrated and extended to bidomain simulations and ran under the developed software openCARP (`www.opencarp.org`) [37, 38].

Chapter 4

Electro-anatomical mapping

In this chapter, an introduction to clinical electro-anatomical mapping systems is presented. An overview of mapping catheters, intracardiac signals, and maps generated to guide ablation therapies is given.

4.1 Intracardiac signals

Single electrodes capture the extracellular potential in respect to a far away reference ground electrode. These recorded signals are known as unipolar electrograms. Unipolar electrograms are strongly affected by different artifacts from the patient and the recording system, and by the clinical environment.

The difference between two signals from neighboring electrodes constitutes a bipolar electrogram, which is the most common waveform used during a typical clinical electrophysiology study.

The main advantage of bipolar recordings is far-field rejection. Far-field artifacts present in a unipolar signal are removed from the bipolar signal because each electrode of the bipolar pair perceives a similar far-field voltage signal. Consequently, using a high-pass filter with a higher cut-off frequency, such as 30 Hz, for bipolar signals helps minimize baseline drifts/shifts, with no further loss of information. One of the drawbacks of using bipolar electrograms is that they are affected by the orientation of the electric propagation wavefront.

In the last years, omnipolar electrograms have emerged with the advantage of overcoming the directional dependence of the bipolar electrogram. The omnipolar electrogram calculation looks at all possible bipolar electrode orientations and obtains the electrode orientation–independent electrograms along the maximal bipolar direction.

4.2 Mapping catheters

Available mapping catheters have different shapes and electrode characteristics depending on the manufacturer (Figure 4.1). In silico experiments have shown that different electrode

sizes can influence the recorded voltage [39]. Smaller electrodes typically result in sharper and shorter EGM duration. Therefore, the amplitude of a bipolar electrogram depends on the electrode size, the angle of incidence between the catheter and tissue [40], and the orientation of the bipole relative to the wavefront propagation. The design of most multi-electrode catheters with small electrodes allows reducing the influence of the angle of incidence. Computer and animal models suggest an optimal spatial resolution with electrodes sizes of 1 mm.

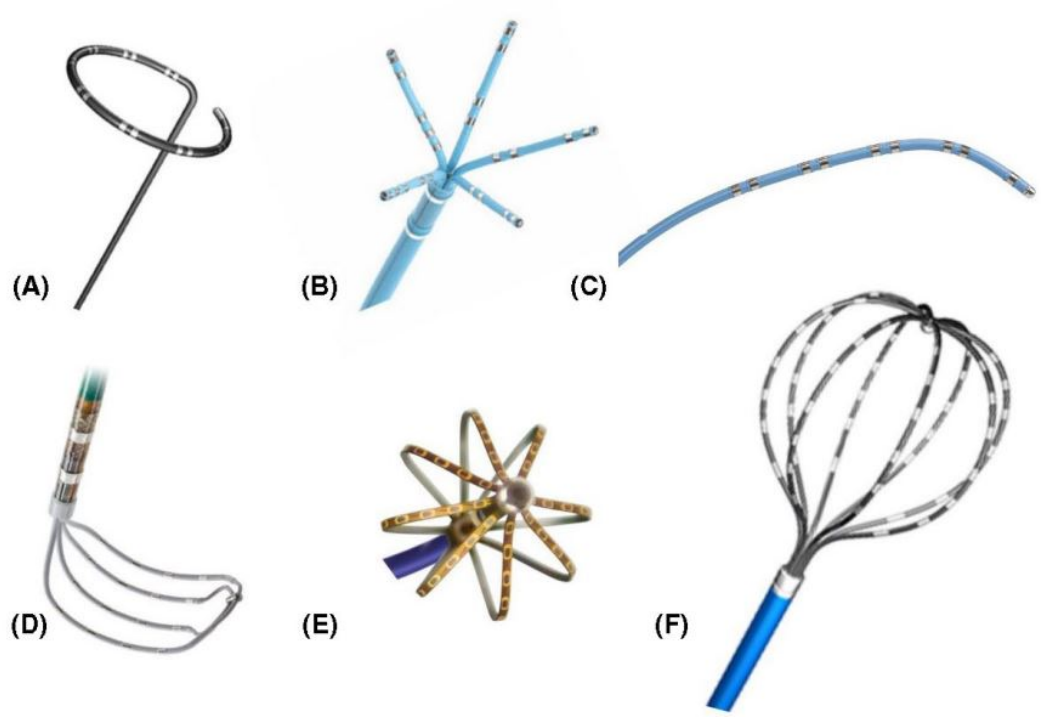

Figure 4.1: Commercially available mapping catheters. A) Circular loop catheter; B, Five-splined catheter (PentaRay, Biosense Webster); C, Linear catheter (Decapolar, Biosense Webster); D, Grid catheter (HD Grid, Abbott); E, Mini-basket catheter (Orion, Boston Scientific); F, Basket catheter (Constellation, Boston Scientific). Adapted from [41].

Commercially, there are several mapping catheters that are commonly used in the daily clinical practice for an electrophysiological study. Table 4.1 summarizes the characteristics of the electrode, such as size, interelectrode space, and diameter of the catheters used in this thesis.

Table 4.1: Commercially available cardiac mappping catheters

Model	Manufacturer	Number of electrodes	Electrode size (mm)	Spacing (Edge to Edge)	Spacing recorded (Center to Center)
Lasso	Biosense Webster	20	1	2-6-2	3
HD Grid	Abbott	16 or 32	1	3	4
IntellaMap Orion	Boston Scientific	64	0.9x0.45	1.6	2.5

4.3 Clinical maps

The electro-anatomical mapping system is a fundamental tool for guiding ablation procedures. The term electro-anatomical mapping is related to the assignment and displays encoded information (i.e., voltage, activation time) according to its spatial coordinates.

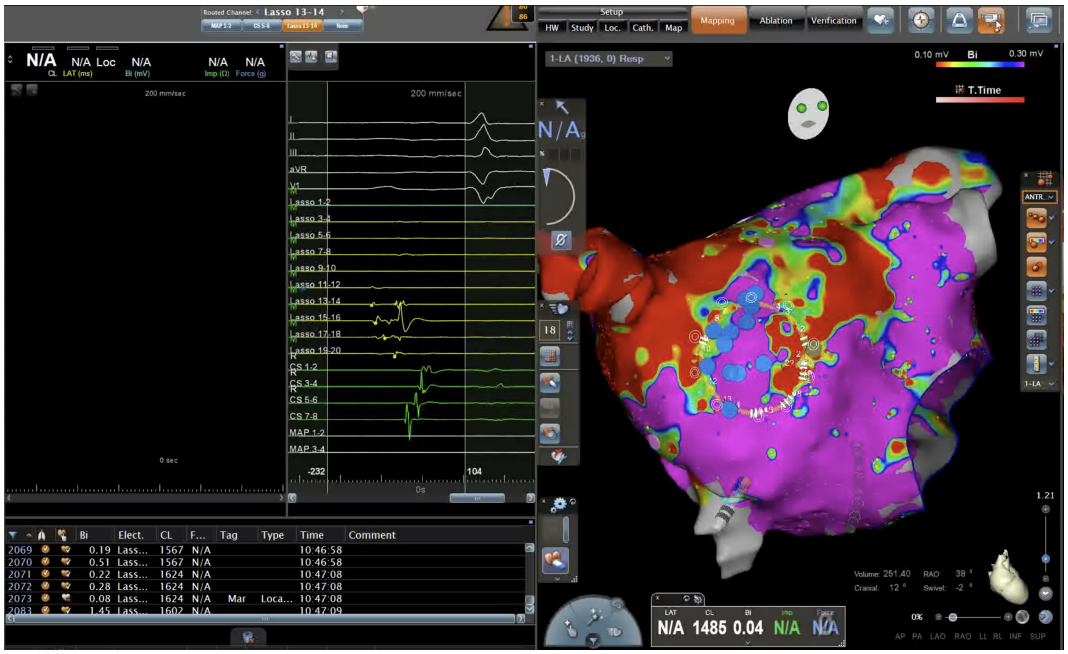

Figure 4.2: Patients calculated voltage map during an electrophysiology study. The voltage map at the right indicates the high or low voltage amplitude derived from the electrograms showed at the left. In this specific case, purple color indicates values above a defined voltage cut-off value of 0.3 mV.

The distribution of voltage on the cardiac surface is used to identify pathological tissue or fibrotic areas with a cut-off value. In the ventricle, Marschlinski et al. [42] using an ablation catheter with a large tip, determined a low voltage cut-off value ranging from 0.5 mV to 1.5 mV in ischemic regions. Other studies have validated the threshold of 1.5 mV in

animal models of transmural myocardial infarction. However, for fibrosis, only post-infarct scars have been validated. Whole-heart histology in non-ischaemic cardiomyopathy has highlighted that no specific voltage cut-offs can be found, as fibrosis patterns and architecture are different from ischaemic cardiomyopathy.

In clinical practice, bipolar peak-to-peak voltage is of great importance, and a single cut-off value of 0.5 mV is commonly used to identify fibrotic areas in the atria [43]. Nevertheless, this cut-off value has not yet been standardized and differentiated from patient to patient due to the fibrosis microarchitecture [44].

PART II

CELLULAR LEVEL

Chapter 5

Human atrial myocyte electrophysiology

The Koivumäki et al. [45] mathematical model of human atrial cells is suitable for investigating heterogeneous myocyte-to-myocyte electrical coupling, atrial fibrillation electrical remodeling, and the heterocellular electrical coupling between myocyte-to-non-cardiomyocyte cells such as fibroblast/myofibroblast. The myocyte model conductances were fitted to obtain different action potentials to simulate the electrophysiology from different human atrial regions, as will be detailed in this section.

5.1 Methods

From Eq. 3.2 the maximum conductances g_χ were fitted to reproduce physiological action potentials of the human atria. The conductance of five ionic currents: transient outward K^+ current (I_{to}), potassium rapid current (I_{Kr}), potassium slow current (I_{Ks}), time-independent K+ current (I_{K1}), and L-type Ca^{2+} current (I_{CaL}) were fitted using the least-squares fitting method to reproduce experimental data of the action potential, as proposed in previous simulation studies [46, 47].

As many experimental data have the action potential duration at its 90 percent (APD_{90}) and the resting membrane potential (RMP), the cost function was defined as in Eq. 5.1.

$$J(\theta) = \sqrt{\frac{\sum_{i=1}^{n}(APD_{90\,predi} - APD_{90})^2}{n}} + \sqrt{\frac{\sum_{i=1}^{n}(RMP_{predi} - RMP)^2}{n}} \tag{5.1}$$

The fitted models were then simulated for 10000 seconds to ensure long term stability.

Furthermore, the cardiomyocyte model ionic channels were changed to reflect the electrical remodeling during persistent AF in all atrial regions by modifying ion channel conductances for I_{CaL}, I_{to}, I_{K1}, sustained outward K^+ current (I_{sus}), Na^+/Ca^{2+} exchanger (NCX), sarcoplasmic reticulum Ca^{2+} ATPase (SERCA) pump, and ryanodine receptors (RyR), and specific calcium handling parameters, such as phospholamban (PLB), sarcolipin (SLN), and

the baseline phosphorylation (phos). Dilation was also modeled by increasing the length of the cell by a factor of 1.1 as proposed by Koivumäki et al. [48].

At the cellular level in silico experiments offer a wide range of possibilities to investigate in detail the electrophysiology of single cells.

Following the law of the conservation of charge, the total net flux of ions across a specific channel can be quantified using the area under the ionic current curve along time. The total net flux can be used to identify differences in ion channels during pathological events such as AF or because cellular coupling was altered.

The action potential is a characteristic trace of the transmembrane voltage along time. In the action potential, we can measure several biomarkers such as APD_{90}, the amplitude (APA), RMP, and the change rate of the membrane potential at repolarization (dV/dt_{max})

Additionally, the action potential duration (APD) is closely related to the frequency of stimulation. The faster the cell is paced, the less time has the cell to recover its initial state. This has been identified as a potential mechanism for arrhythmia. To better understand the changes of APD in relation to the stimulation frequency, the concept of restitution curves has been established. The steepness of the APD restitution curve and local tissue refractoriness are both thought to play important roles in arrhythmogenesis.

The restitution curve's dependence on its preceding pacing history was investigated by the standard extra-stimulus (S1–S2) restitution protocol (Figure 5.1). Single myocytes were stimulated with 5 pulses (S1) at an initial cycle length of 1000 ms followed by an extra-stimulus (S2) where the coupling interval is progressively shortened. Restitution curve's slope is an indicator of arrhymogencity [49]. Maximum slope values less than 1 have been shown to be less arrhythmogenic than slope values higher than 1.

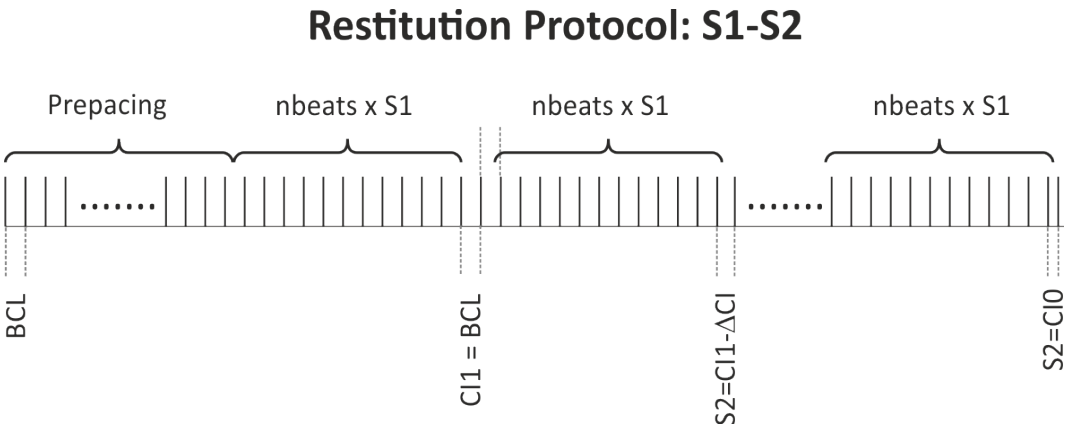

Figure 5.1: Single cell restitution stimulation protocol. The protocol starts with an initial pre-pacing period where a number of defined stimuli are delivered at the chosen basic cycle length (BCL) to stabilize the action potential. After stabilization, BCL is kept constant, but prematurity of the coupling interval (CI) of the S2 decreases until the final S2 CI. Adapted from [50]

.

5.2 Results

Atrial electrophysiology heterogeneity was produced for single cell action potential simulations with a BCL of 1000 ms. Fitted relative values for each atrial region with respect to their maximum conductance are shown in Table 5.1. APD_{90} values in Table 5.1 matched the reported experimental values for different regions of the atria [7, 51–54].

Figure 5.2a depicts action potentials under normal sinus rhythm and Figure 5.2b action potentials under peAF conditions in the different atrial regions. This study highlights the differences in APD_{90} for four characteristic atrial regions, which are common areas where reentrant activity can be maintained or where ectopic beats are originated. Under physiological conditions, APD_{90} was 236.4 ms for RA, 214 ms for LA, 176.1 ms for PV, and 292.8 ms for CT. However, under peAF conditions APD_{90} was 165.5 ms, 139.8 ms, 120.8 ms, and 180.2 ms for the RA, LA, PV, and CT, respectively.

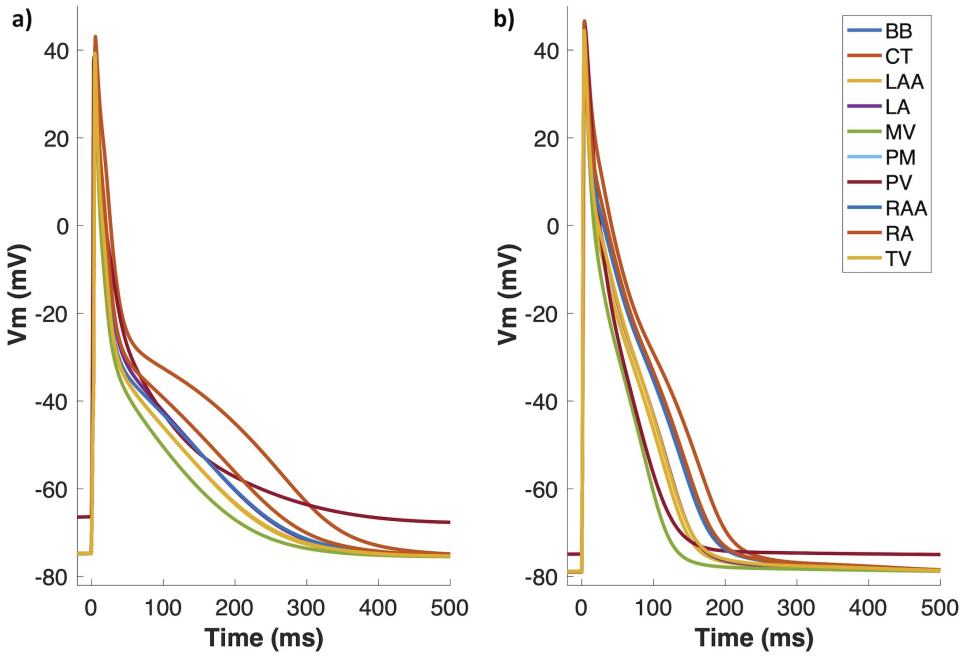

Figure 5.2: a) Human atrial action potential heterogeneity under physiological conditions. b) Human atrial action potential heterogeneity under the electrical remodeling due to persistent atrial fibrillation.

APD_{90} decreased by 40% for RA, LA, and CT and by approximately 30% for PV with respect to normal conditions. In peAF, in addition to APD shortening, RMP dropped from -75 mV to -79 mV, and dV/dt_{max} increased from 163 V/s to 168 V/s for RA, CT, and LA. RMP fell from -68 mV to -78 mV, and dV/dt_{max} rose from 157 V/s to 165 V/s for PV.

APD restitution curves show the behavior of single cells from different regions of the atria. Restitution curves in nSR, showed a decrease of APD_{90} with respect to the diastolic

Table 5.1: Ionic channel conductance and APD_{90}

	RA - PM	CT	BB	RAA	TV	LA	PV	LAA	MV
g_{to}	1.0	0.55	0.5	1.35	1.0	0.25	1.35	1.35	1.0
g_{Kr}	1.0	0.55	0.5	2.0	1.35	4.8	1.6	3.20	0.67
g_{Ks}	1.0	1.0	1.0	1.0	1.6	5.12	1.0	1.0	0.67
g_{CaL}	1.0	1.0	1.0	0.8	0.8	0.3	0.67	0.53	1.25
g_{K1}	1.0	1.0	1.0	1.0	1.0	0.74	1.0	1.0	1.0
Simulated nSR APD_{90} (ms)	236.4	292.8	292.8	241.2	220.0	214.5	176.1	199.5	172.6
Simulated peAF APD_{90} (ms)	165.5	180.2	180.2	141.5	141.5	139.8	120.8	136.2	110.1
Experimental APD_{90} (ms)	207±18 [55]	289±43 [56]	270.0±10	255±45 [57]	173 [47]	200.0 [58]	178.0 [58]	208.12 [59]	158.0 [47]

interval (DI) (Figure 5.3). For nSR, the maximal slope of the restitution curve was 0.77 for the PV. Furthermore, in peAF, the restitution curve's maximal slope was decreased (0.39). Restitution curves for peAF were flattened and shifted in the y axis due to the shortening of APD_{90}.

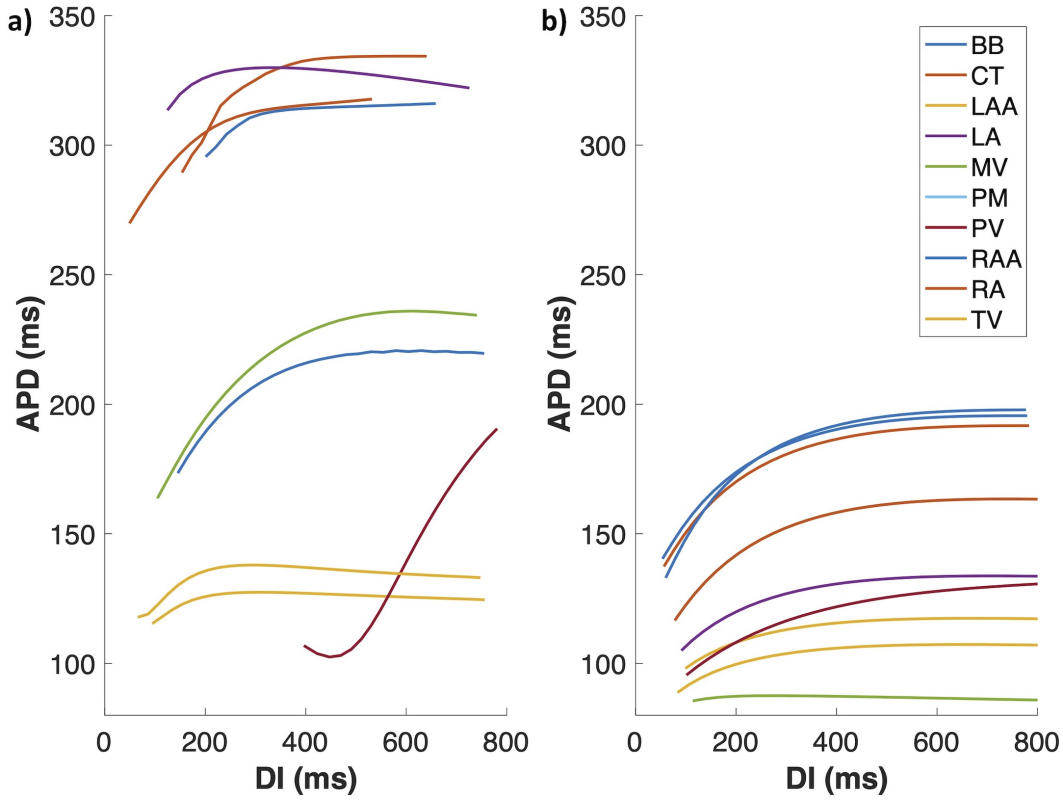

Figure 5.3: Calculated restitution curves for all the different anatomical regions in the human atria. a) Under physiological conditions, there is a considerable heterogeneity in the behavior of the cardiac myocyte in the atria. b) Restitution curves from electrical remodeled myocytes due to persistent atrial fibrillation were flattened, and the dispersion of the curves was reduced.

Figure 5.3a showed that the myocytes from the pulmonary veins had the steppest slope (0.77) and a spatial heterogenity in restution of APD. The steep slope in the PV region is mainly due to the reduced availability of I_{CaL} compared to the other atrial regions. In contrast, due to peAF remodeling the slope is decreased due to the reduction of potassium currents and the spatial hetereogenity in restution curves is reduced for all regions of the atria (Figure 5.3b).

5.3 Discussion

In silico experiments allowed fitting an existing ionic model to reproduce the heterogeneous atrial electrophysiology. Krueger et al. [60] reported the importance of the atrial APD heterogeneity. In this study, we have also incorporated the difference of RMP in atrial cellular electrophysiology. The pulmonary veins exhibit a more depolarized RMP of -68 mV, which is in accordance with several experimental data [61].

The pulmonary vein has a decreased potassium current compared to other regions of the left atria. In the atria, APD heterogeneity is notable between the right and the left atrium. However, the local heterogeneity in the regions of the atria is not considerable. Spatial heterogeneity of the APD has been demonstrated to be pro-arrhythmic and contributes to the pathogenesis of atrial arrhythmias in humans [62], specially in the junction between PV and LA [63]. During atrial fibrillation, the heterogeneity in both sides of the atrium is reduced due to the shortening of the APD in both sides of the atria.

Spatial heterogeneity is a key factor in the physiological function of the atria. Restitution curves of the APD are attributed to the incomplete recovery of ionic currents and concentrations after a previous beat. During the short time between beats the I_{CaL} ionic channel cannot fully recover and the flow of calcium to the sarcoplamic reticulum is not sufficient. Our results of the restitution curves during peAF are in accordance to the results shown by Krummen et al. [64] where APD restitution curves during AF were flattened and with maximal slope less than one. It is expected that the marked increase in APD restitution dispersion would promote greater heterogeneous refractoriness across the atria, and lead to a significant increase in susceptibility of AF especially at rapid heart rates.

Chapter 6

Human atrial myofibroblast electrophysiology

Several models of fibroblasts have been proposed during the past years [65–68]. However, experimental data have shown that there is a difference between atrial and ventricular fibroblasts electrophysiology. Additionally, fibroblasts are heterogeneous cells and their electrophysiology is hard to determine under in vivo experimentation or even in vitro [13, 69]. For that reason, an in silico experiment using genetic algorithms was implemented to optimize the model parameters while maintaining the parameter values within physiological ranges.

6.1 Methods

Using in silico experiments, the parameters of the fibroblast model were determined to reproduce in vivo experiments. In this study, we first investigate the effect of the sodium current (I_{Na}) and the RMP [13, 68, 69]. We introduce the formulation of I_{Na} to the underling fibroblast[68] models according to the experimental results from Poulet et al. [69]. A wide range of 7 initial parameters was fitted. The cost function to minimize was defined in Eq. 6.1.

$$J(\theta) = \sqrt{\frac{\sum_{i=1}^{n}([Ko^{+}](\theta)_{predi} - [Ko^{+}])^2}{n}} + \sqrt{\frac{\sum_{i=1}^{n}(RMP(\theta)_{predi} - RMP)^2}{n}} \tag{6.1}$$

Parameters were constrained to vary 10% from the value originally defined in the model. The constraints assured that the values were kept within reported physiological ranges [65, 67–69]. The fitted fibroblast model was then simulated for 1000 seconds without stimulation to ensure long term stability.

Fibroblasts/myofibroblasts were coupled by Eq. 6.4 which represents the current that flows between cells across gap juntions.

$$C_{myo} \cdot \frac{dVm_{myo}}{dt} + I_{ion-myo} + I_{gap} = 0 \tag{6.2}$$

$$C_{fib} \cdot \frac{dVm_{fib}}{dt} + I_{ion-fib} - I_{gap} = 0 \tag{6.3}$$

$$I_{gap} = \sum_{i=0}^{n} G_{gap} \cdot (Vm_{myo} - Vm_{fib(i)}) \tag{6.4}$$

The genetic algorithm is a stochastic global search optimization algorithm in difficult solution spaces. The algorithm is inspired from biological evolution where fitter individuals are more likely to pass on their genes to the next generation [70].

6.2 Results

The RMP for the fibroblast model was fitted to obtain experimental values [69]. Two different fibroblast's RMP (RMPf) (-45 mV, and -26 mV) were obtained. Moreover, as the fibroblast size differs from the myofibroblast, the membrane capacitance (Cmf) was changed. Two different values, 6.3pF and 50.8pF, were used for the Cmf value for fibroblast and myofibroblast. Values for the myofibroblast are listed in Table 6.1

Table 6.1: Myofibroflast model ionic conductance modifications.

g_{Kv}	g_{K1}	g_{Nab}	g_{NaK}	r_{Kv}	s_{Kv}	P_{Na}
1.75	3	5.22	2.75	15	18	1

Myocyte RMP and dV/dt_{max} (Figure 6.1) coupled to different numbers of fibroblasts were analyzed. Myocyte's RMP (Figure 6.1b) changed similarly when Cmf increased for both RMPf values (-26 mV and -45 mV). Increasing the number of fibroblasts moved the myocyte RMP closer to RMPf value. The most significant change was observed in dV/dt_{max} (Figure 6.1a), which was much lower at an RMPf of -26 mV than the reduction obtained at an RMPf of -45 mV. When fibroblasts are coupled to myocytes their RMP move closer to each other and more Na^+ channels are available, although myocyte Na^+ channel availability is reduced due to a more depolarized RMP depending on the number of coupled fibroblasts.

One myocyte was coupled to one, three or nine myofibroblasts to study the effect on myoycte action potential. The effect of RMP and Cmf is depicted in Figue 6.2. Figure 6.2a shows the effect of the fibroblast RMP on the myocyte's action potential. The myocyte's RMP was highly depolarized with more coupled fibroblasts. Additionally, the Cmf has little effect on myocyte's action potential.

In four characteristic regions of the atria restitution curves were computed to analyze the effect of three myofibroblasts to one myocyte. Figure 6.3 shows how myofibroblasts increase the spatial heteorogenity by reducing APD_{90}. However, in the left atrium, myofibroblasts reduce APD_{90} below 100 ms for DIs below 500 ms.

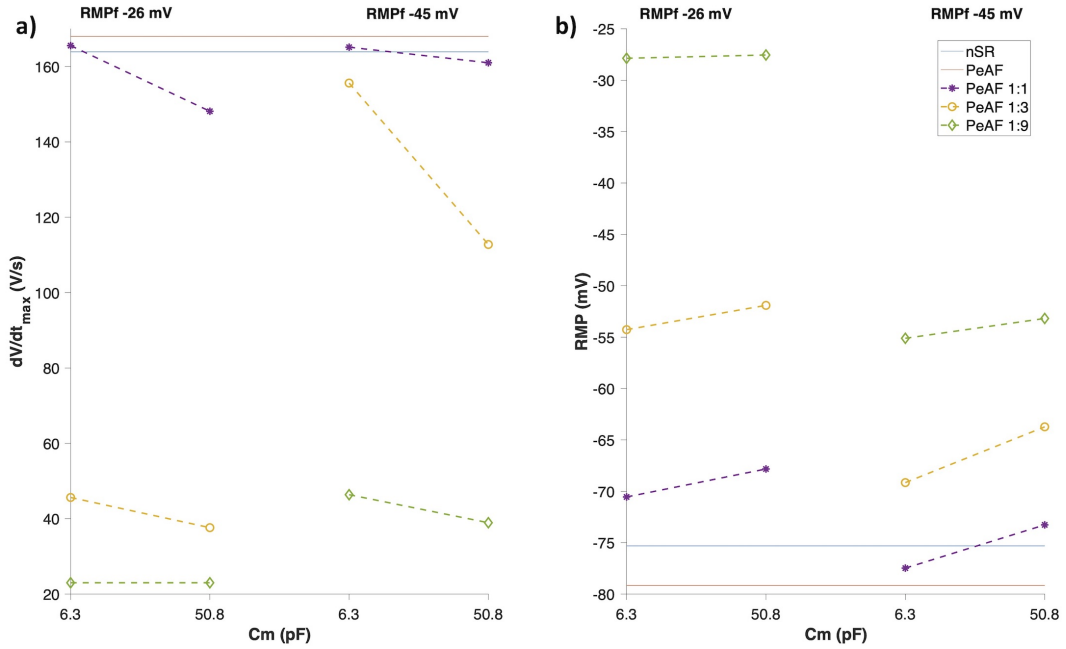

Figure 6.1: Fibroblasts coupling effect on myocyte electrophysiology. a) Myocyte maximum upstroke velocity (dV/dt_{max}). b) Myocyte resting membrane potential (RMP). The levels for myocytes in normal sinus rhythm (nSR) and persistent atrial fibrillation (peAF) conditions are given in blue and red, respectively. Discontinuous lines are myocytes in peAF coupled to one fibroblast (1:1), 3 (1:3), or 9 (1:9).

6.3 Discussion

Atrial tissue is differently affected by peAF remodeling and by the presence of fibroblasts, due to the electrophysiological heterogeneity of the different atrial regions. Our results in isolated single cells show differences in the RMP, dV/dt_{max}, and APD for the four different atrial regions (RA, LA, CT, and PV) in nSR and in peAF. These differences are in agreement with the simulations carried out by Krueger et al. [46], who reported the differential effects of AF remodeling in different atrial regions. It has to be noted that in contrast to the Krueger study, our model presents a long-term stability in all regions in single-cell and tissue simulations and also considers the effect of fibroblast coupling. To our knowledge, this is the first simulation study including the three components (atrial heterogeneity, AF remodeling, and fibroblasts) using a detailed electrophysiological AP model for fibroblasts and focusing on the analysis of the different effects exerted by fibrosis in the different atrial regions. A recent study by Roney et al. [63] showed that high phase singularity density in the PVs favored the effectiveness of PV isolation in ablation procedure. Their model also considered electrophysiological remodeling in AF, electrophysiological heterogeneities in different atrial regions, and fibrosis that was simulated by changes in tissue conductivity. In a previous study [27], the same group modeled fibrosis using different methods and did not consider either electrophysiological heterogeneities in the atrial regions or AF remodeling to determine how different fibrosis models could affect rotor dynamics.

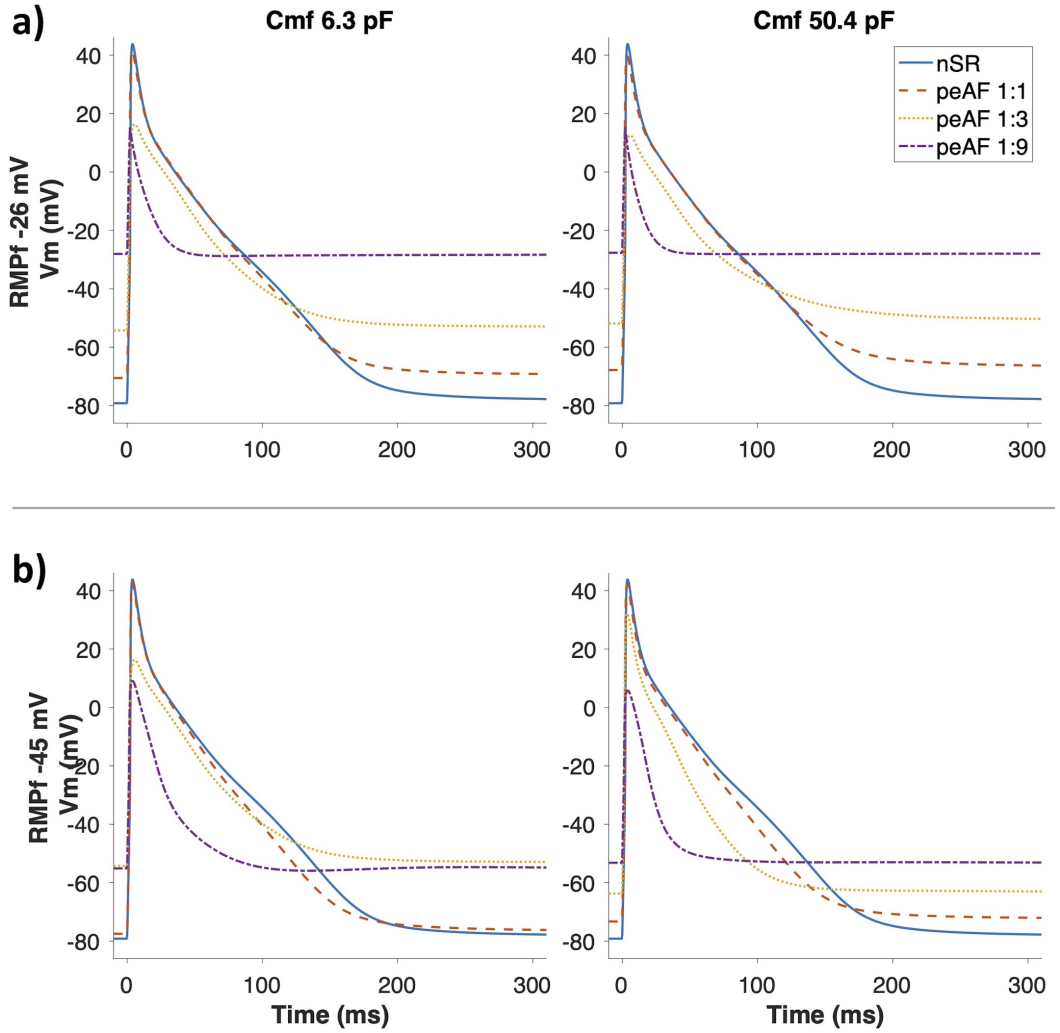

Figure 6.2: Effect of fibroblast and myocyte coupling under persistent atrial fibrillation (peAF) electrical remodeling in RA (baseline model). First and second rows show fibroblasts resting membrane potential (RMPf) of −26 and −45 mV, respectively, for a fibroblast membrane capacitance (Cmf) of 6.3 pF (first column) and 50.4 pF (second column). The different traces are action potentials of isolated myocytes under peAF (blue), one myocyte under PeAF coupled to 1 fibroblast (1:1) (dashed orange), one myocyte under peAF coupled to three fibroblasts (1:3) (dotted yellow), and one myocyte under PeAF coupled to nine fibroblasts (1:9) (dotted-dashed purple).

Different experimental studies show that atrial fibroblasts have a different electrophysiology from ventricular fibroblasts [13, 65, 69, 71]. Morgan et al. [66] found that fibroblast electrophysiology changes the dynamics of an arrhythmic process and provides relevant information on the effect of myocyte-fibroblast coupling in the atria. Our results indicate that RMPf, Cmf, and the number of coupled fibroblasts altered the behavior of myocytes AP, as was found in previous simulation studies [68, 72, 73]. Furthermore, in the present study we found that introducing I_{Na} current into the fibroblast model had an interesting effect; due to the high RMP of isolated fibroblasts I_{Na} current was blocked but when fibroblasts were

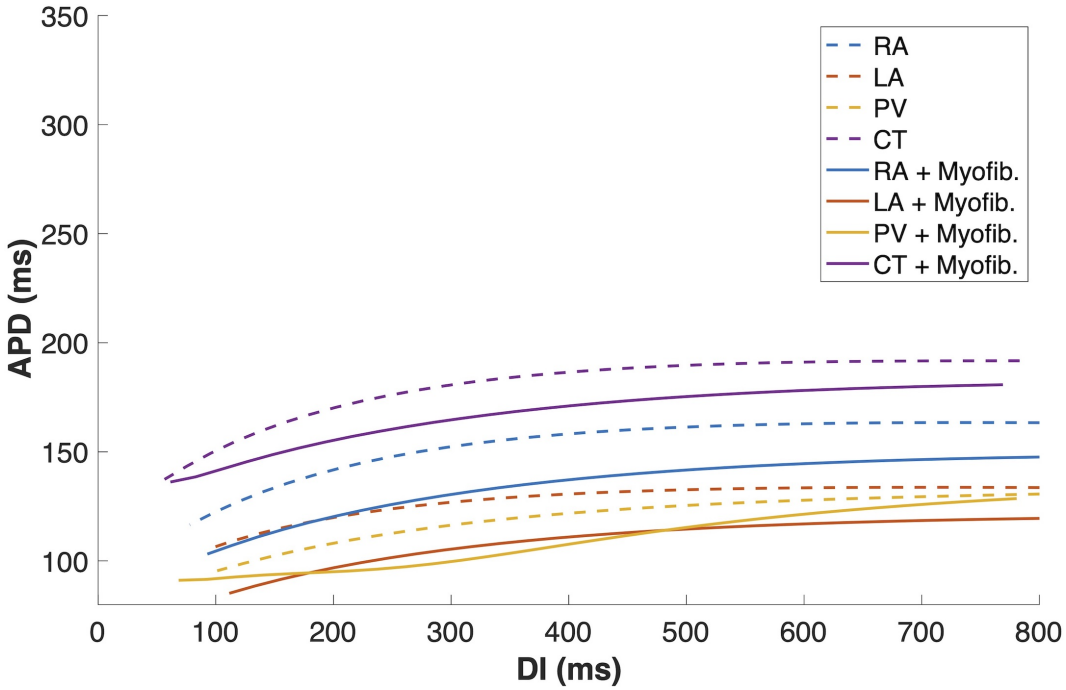

Figure 6.3: Restitution curves calculated for one myocyte coupled to three myofibroblasts (solid lines). Myofibroblasts change the duration of the action potential and increase the atrial tissue heterogeneity compared to non-coupled myocytes (dashed lines).

coupled with myocytes I_{Na} channels became available. Additionally, myocyte-fibroblast coupling led to a partial inactivation of the myocyte I_{Na} due to the higher RMP in the myocyte.

Fibroblast electrophysiology (RMPf and Cmf) changes myocyte AP characteristics [67, 74, 75]. Our simulation results also show that electrical coupling with myocytes increases atrial electrophysiological heterogeneity. Changes in the BCL altered the behavior of the coupled cells, with different responses in different regions. Interestingly, myofibroblast-myocyte coupling in regions with higher I_{K1} and I_{CaL} (RA and CT) exhibited more sensitivity to changes in frequency, while regions with smaller I_{K1} and I_{CaL} (PV) developed no AP for any of the BCLs. In contrast to McDowell et al. [76], we defined different electric characteristics for atrial myofibroblasts, which have a different effect on myocyte AP. Myofibroblasts act as the current source, raising the myocyte RMP [75] depending on the number of coupled myofibroblasts [67, 68], thus leading to a partial inactivation of the myocyte I_{Na} current.

Chapter 7

Myofibroblast Ca^{2+} current and intracellular Ca^{2+} handling

Calcium dynamics in contractile cells play a key role in electrophysiology. Recent experimental data have shown that the ionic calcium channel in the myofibroblast membrane changes the electrophysiological behavior of this cell [77–79]. Therefore, in this chapter in silico experiments exploring the presence of I_{CaL} are presented.

7.1 Methods

Recent experimental studies have shown that myofibroblasts exhibit α-smooth proteins and are able to contract [80]. Based on this result, we hypothesize the myofibroblast need calcium to contract and the presence of a calcium ionic channel and intracellular calcium handling system. Recent studies have shown that ionic channels permeable to calcium are present in the myofibroblast membrane[78, 79]. Therefore, we used the genetic algorithms explained above to explore the influence of the calcium current in the electrophysiology of the myofibroblast. The number of variables to be fitted was 13. The cost function (Eq. 7.1) was then adjusted to minimize the error between the experimental curves for I_{CaL} calcium current and the simulated data. Additionally, $[K^+]o$ was also considered in Eq. 7.1 to ensure long term stability and maintain the value within physiological ranges.

$$J(\theta) = \sqrt{\frac{\sum_{n=1}^{n}(I_{CaLpredi} - I_{CaL})^2}{n}} + \sqrt{\frac{\sum_{n=1}^{n}([Ko^+](\theta)_{predi} - [Ko^+])^2}{n}} \tag{7.1}$$

A second step was to include intracellular calcium handling. Since differentiated myofibroblasts exhibit similar phenotypes to the surrounding myocytes in cardiac tissue, Courtemanche et al. [81] human atrial model was used to formulate the intracelullar calcium handling system and was included in the human atrial myofibroblast model. Parameters of the intracellular handling system were constrained to vary $\pm 10\%$ from their established values in a human atrial cardiomyocyte model. Parameters with variation less than $\pm 1\%$

were taken out to reduce the parameter search space and increase the speed of the genetic algorithm.

Additionally, three, six, or nine myofibroblasts with only the I_{CaL} ionic current or with the I_{CaL} ionic current and the intracellular Ca^{2+} were coupled to one myocyte to explore the effect on APD as described in Chapter 6.

7.2 Results

The fitted parameters for I_{CaL} are in the range of the available experimental data [79]. The modified parameters for the I_{CaL} with the intracellular Ca^{2+} handling system are listed in Table 7.1. The fitted I_{CaL} parameters' error was below 1% with respect to experimental patch clamp data (Figure 7.1). Figure 7.1 depicts the result of the fitted I_{CaL} (blue trace) with respect to the experimental values (white dots).

Table 7.1: Myofibroflast model including the I_{CaL} with the intracellular Ca^{2+} handling system ionic conductance modifications.

g_{Kv}	g_{K1}	g_{Nab}	g_{NaK}	r_{Kv}	s_{Kv}	P_{Na}	g_{CaL}	K_{NaCa}	g_{Cab}	K_{pCa}	f_L	d_L
1.34	1.79	2.39	0.84	14.04	16.21	0.73	0.48	2.55	0.57	1.0	1.0	1.0

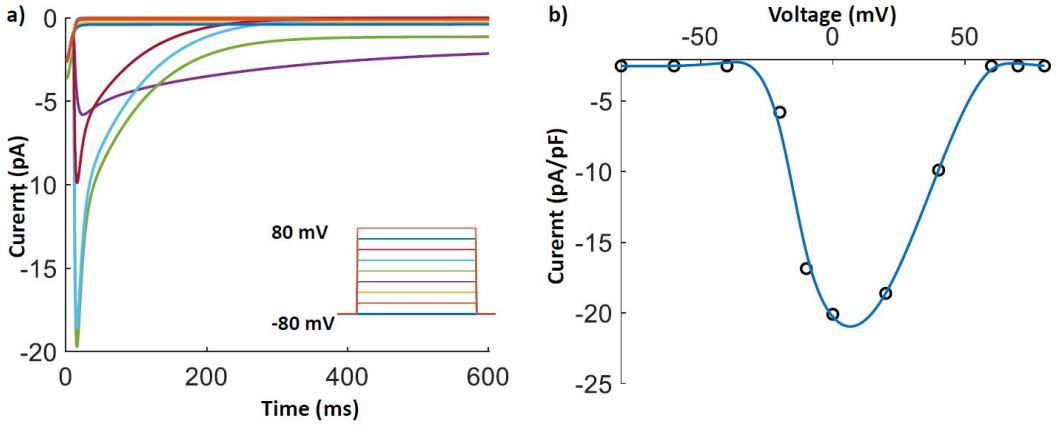

Figure 7.1: Fitted myofibroblast I_{CaL} according to experimental data. a) Voltage clamp experiments of the I_{CaL} where the behavior of the current is shown at different voltages. b) White dots represents the maximum current value of I_{CaL} with respect to the experimental data[79] (blue curve).

Figure 7.2 depicts myofibroblast transmembrane voltage. At its resting state, the myofibroblast RMP is constant at a value of -26 mV. In the presence of I_{CaL}, the myofibroblast exhibits automaticity. The transmembrane voltage range is from -46 mV to 26.5 mV. The triggered activity has a constant cycle length of 100 ms. When the intracellular handling

system was included, the automaticity of the myofibroblast ceased. The calcium ions which were not pumped out of the cell by NCX, were now pumped by the I_{pCa} and taken inside the sarcoplasmic reticulum, and I_{CaL} was not activated, yielding a RMP of -46 mV.

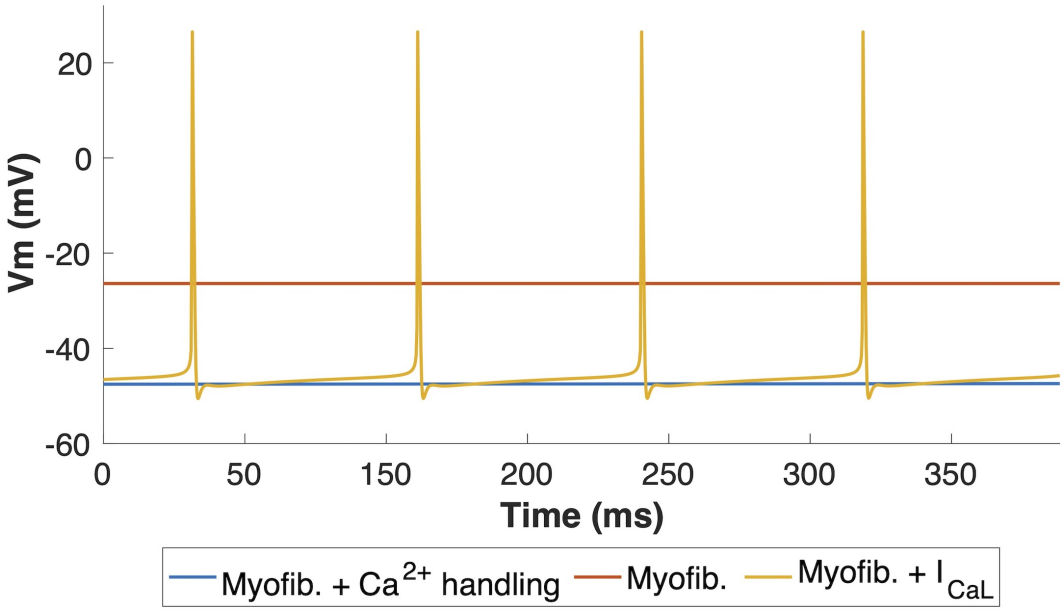

Figure 7.2: Myofibroblast transmembrane potential without stimulation. The red trace shows the transmembrane potential of the myofibroblast without I_{CaL}. The yellow trace shows the transmembrane potential and the automaticity that the myofibroblasts exhibit when I_{CaL} ionic current is included. Blue trace indicates the myofibroblast transmembrane potential with I_{CaL} and the Ca^{2+} intracellular handling system.

The system of ordinary equations is not linear. The presence of I_{CaL} and the intracellular Ca^{2+} changed the net current flux across ionic channels. Due to a decrease of 50% in the flux of I_{K1} the RMP has a more negative RMP with respect to the control myofibroblast model. During the resting state, the net flux across the different ion channels changed. The control myofibroblast model at resting state has a total flux of potassium ions through the ionic channels of 6.76 C/s, which helped reach the RMP of -26 mV. When I_{CaL} was introduced in the myofibroblast, the net flux of K^+ was decreased. The automaticity of the cell was mainly driven by a constant exchange of potassium from the intracellular and extracellular medium since the I_{CaL} channel was deactivated for a RMP of -46 mV (Figure 7.3).

Figure 7.4 shows the results of in silico experiments exploring the coupling of myofibroblast model with I_{CaL} and intracellular Ca^{2+} handling to one myocyte. Single myocytes electrophysiology was less affected when coupled to three, six, or nine myofibroblasts compared with the effect of coupling the baseline myofibroblast model. Myocytes APD_{90} was less affected, and the RMP was less hyperpolarized (from -74 mV to -60 mV). With a myocyte RMP of -60 mV or more, sodium ion channels were available, and the myocyte can trigger a complete action potential.

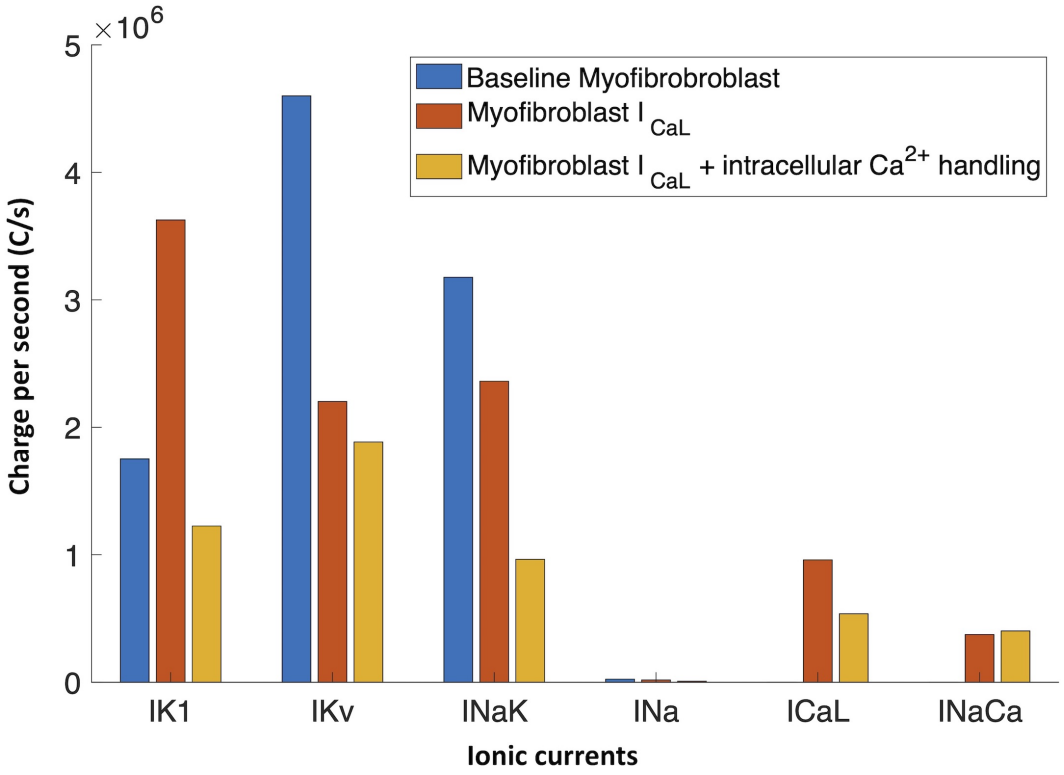

Figure 7.3: Current across the different ion channels in the membrane of the myofibroblasts. The ionic currents exhibit different dynamics, and the influx and efflux of K^+ mainly drives the behavior of the cell.

7.3 Discussion

In vitro and in vivo studies have shown that the number of myofibroblasts and collagen in rat hearts were reduced by blocking L/T-type Ca^{2+}channels [82–84]. These studies suggest that Ca^{2+} ion channels and calcium intracellular handling plays an essential role in the electrophysiology of myofibroblasts and the understanding of the development of cardiac fibrosis.

Miragoli et al. [15] have shown myofibroblasts' automaticity. The results presented in this study are in accordance with previously mentioned experimental data. The myofibroblast model with I_{CaL} shows automatic activity mainly driven by the voltage-activated potassium channels due to the small conductance of I_{K1} [85]. However, by introducing the intracellular Ca^{2+} handling system, the autonomic activity ceased due to the regulation of the Ca^{2+} in the intracellular space, which regulates the function of the NCX exchanger and the NaK pump.

Moreover, when the intracellular handling system was introduced, the autonomic activity stopped. However, it is worth noticing that the RMP was -46 mV. This finding is in accordance with the RMP reported in different studies [69, 80]. The wide range of RMP reported

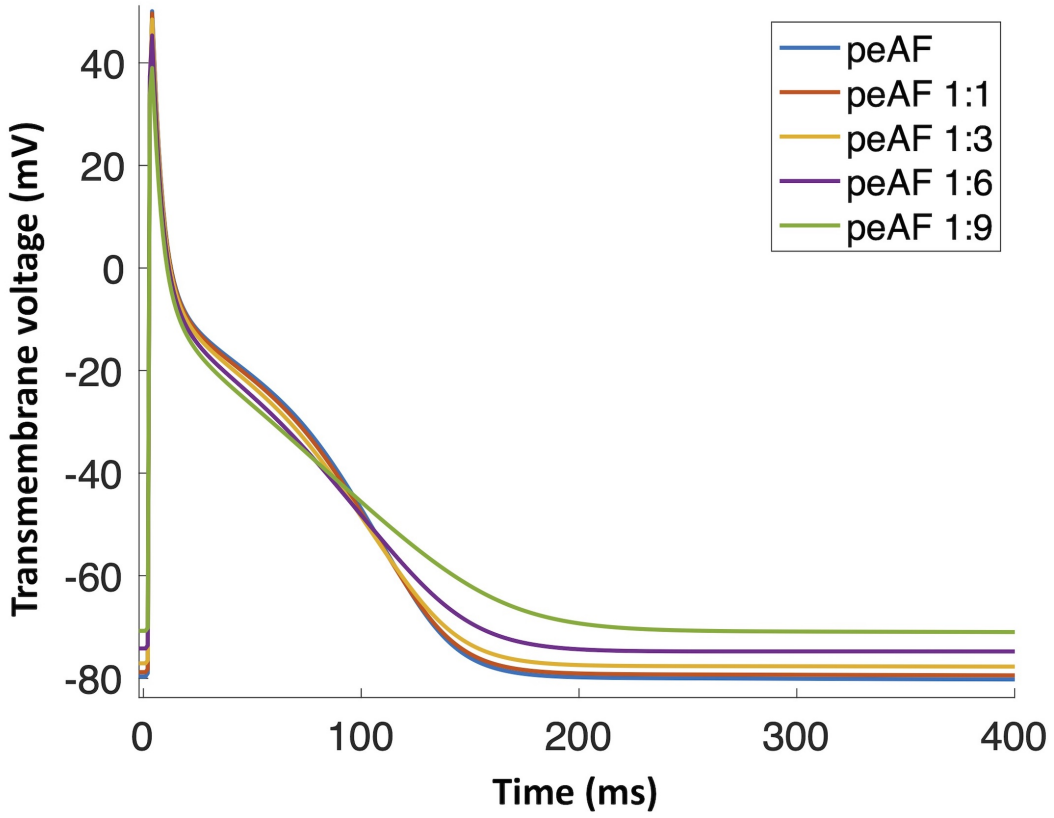

Figure 7.4: Myocyte action potential without myofibroblast coupling under the electrical remodeling due to persistent atrial fibrillation (blue trace). The myocyte was then coupled with one, three, six, and nine myofibroblasts with I_{CaL} and intracellular Ca^{2+} handling. Six or nine coupled myofibroblasts highly influence the myocyte's action potential duration and the resting potential.

experimentally can be due to the differentiation of fibroblast into myofibroblast and their phenotype.

A better understanding of the fibroblasts' electrical properties should lead to an improved comprehension of AF pathophysiology and a variety of novel targets for antiarrhythmic intervention. The presence of calcium current and intracellular handling system is an important factor that needs to be explored in more detail.

PART III

TISSUE LEVEL

Chapter 8

Myofibroblast infiltration

Myofibroblasts have been shown to disturb the electrical conduction in the cardiac tissue [15, 86]. Previous results from single cell simulations have shown how myofibroblasts can alter the myocyte action potential [36, 87]. Therefore, this chapter covers the in silico simulations at tissue level that study the role of the electrical coupling between myocytes and myofibroblasts in cardiac tissue.

8.1 Methods

Using 1D tissue strands, the aim of this study was to analyze the effect of myofibroblast infiltration on conduction velocity. One dimensional (1D) detailed tissue strands were created with different element sizes to account for the differences between myocytes and fibroblasts. Diffusion coefficients were then calculated considering the physiological size of each cell, as shown in Eq. 8.1 [88].

$$D = \frac{1}{\rho S C_{\mathrm{m}}} \tag{8.1}$$

where D is the diffusion coefficient, ρ is the cellular resistivity, S is the surface-to-volume ratio of the cell, and C_{m} is the membrane capacitance.

To simulate tissue strands under physiological conditions and sinus rhythm, the diffusion coefficient was tuned to achieve realistic conduction velocities of the cardiac tissue [47]. In addition, four different densities of myofibroblasts (10%, 20%, 40%, and 60%) were uniformly randomly distributed in the fiber. Tissue strands were stimulated from the right side with ten pulses at a basic cycle length of 1000 ms.

Two-dimensional (2D) tissue patch meshes of 5 cm x 5 cm, representing cardiac tissues were built with a central region of 2 cm diameter. In the tissue central region, four different densities of myofibroblasts (10%, 20%, 40%, and 60%) were uniformly randomly distributed. To minimize the effect of the random distribution, ten different realizations for each density were created.

Additionally, a cross-shock (S1-S2) protocol was used to quantify the structurally remodeled cardiac tissue vulnerability to initiate and maintain an arrhythmia (Figure 8.1). The tissue was stimulated from the left border with five pulses (S1). S1 was paced at a basic cycle length of 1000 ms to stabilize the tissue. Afterwards, an S2 stimulus at the end of the refractory period was applied at the left lower quarter of the tissue to induce a reentry.

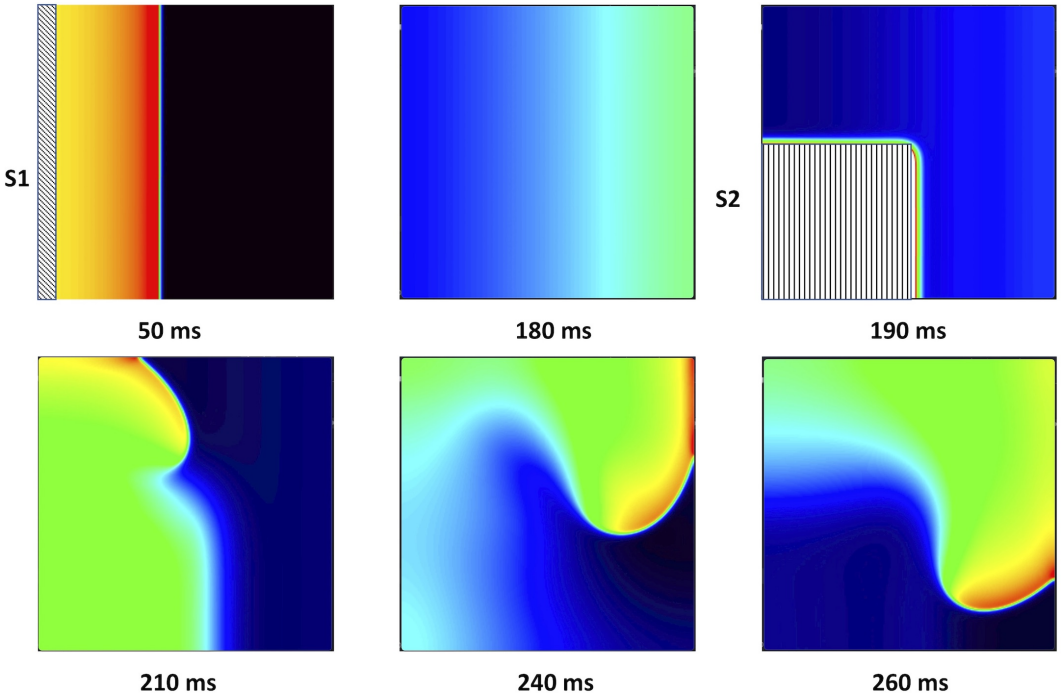

Figure 8.1: Snapshots in time explaining the cross-schock (S1-S2) protocol. The first panel (left upper corner) shows the S1 pulse and the depolarization wave. At 180 ms, the tissue cells are finishing their repolarization phase, and then at 190 ms, a second stimulus (S2) was introduced in the lower left quarter of the tissue to induce a reentry. From the time 210 ms, it is possible to observe the reentry activity's progression and maintenance in the cardiac tissue.

Looking for an S2 that creates a sustained reentry is a tedious job. A function was created to automate the search of the right time to introduce the S2 stimulus. The function traced one node's action potential and calculated APD_{90} of one given node. Then S2 was applied, and then, using a bisection algorithm, different S2 are tested. The function then looks at the action potential trace from four given nodes to define a sustained reentry. A sustained reentry was defined as electrical tissue activity longer than 1 s. If the reentry was sustained for 1 s or longer, the S2 time was considered to calculate the tissue's vulnerability time window to arrhythmia. Phase singularities (PSs) detection was used to obtain the instantaneous location of the reentry [89, 90]. Phase maps based on the Hilbert transform (HT) of the APs were created [91, 92] by computing the instantaneous phase θ, which values ranged from -π to π radians:

$$HT|Vm(t)| = \frac{1}{\pi}\int \frac{Vm(\tau)}{t-\tau}\,d\tau$$

$$\theta = tan^{-1}(\frac{HT|Vm(t)|}{Vm(\tau)})$$

where Vm is the transmembrane potential. Then PSs, where all phases converge (7), were computed to track the rotor trajectory:

$$\oint \nabla\theta dr = \pm 2\pi \tag{8.2}$$

Detected PSs were also used to assess the heterogeneity degree in the tissue due to the inclusion of fibrotic regions following the trajectory of the reentry tip.

Finite element monodomain simulations were ran using GPUs [36]. Meshes with quadrilateral elements with a resolution of 100 μm were created, and time discretization of 1μs was used.

8.2 Results

Electrical remodeling of atrial fibrillation has already an impact on the tissue conduction velocity. Tissue strands show how myofibroblasts alter the local conduction velocity of the cardiac tissue (Figure 8.2).

During nSR and without fibroblasts, the RA has a CV of 70 cm/s, CT has a CV of 100 cm/s, LA has a CV of 70 cm/s, and PV has a CV of 80 cm/s (discontinuous blue lines). AP propagation along the strand was affected by peAF electrical remodeling (discontinuous red lines), and CVs dropped significantly. At higher fibroblast (dark grey) or myofibroblasts (light grey) densities in the strand, CV dropped. Boxplot measurements of the CV were represented for the 100 random distributions of fibroblasts for each density (10%, 20%, and 40%). The region with the greatest differential effect on the CV was the PV, depending on whether the distribution was with fibroblasts or myofibroblasts. PV also experienced conduction blocks in some of the random distributions (indicated by blue asterisks). Conduction block was also seen in the LA at a density of 40% in some distributions.

Tissue simulations were run to quantify the tissue vulnerability to reentry under atria fibrillation electrical remodeling and in the presence of myofibroblasts with different densities. Figure 8.3 shows snapshots of phase maps (taken at the same time). Reentrant circuits can be seen in the RA (top panels) and the LA (bottom panels) in peAF remodeling and increasing levels of myofibroblast density from left to right (membrane potential snapshots can be seen in Supplementary Figure S4). In the absence of myofibroblasts, a functional reentry was obtained in RA and LA. The tip of these rotors (Figure 8.3, first column), corresponding to the PS superimposed in white on the phase maps, describes a regular circular path, which agrees with the results obtained in previous simulation studies [93]. In the LA, the rotor tip describes a smaller path due to the shorter wavelength caused by shorter LA ERP [46, 47, 94].

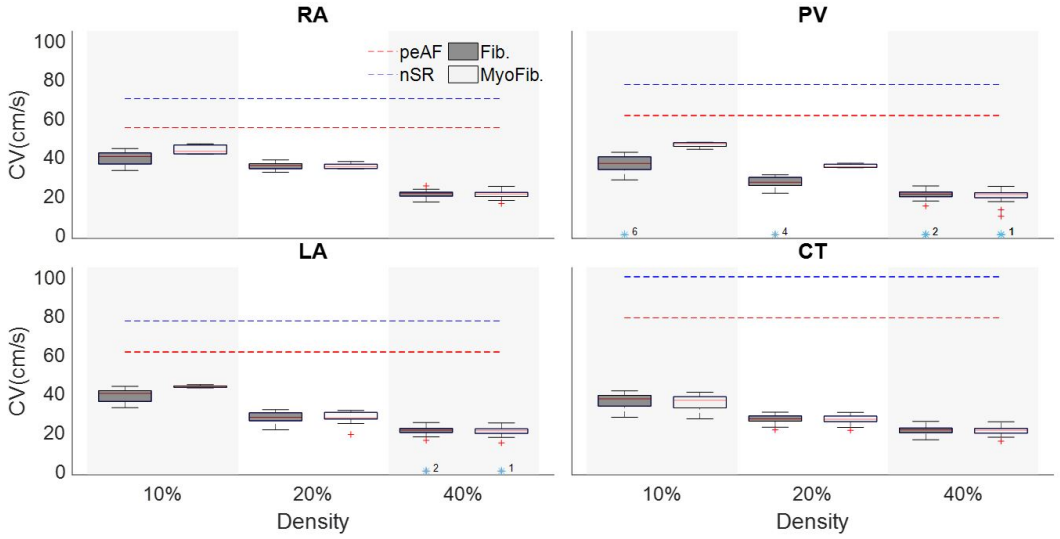

Figure 8.2: Conduction velocity (CV) of a tissue strand in four different regions of the atria with random fibroblasts (Fib) or myofibroblast (MyoFib) distribution and different fibroblast densities. For each density 100 random configurations were simulated. CV measurements are represented in boxplots. (A) Right atria (RA). (B) Pulmonary vein (PV), (C) Left atria (LA), and (D) Crista terminalis (CT). Adapted from [36]

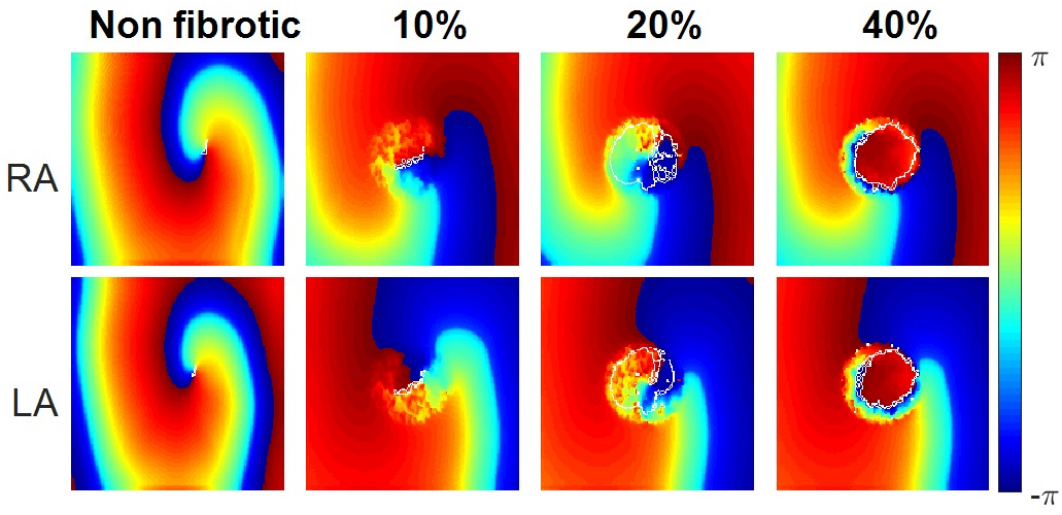

Figure 8.3: Instantaneous phase maps and phase singularities (in white) for different densities of myofibroblasts (non-fibrotic, 10%, 20%, and 40%) in the right atria (RA) and left atria (LA) under conditions of persistent AF remodeling. Adapted from [36]

When myofibroblasts were present in the center of the tissue, the obstacle altered the reentrant activity. Small percentages of myofibroblasts (10%–20%) allowed the wavefront to propagate through the fibrotic region, but the electrophysiological heterogeneities of myofibroblasts and myocytes caused wave breaks, which were detected as PSs. However, propagation in the fibrotic region was practically blocked when myofibroblast density was

raised to 40%, which produced an anatomical reentry surrounding the fibrotic obstacle. Since the wavefront did not propagate through the fibrotic region, the number of wave breaks was significantly reduced, as were the number of PSs detected.

The myofibroblasts in the tissue increased vulnerability to reentry, measured as the vulnerable window (VW), a time interval for which premature S2 stimulation generates a reentry (Figure 8). In the RA, the vulnerable window in the absence of myofibroblasts was 37 ms. When myofibroblasts density was raised to 10%, the VW increased to 38 ± 0.0 ms. The VW also increased (39 ± 0.63 ms) when density was raised to 20%, but at 40%, the VW dropped below the control value (35 ± 0.82 ms). Interestingly, LA was more sensitive to myofibroblasts with a larger VW than the RA. The LA VW, in the absence of myofibroblasts, was 40 ms. When myofibroblasts density was raised to 10%, the VW rose to 40 ± 0.10 ms, at 20% it increased to 40.5 ± 0.53 ms, and at 40% it dropped to 38 ± 0.88 ms.

8.3 Discussion

Structural remodeling in cardiac tissue contributes to the reduction of conduction velocity, delaying regional functional activations, and increasing structural heterogeneities, which are essential factors for establishing a reentrant driver or conduction block [2]. Our results show that fibroblasts and myofibroblasts can alter the activation time in a 1D tissue strand, in agreement with different studies [6, 95]. One hundred random configurations for different fibroblasts/myofibroblasts densities in the four atrial regions were implemented. Zhan et al. [96] showed that fibroblasts can alter the CV and can lead to blocks in conduction with fibrosis densities of 40% and 45%. Our results showed that a high density (40%) led to conduction blocks in the LA and that the PV was the most sensitive region to the presence of fibroblasts-myofibroblasts. Similarly, in an experimental study, Miragoli et al. [15] showed that myofibroblast proliferation changed the tissue conduction velocity and myocyte dV/dt_{max}. Our results showed a reduction in CV, in agreement with several other experimental and simulation studies that found that fibroblasts-myofibroblasts can establish an electrical coupling with myocytes, reducing their dV/dt_{max} and activation time, reflected in reduced CV [6, 8, 15, 97]. We also found a monotonic reduction in all four atrial regions.

Tanaka et al. [98] have shown that local fibrosis distribution reduces CV in the different atrial regions, in agreement with our results, which showed a reduced CV with a tendency to homogenize in all four atrial regions. CV heterogeneity is responsible for giving the atria the characteristic activation times [99]; if all the regions were to have a homogenous CV, this might induce the appropriate conditions for reentrant rhythms and conduction blocks [100]. As the fast conduction systems (CT) conduction velocity was significantly reduced, this may be an interesting AF mechanism in the right atrium.

Structural remodeling and endo-epicardial dissociation alter the atrial substrate and could produce macroreentries and focal activity [101, 102]. When the propagation was analyzed in different regions of the atria and at different myofibroblast densities, it was found that a low myofibroblasts percentage increased the number of PSs due to wave breaks. However, at

higher percentages, propagation through the fibrotic zone was blocked, the number of wave breaks and PSs decreased, and an anatomical reentry was anchored around the fibrotic zone, in agreement with previous studies [27, 76]. Several simulation studies have also shown that reentry dynamics are altered by heterogeneities of the AP in the cardiac tissue [61, 103], the presence of fibroblasts [66, 104, 105], and that PSs increase in the zones with fibroblasts [25].

Waks and Josephson [106] demonstrated that the rotation dynamics depend on the atrial region (RA or LA) and its electrophysiological characteristics, as did we in the present study in which vulnerability to reentries and the dynamics of the rotation depended on the atrial region. LA presented slightly wider VWs, due to its shorter APD.

Gomez et al. [107] showed that the density of fibroblasts had a biphasic impact on the ventricular vulnerable window for reentry. Moreover, our results showed the same VW biphasic behavior for the first time in atrial tissue. Krul et al. [108] found that local fibrosis is associated with reentrant activity, in accordance to our results at low fibroblast density (10%), considered as a region of local diffuse fibrosis, which presented higher vulnerability to reentry and resulted in multiple wave breaks. When myofibroblast density was raised (20%), tissue vulnerability to reentry rose, and conduction blocks occurred. However, at higher densities (40%) conduction blocks also occurred, but the VW dropped, as was found by Campos et al. [109]. This suggests that myocyte-fibroblast coupling in peAF plays an essential role in AF electrical propagation [110], with different effects in different atrial regions.

Chapter 9

Fibrosis composition

Cardiac and lung fibrotic diseases cause over 800,000 deaths per year worldwide [12]. The fibrotic process is complex and several cellular mediators and signalling pathways are involved (Figure 9.1).

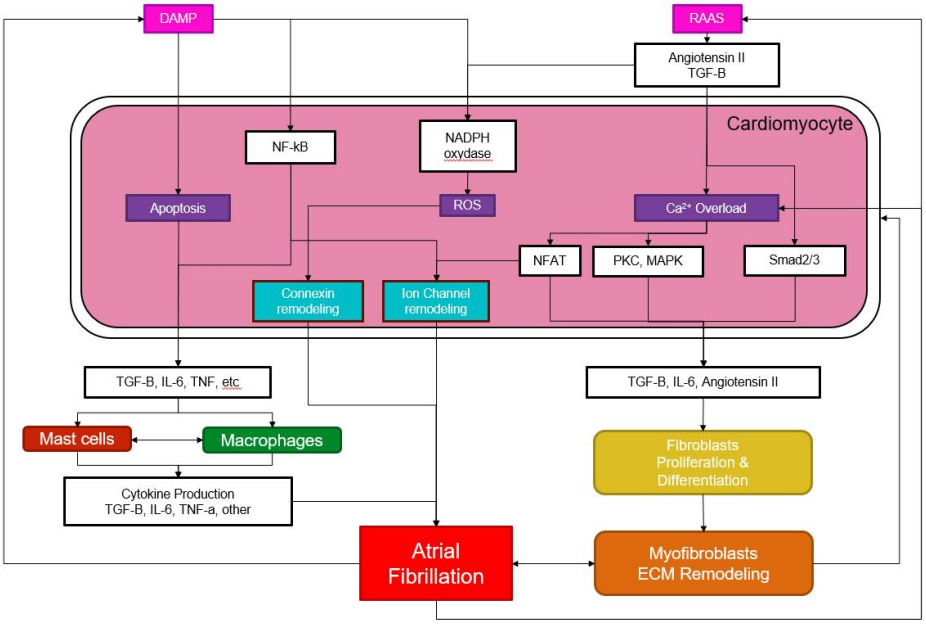

Figure 9.1: Atrial fibrillation (AF) is a complex pathology and inflammation plays a role in the initiation and maintenance of AF. Danger-associated molecular patterns (DAMP) or alterations in the Renin-Angiotensin-Aldosterone System (RAAS) trigger a cascade of reactions in the cardiac myocyte, which results in a remodeling of gap junctions and ionic channels. Additionally, cardiac myocytes segregate cytokines such as TGF-β1, which recruit mast cells and macrophages. Furthermore, TGF-β1 also triggers the differentiation of fibroblasts into myofibroblasts which deposit collagen and are responsible for the extracellular remodeling.

Cardiac fibrosis has been classified as a cardiomyopathy, and its composition varies from patient to patient. In cardiac fibrosis, differentiated fibroblasts or myofibroblasts are mainly

responsible for structural remodeling. Experimental studies have shown that myofibroblasts derived from AF patients display different phenotypes compared to those patients in the healthy control group [69]. Differentiation of fibroblasts can be triggered by paracrine signalling from myocytes or other cells in the cardiac tissue. The paracrine signalling of cytokines, such as transforming growth factor β 1 (TGF-β1), interleukin 6 (IL-6), and tumor necrotic factor alpha (TNF-α) are segregated by myocytes, fibroblasts and macrophages, this process is known as inflammation. Myofibroblasts alter the extracellular medium, depositing protein fibers (collagen I, collagen III) to maintain the cardiac tissue's integrity. Using confocal microscopy, Greiner et al. have shown, with a high level of resolution, the composition of fibrotic tissue where different types of cells are found [111].

In this chapter, the fibrotic composition was varied, and the effect on electrical propagation and the electrograms was quantified. Part of this work was presented as a conference contribution [112].

9.1 Methods

Two-dimensional (2D) patch meshes of 5 cm x 5cm x 0.2 cm (Figure 9.2), representing cardiac tissues were built with a central *structurally remodeled* region of 2 cm diameter. In the central region of the tissue, different tissue properties arrangements were simulated to study the effect of myofibroblasts coupling, the inflammatory paracrine remodeling and the deposit of collagen fibers. Within the region, myofibroblasts and collagen were randomly distributed with different ratios (0%-100%, 25%-75%, 50%-50%, 75%-25% and 100%-0%). TGF-β1 paracrine remodeling was represented by modifying ion channel conductances, 50% reduction in I_{K1}, 50% reduction I_{CaL}, and 40% reduction in sodium current I_{Na} [11]. The mesh was conformed by tetrahedral elements with an average length of 100 μm to capture the details of collagen deposit in the cardiac tissue.

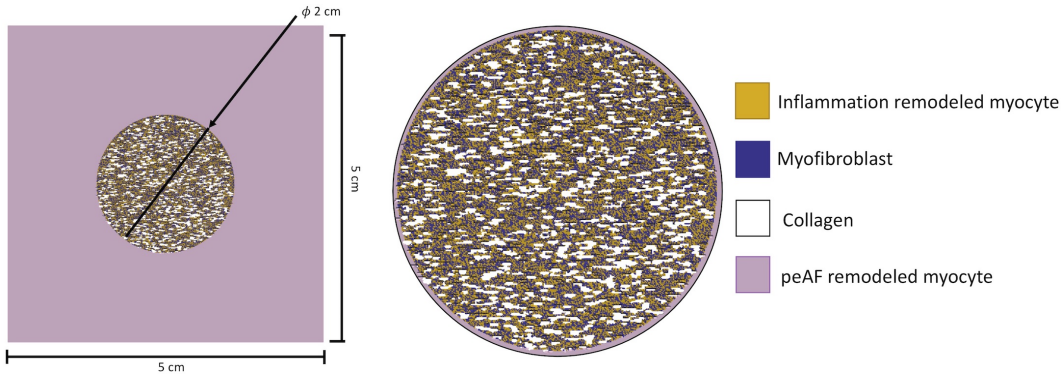

Figure 9.2: Dimensions of an atrial tissue patch of 5 cm x 5cm x 0.2 cm with a circular area of 2 cm of diameter. The circular region has different cells: myocytes affected by persistent atrial fibrillation (pink) and inflammation (yellow). Additionally, myofibroblasts (blue) and collagen fibers were modeled as empty cylindrical holes in the cardiac tissue (white).

Additionally, collagen was modeled as cylindrical strands to mimic the texture reported in interstitial fibrosis during AF [101]. Moreover, percolation has been described to better reflect the findings in experimental data [26, 63]; therefore elements representing collagen were taken out creating empty spaces in the mesh.

Reentry was initiated using a cross-shock stimulation and PSs were quantified. Additionally, pseudo-unipolar equally spaced (1 mm) electrograms were computed at the surface of the tissue using the infinity volume conductor approximation Eq. 9.1.

$$\phi = \frac{1}{4\pi\sigma} \iiint_V \frac{I_{src}}{||x - x_{src}||} dV \tag{9.1}$$

where σ is the conductivity coefficient of the medium, I_{src} is the current density and $||x - x_{src}||$ is the Euclidean distance from the source point to the measuring point. Bipolar EGMs were calculated from two unipolar EGM with a spacing of 1 mm (Figure 1, panel B). The criteria for fractionation were based on the duration of the active segment of the signal using the Nonlinear Energy Operator (NLEO) algorithm described by Schilling et al. [113] and the Shannon Entropy [114]. Signals with peak to peak values below 0.5 mV were not considered for the calculations.

9.2 Results

When the fibrotic density was low (10% and 20%), the excitation was able to propagate across the fibrotic region (Figure 9.3a). In contrast, for higher density (40%), conduction was blocked in this region (Figure 9.3a). Reentry changed gradually from functional to anatomical due to block of conduction. Figure 9.3b shows a biphasic behaviour of the number of PSs quantified with different compositions of the fibrotic area. For all densities the maximum amount of PSs was achieved for a proportion of 50% of myofibroblasts and 50% of collagen in the cardiac tissue.

EGMs in Figure 9.4 show the different morphologies inside and outside of the fibrotic region. Depending on the myofibroblast-collagen ratio, EGM's morphology is also affected. Additionally, the EGM morphology outside of the fibrotic area did not change significantly. EGM activity duration increased inside the fibrotic region compared to the duration at the outside of this region. For the fibrotic density of 10% we detected segments with shorter duration (45.21±1.24 ms). Increasing fibrosis density (20%) increased the duration of the segments (60.73±1.10 ms), and for higher density of fibrosis (40%), segments were shortened again with a duration of (46.59±1.29 ms) or inactivity near the core.

Figure 9.5 shows the difference in duration of the active segments and Shannon entropy found inside and outside of the fibrotic region. Fibrotic regions with a lower percentage of myofibroblasts (below 50% compared to the percentage of collagen) had active segments with shorter duration. When increasing the percentage of myofibroblast densities (above 50% compared to the percentage of collagen), propagation exhibited a slower frequency of activation, which was reflected in segments with a longer duration of activity.

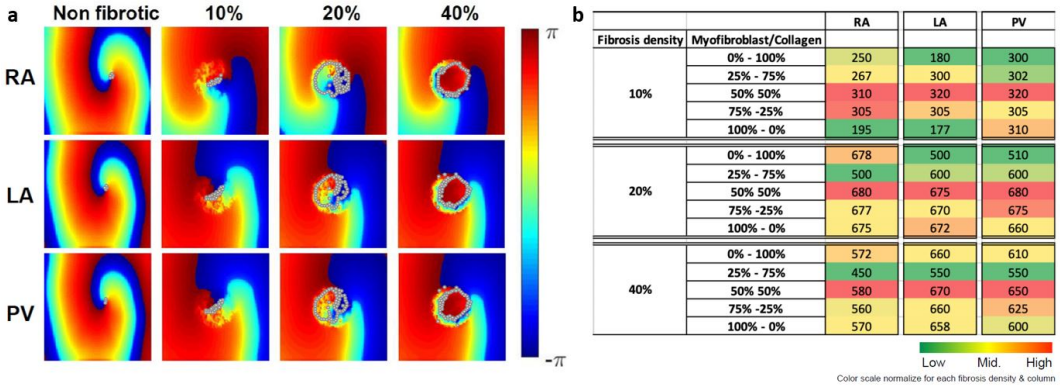

Fibrosis density	Myofibroblast/Collagen	RA	LA	PV
10%	0% - 100%	250	180	300
	25% - 75%	267	300	302
	50% 50%	310	320	320
	75% -25%	305	305	305
	100% - 0%	195	177	310
20%	0% - 100%	678	500	510
	25% - 75%	500	600	600
	50% 50%	680	675	680
	75% -25%	677	670	675
	100% - 0%	675	672	660
40%	0% - 100%	572	660	610
	25% - 75%	450	550	550
	50% 50%	580	670	650
	75% -25%	560	660	625
	100% - 0%	570	658	600

Figure 9.3: a) Snapshot of a single time frame for three tissue patches from the right atria, left atria, and pulmonary vein. The first column depicts a reentry activity without fibrosis. The second to fourth columns show how reentry dynamics change due to the presence of fibrotic tissue. b) Different fibrotic compositions change the reentry dynamics, where a mixture of myofibroblasts and collagen exhibit a high density of singularity points.

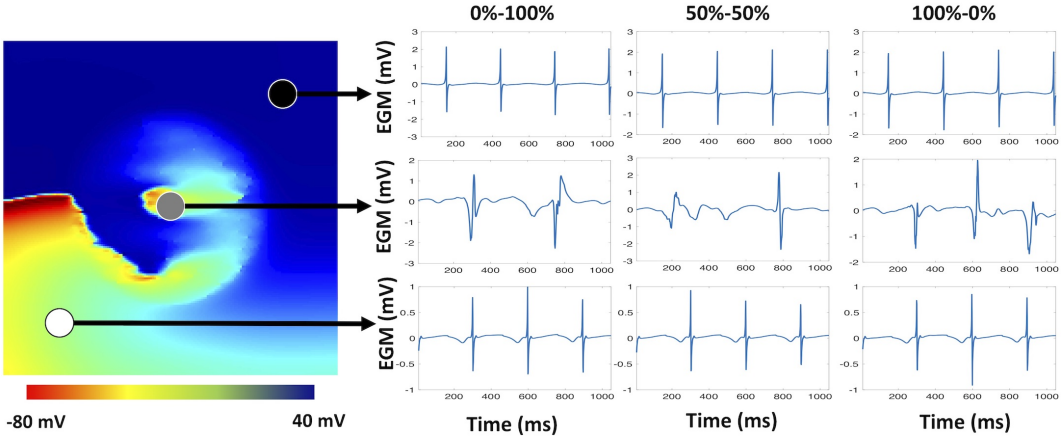

Figure 9.4: Electrograms calculated at the surface of the cardiac tissue. White and black dots show the signal at the outside the fibrotic area where the signal is not affected by fibrosis composition. The gray dot shows how the electrogram computed at the core of the fibrotic tissue is affected due to its composition. Fractionated signals were mainly found with a mixture of myofibroblasts and collagen. Adapted from [112]

.

For simulations with 40% fibrotic density, we were not able to detect any activity near the core. This center of the fibrotic region had an EGM with a smaller peak-to-peak amplitude (below 0.5 mV). However, the Shannon entropy was homogenously distributed and higher compared to the values at the outside the fibrotic region.

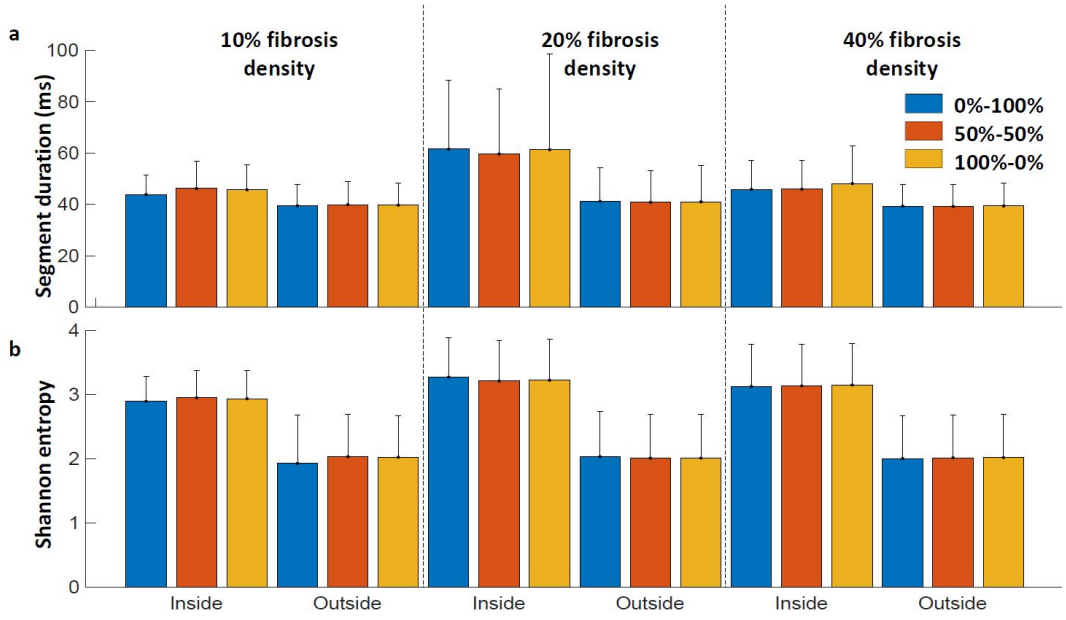

Figure 9.5: a) Mean duration of the active segment for different fibrosis densities and myofibroblasts vs. collagen ratios inside and outside the fibrotic region. As fibrosis density increases, the duration of the detected segment also increases. At 40% fibrosis density voltage becomes very small and block can occur. b) Mean Shannon Entropy at the inside and outside of the fibrotic region. Different densities of fibrosis increase the Shannon Entropy, it is not significantly affected by the ratio of myofibroblasts vs. collagen. Adapted from [112]

9.3 Discussion

Heterogeneities in the fibrotic tissue do not only alter the dynamics of the reentrant activity but can change the morphology of the EGM. McDowell et al. explored the influence of using collagen, fibroblasts, and gap junction reduction but neglected the effect of inflammation [76]; however, they did not study the effect on the EGM's morphology. An increase in the number of myofibroblasts in the cardiac tissue affects the rotation dynamics due to the ability of these cells to follow myocytes action potential [25]. Myofibroblasts introduced a delay in propagation but not a block when they are sparsely distributed (less than 40% density) [2, 15].

Ashihara et al. [104] showed that fibroblasts present in the atrial substrate could alter the morphology of the EGM. Our results also show that myofibroblasts changed the morphology of the EGM. Since myofibroblasts tend to homogenize cardiac tissue, segments with shorter activity duration were found compared to simulations where only collagen was present. However, depolarization and repolarization heterogeneity introduced by inflammation paracrine remodeling in the myocyte and myofibroblast infiltration can increase the tissue's vulnerability to arrhythmia [115].

The simulations showed that the composition of the fibrotic tissue clearly affects the dynamics of the reentry. Roney et al. [27] also showed that modeling methodologies of fibrotic tissue have a large effect on rotor dynamics in 3D simulations. However, it is still

unclear how fibrosis structure and transmurality may affect the morphology of the EGM. This will be subject of investigation in subsequent chapters of the present Thesis.

Understanding the mechanisms responsible for initiation, progression, and resolution of cardiac fibrosis is crucial and may help design anti-fibrotic treatment strategies and ablation therapies for patients with peAF.

Chapter 10

Computational modeling of intracardiac signals

Signals measured at the surface of cardiac tissue are known as electrograms. Electrograms are generated by cellular depolarization during the propagation of the electrical activation in cardiac tissue.

Electrograms recorded in electrodes close to the cardiac surface are know as unipolar electrograms. Unipolar electrograms from healthy tissue have a biphasic deflection. With a depolarization front approaching the electrode, the potential field is positive, which results in a positive deflection of the electrogram. The value of the electrogram becomes zero at the time when the wavefront is precisely underneath the electrode. Then, when the wavefront propagates away from the electrode, the electrogram becomes negative because the electrode is located in the negative part of the potential field.

Several modeling studies calculate the extracellular potential at one point in space but they neglect the effect of electrode's geometry and orientation [116, 117]. This chapter explores the effect of modeling a realistic geometry of the catheter on EGM. Part of this study has been published as a conference contribution [39] and a preprint [118].

10.1 Methods

Two different setups were created to study the influence of the electrode and catheter's geometry on computed electrograms in in silico experiments. Both setups modeled the cardiac tissue with a surrounding blood bath. In the first setup, a grid of 16 cubic electrodes of 1 mm side length, and interelectrode space of 3 mm was created. In the second setup, the realistic geometry of the two catheters was placed at the surface of the tissue. The HD Grid catheter (St. Jude Medical, EnSite HD Grid catheter, St. Paul, MN) with a constant interelectrode space of 3 mm and the Lasso catheter (Biosense Webster, Diamond Bar, CA, USA) with an interelectrode distance of 2 mm between electrodes of one pair and 6 mm

between pairs. Realistic geometries that consider electrode size, separation, and position with respect to the wavefront were taken into account.

Bidomain simulations were ran using openCARP [37, 38] to simulate the biophysical phenomena of the electrical propagation in the cardiac tissue and the catheter's influence on the electrograms at the surface of the tissue.

The blood bath around the cardiac tissue was modeled as a conductive medium with a conductivity of 0.625 S/m [119, 120]. Electrodes were modelled as a highly conductive material (1×10^{12} S/m). In the case of the catheter, insulator materials were modelled with a low conductivity 1×10^{-6} S/m.

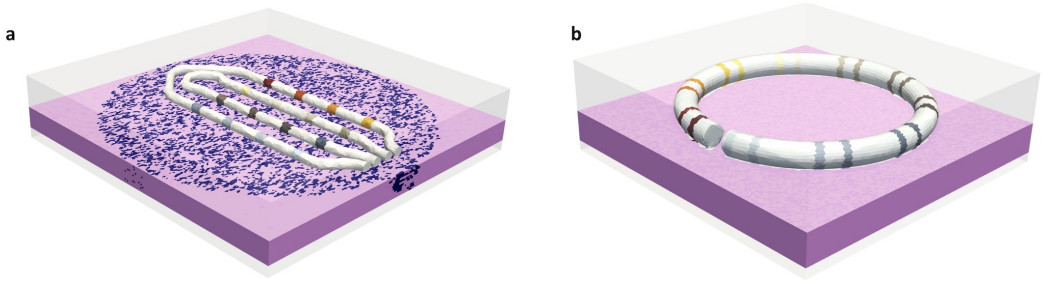

Figure 10.1: Model of the in silico setup with the commercial catheter. a) HD-grid model included on top of a fibrotic area. b) 20-pole lasso catheter over a non-fibrotic tissue.

Additionally, a realistic clinical noise model was added to the simulated electrograms to produce a more accurate unipolar electrogram. More in detail, clinical unipolar electrograms were extracted from patients' recordings. With the help of the tool ECGDeli [121], the ECG signal recorded on the surface of the thorax of the patient was used to detect the time windows of the ventricular activity, which corresponds with the duration of the QRST complex. The detected time windows were used to automatically blank the ventricular far-field artifact from unipolar electrograms. Afterwards, the non linear energy operator (NLEO) algorithm was used in the signal without the ECG complex to detect the atrial activity. Also atrial activity was blanked from unipolar electrogram. The remaining signal was then pure noise artifacts present during the electrophysiological study.

With the isolated noise artifact segments, an autoregressive model was fitted to obtain a generalized clinical noise model. The model was determined by Eq. 10.1:

$$X_t = \sum_{i=1}^{p} \phi_i X_{t-i} + \varepsilon_t^* \,, \tag{10.1}$$

where X_t is the time series and ε_t^* is white noise. The model order p was determined based on the Bayesian information criterion. The smallest Akaike information criterion value determined the global order, and the model coefficients ϕ_i were averaged to obtain a global model representing the clinical noise of intracardiac signals. The generalized model was added to the simulated unipolar signals as depicted in Figure 10.2. After adding

noise, unipolar synthetic signals were filtered using a band-pass filter between 0.05 Hz and 900 Hz. Additionally, bipolar electrograms were calculated by subtracting the signals from the corresponding pairs of electrodes and filtered by a band-pass filter between 30 Hz and 300 Hz used in clinical settings.

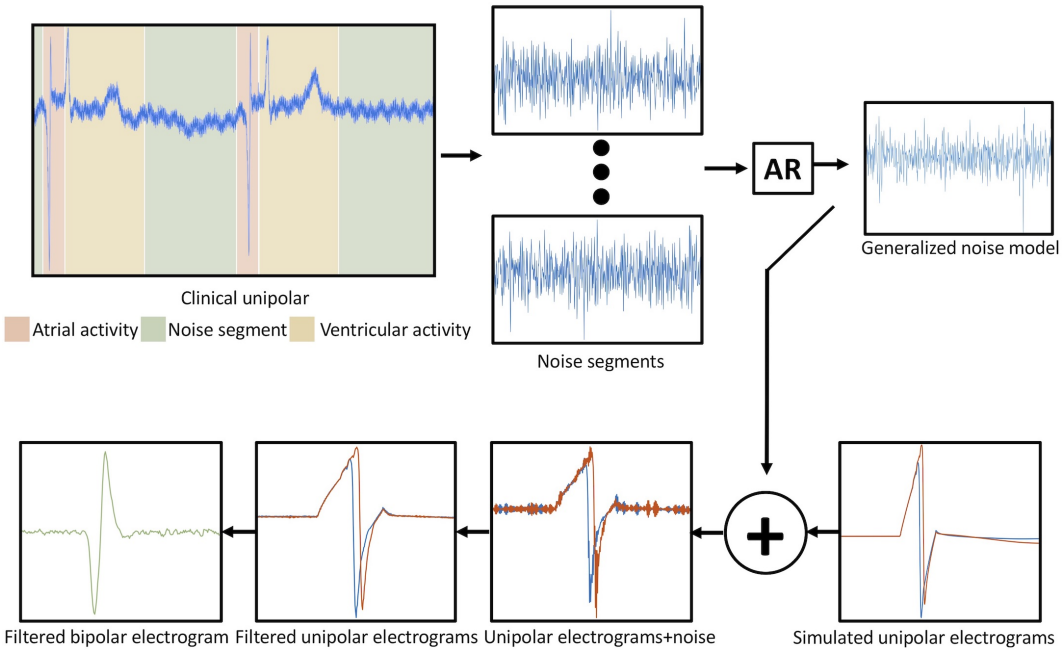

Figure 10.2: Workflow to generate the noise model and the addition to the simulated signals. In the top left corner, the different segments of the activity from a clinical unipolar electrogram are depicted. Autoregression was applied on the noise segments. The noise model was used to estimate the simulated unipolar electrogram with noise. Afterwards, the unipolar electrograms (red and blue trace) were filtered, and the bipolar electrogram was calculated by subtracting the unipolar electrograms. Adapted from [118].

10.2 Results

The use of realistic geometries to represent the electrodes alters the morphology of simulated electrograms. Figure 10.3a shows a simulated bipolar electrogram sensed with cubic electrodes where the impact of filtering on the positive slope becomes visible. Figure 10.3b shows a simulation with a cylindrical electrode geometry mimicking the commercial catheters used in this study. The resulting electrogram is not symmetric and filtering has no significant effect on the positive slope, which is steeper than in the electrogram sensed with cubic electrodes. Adding noise to the simulated signals decreases their amplitude and fractionates the morphology (Figure 10.3c). Simulated bipolar electrograms without noise have a higher amplitude of R and S peaks, which decrease with the addition of noise. Figure 10.3d compares a simulated

signal with a clinical signal. In simulated electrograms negative and positive slopes are close to the values of the clinical signal, 0.1 mV/ms and 0.25 mV/ms, respectively.

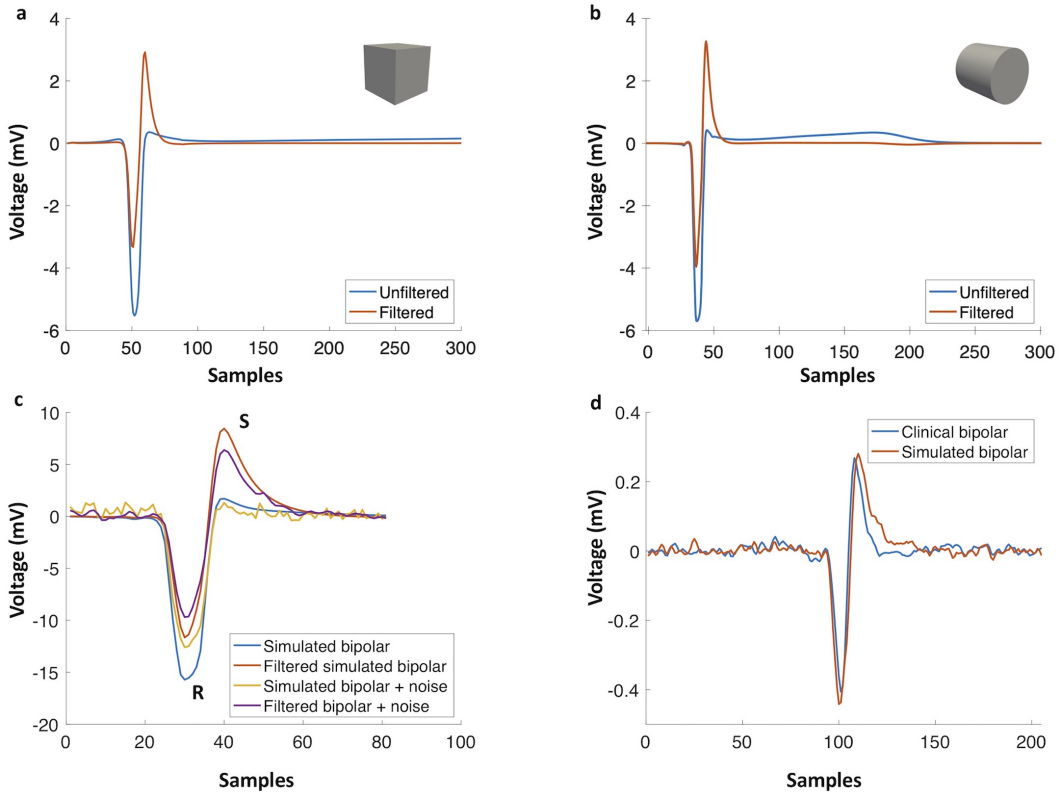

Figure 10.3: Importance of using a realistic electrode geometry and adding noise for simulated intracardiac signals. a) Bipolar electrogram signal recorded with a cubic electrode (blue trace) and the corresponding filtered signal (red trace). b) Signal recorded with a cylindrical electrode (blue trace) and the resulting signal after filtering (red trace). c) Simulated signals recorded with a cylindrical electrode with and without noise and the resulting signals after filtering. d) Comparison of a simulated signal with a clinical signal.

In silico electrograms were validated against clinical electrograms recorded from areas of the atria with peak-to-peak amplitudes higher than 0.5 mV. Cross-correlation was used to align clinical signals and simulated electrograms in time for maximal similarity. Simulated bipolar signals for non-fibrotic tissue had a correlation of 91.13±0.05 % with clinical signals. Clinical high voltage (peak-to-peak >0.5 mV) and simulated control electrograms (no fibrosis) had a peak-to-peak voltage of 1.67±0.05 mV and 2.25±0.01 mV, respectively. Clinical and simulated control electrograms had a duration of 18.30±0.56 ms and 17.5±0.04 ms, respectively.

10.3 Discussion

The bidomain model captures the biophysical phenomena of cardiac depolarization and the generated electric field in the extracellular medium with wavefront propagation. The biophysical model also simulates the equipotential characteristic of a metal electrode and the influence of the geometry in the simulated electrogram.

Nairn et al. [39] have shown the importance of the electrode size in the amplitude of the electrogram. Furthermore, the results presented in this chapter showed the importance of introducing a realistic geometry of the catheter to compute the electrogram morphology. Additionally, simulated bipolar electrograms from this study have shown a high correlation with clinical bipolar clinical signals [43].

A high correlation between clinical and in silico electrograms is of great importance to study the electrical activation of the cardiac tissue. Electrograms from in silico experiments provide the information of the cardiac cells' action potential (sources) that will generate the extracellular potential measured by the electrode. Therefore, there is a great necessity to use realistic geometries to understand the mechanisms that affect the electrograms and translate the gained knowledge to clinical applications that improve the patients' quality of life.

Chapter 11

Fibrosis characterization using machine learning

With the increasing amount of clinical data available, the use of machine learning for the interpretation of cardiac signals is steadily increasing. Machine learning has been extensively used in electrocardiogram analysis due to its potential to analyze big datasets and uncover mechanistic information about cardiac electrical function [122–124]. Several studies aimed at quantifying AF mechanisms and automatically localize reentrant drivers using in silico or clinical electrograms [125, 126]. Less attention has been paid to how intracardiac electrograms can provide information about the cardiac substrate based on fibrosis effects on the signal morphology. Campos et al. classified different types of fibrosis based on electrogram features using in silico experiments [20]. However, quantification of fibrotic volume fraction and transmurality in the atrial substrate has not been reported yet to the best of our knowledge. Additionally, data-driven approaches can help to overcome the use of a single voltage cut-off value to characterize the cardiac substrate and distinguish between non-fibrotic and fibrotic tissue based on a more comprehensive holistic set of criteria. Part of this work was presented as a part of a prepint [118].

11.1 Methods

11.1.1 Modeling realistic setups

Computational cardiac modeling can considerably accelerate the process of designing and evaluating medical devices, including mapping systems and software to treat patients with cardiac arrhythmia. The American Society of Mechanical Engineers (ASME) Verification and Validation Subcommittee standard V&V40 (Verification and Validation in Computational Modeling of Medical Devices) outlines credibility requirements of a computational model based on risk.

Following the recommendations of the ASME V&V40 the modeling steps (Figure 11.1) for the present study were carefully chosen.

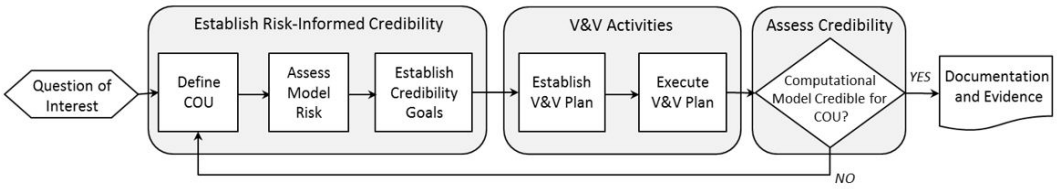

Figure 11.1: ASME V&V40 workflow to verify and validate models that will be translated to clinical applications. Adapted from [127]

As an input of the flowchart in Figure 11.1, two questions of interest were defined:

1. "Can tissue fibrotic characteristics be derived from intracardiac signals to guide ablation therapies?"
2. "Can synthetic data be used to train a classifier to locate fibrotic tissue and quantify its characteristics?"

These guiding questions helped define the required model level of detail for the in silico experiment. In the next step, we established the risk-informed credibility of using a detailed biophysical model to simulate electrograms and use them to generate a hybrid dataset which combines clinical and synthetic signals. Risk-informed assessment defined the level of uncertainty and the model's complexity based on the context of use (CoU) of the in silico experiments. The CoU of the model is to *generate a hybrid dataset to train a classifier to locate and quantify fibrotic tissue*.

The strategy used to model fibrosis affects the dynamics of electrical propagation as described by Roney et al. [63], which in turn affects electrogram morphology. Fibrosis modeling uncertainty was reduced by considering several realizations of random uniformly distributed collagen fibers with different volume fraction and transmurality. We overcame the limitation of catheter geometry and wavefront direction by including two models of commercially available catheters (HD-grid catheter and 20-pole lasso catheter) and pacing from three different locations [128]. Two different human atrial cardiomyocyte models were considered to minimize the uncertainty of the action potential morphology influence on the electrogram. Moreover, an autoregression model of clinically measured noise artifacts was created. The modeled clinical noise in combination with the simulated electrograms reduced the uncertainty of simulated with respect to measured electrograms. Considering all points mentioned above, the risk-informed assessment of using in silico experiments to characterize the fibrotic substrate was defined as medium.

Afterwards, Table 11.1 establishes the credibility level based on the model risk [129]. Verification steps of the software's quality code is ensured using an automatic regression testing framework [37], and numerical solutions were established following the steps of Niederer et al. [130]. In silico electrograms where compared with different clinical mea-

surements from different healthy areas of the atria to evaluate the degree of credibility of bidomain simulations (Figure 10.3d).

Table 11.1: Summary of the credibility factors. Assesment was based on the ASME V&V40 standard [129].

Activity	Credibility factor	Rigor	Credibility level
Verification			
Code	Software quality assurance	D	High
	Numerical code verification	D	High
Calculation	Discretization error	D	High
	Numerical solver error	D	High
	User error	N/A	N/A
Validation			
Computer model	Model forms	C	High
	Model input	N/A	N/A
Comparator	Test samples	C	Medium
	Test conditions	B	Low-Medium
Assesment	Equivalency of input parameters	N/A	N/A
	Output Comparison	4	Medium/High
Applicability	Relevance of the quantities of interest	N/A	N/A
	Relevance of the validation activities to the CoU	C	Medium/High

11.1.2 In vivo and in silico electrograms

The dataset was composed of two data sources. The first source was clinical data from in vivo recordings from patients who were diagnosed with persistent AF. From the clinical data source, a cut-off value of 0.5 mV was used to distinguish electrograms from healthy and pathological tissue. Electrograms from healthy tissue were validated by expert cardiologists in the field of electrophysiology.

The second source of data were in silico electrograms from fibrotic tissue. In silico experiments were set up to collect the electrograms at the surface of the fibrotic tissue. The tissue was stimulated from three different locations. The left and bottom border were stimulated to simulate a planar wave across the fibrotic tissue. Additionally, the tissue's left top corner was stimulated to simulate a non-planar wave across the fibrotic area. Simulated signals were added with the realistic clinical noise model explained in chapter 10, which reproduced the noise present in the clinical unipolar electrograms.

Both in silico electrograms and clinical electrograms followed the standard clinical practice filter configuration. Unipolar electrograms were filtered using a band-pass filter from 0.05 Hz to 900 Hz. Then bipolar electrograms were calculated and a band-pass filter from 30 Hz to 300 Hz was used.

In this study a method based on the Hilbert transform is proposed to detect the atrial activity segments from the electrograms. The electrogram signal was transformed in the Hilbert space as depicted in Figure 11.2a. From the centroid (orange trace) a vector was used

to measure the distance to the signal and to trace loops in the signal. Frequency distributions of loop distances were used to distinguish atrial activity and noise artifacts (Figure 11.2b). As a result, atrial activity packages were detected as depicted in Figure 11.2c.

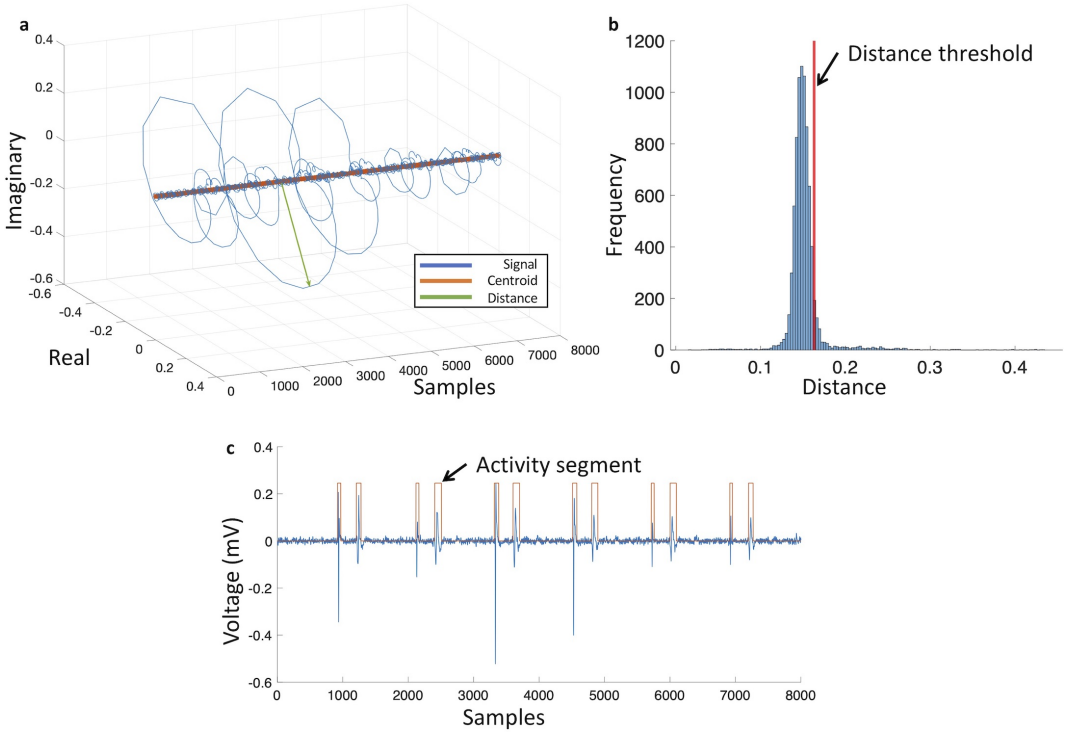

Figure 11.2: Electrogram activity detection in the Hilbert space. a) Electrogram signal (c) in the Hilbert Space with centroid (orange trace), green arrow depicts the distance measured from the centroid to the signal. b) Frequency distribution of centroid to signal distance, red line represents mean value plus one standard deviation. c) Bipolar electrogram (blue trace) and activity segments (orange trace). Adapted from [118].

11.1.3 Machine learning

Nowadays, there is a wide variety of machine learning algorithms. Two main branches of machine learning algorithms can be clearly identified: supervised algorithms and unsupervised algorithms. Supervised algorithms are best suited to problems where there is a set of available ground truth data to train the algorithm. Unsupervised algorithms automatically find structure in the data without labels by extracting characteristic features and similar clustering data. The lack of a ground truth makes hard measuring the accuracy of an unsupervised algorithm.

In this thesis, supervised algorithms are used to characterize the atrial fibrotic substrate from electrogram features due to ground truth data availability, thanks to the highly detailed

in silico experiments. In the hybrid dataset, every single bipolar electrogram was labeled as non-fibrotic, 10% fibrotic density, 20% fibrotic density, 40% fibrotic density, 60% fibrotic density, subendocardial (0.5 mm), partial transmural (1 mm) or total transmural (2 mm). The features extracted from bipolar electrograms quantify their complexity. For each bipolar electrograms, segments of atrial activity were calculated by tracking closed loops in Hilbert space. The distribution of the radius of every single loop was calculated and the mean value plus one standard deviation was chosen to distinguish between cardiac activity and noise. The peak-to-peak amplitude was calculated for each active segment. Furthermore, different entropy measures (sample entropy [131], Shannon entropy [114], spectral entropy [132], and Kolmogorov complexity [133]) were calculated for each segment of atrial activity. Additionally, the fractal dimension coefficient was calculated for the whole 2.5 s signal segment [134].

Four different supervised machine learning algorithms (support-vector machine, decision tree, random forest, and K-Nearest neighbor) were benchmarked to define which algorithm was most adequate to identify the characteristics of the fibrotic tissue from extracted features of the electrograms. Hyperparameter for each algorithm were tuned to find the best set of parameters that best fitted the problem.

Afterwards, both clinical and simulated electrograms were synergically combined to create a hybrid dataset containing in vivo and in silico electrograms. The hybrid data set was split into training, validation, and test sets as a 70%/15%/15% random split. All classes were guaranteed to be in all subsets. The validation set was used by the Greedy technique to tune the classifier optimally. Furthermore, validation set accuracy was used to check that the algorithm was not overfitting when comparing against the test set accuracy. One hundred different realizations were run using hold-out cross-validation to obtain the mean accuracy of the classification algorithm.

11.2 Results

The benchmark for the machine learning algorithms is depicted in Figure 11.3. One hundred different realizations were done in order to obtain the mean value and the standard deviation for each algorithm. For this specific case the used decision tree had a mean accuracy of 97.3%$\pm$0.6. Random forest, support vector machine and K-Nearest neighbor had and mean accuracy of 92.2%$\pm$0.9, 96.2%$\pm$0.6, and 93.8%$\pm$1.5, respectively.

Extracted features from bipolar electrograms are depicted in Figure 11.4. The main diagonal shows the distribution of the calculated features for the different groups of signals (different fibrotic densities in Figure 11.4a, different degrees of fibrosis transmurality in Figure 11.4b). Peak-to-peak amplitude is not a good feature to determine the degree of fibrosis due to the wide range of amplitudes that overlap for fibrotic vs. non-fibrotic cases. While sample entropy can distinguish between fibrotic and non-fibrotic tissue, the distribution of the values overlaps for different densities. The distinction between different fibrosis

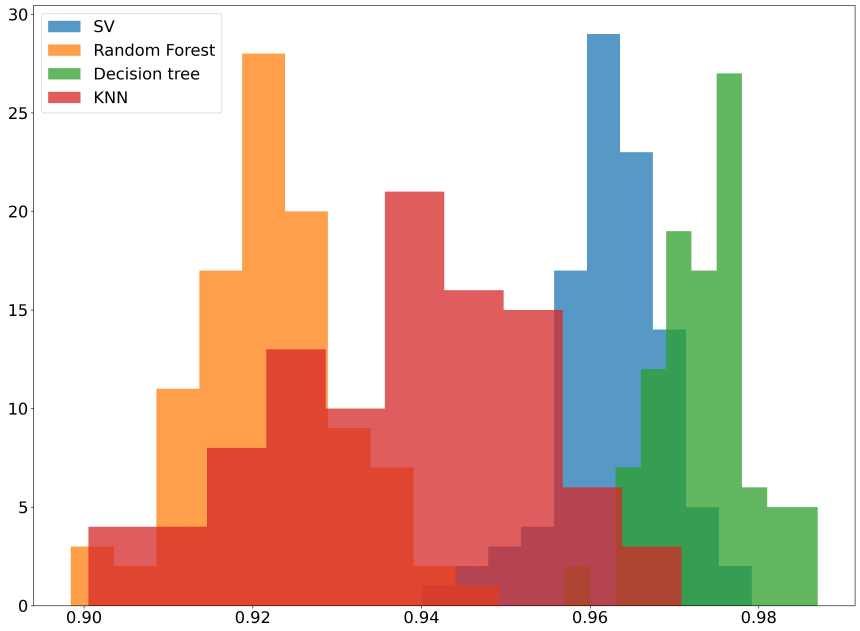

Figure 11.3: Machine learning benchmark of four different algorithm to characterize the cardiac fibrotic substrate. One hundred random realization were done to measure the accuracy of the classifier for the specific task. Decision tree, random forest, support vector machine (SV) and K-Nearest neighbor (kNN) had and mean accuracy of 97.3%±0.6, 92.2%±0.9, 96.2%±0.6, and 93.8%±1.5, respectively.

transmuralities is not possible using only one feature since the value for all features overlap for all density or transmurality values (Figure 11.4b, main diagonal).

A decision tree classification algorithm was trained to separate different fibrosis densities and degrees of transmurality. The combination of signal complexity features was determined by a Greedy forward algorithm. The dataset was randomly divided into 70% train, 15% test, and 15% validation. The mean accuracy of the three classifiers was calculated by doing 100 different realizations. Figure 11.5a shows the confusion matrix of the classifier for distinguishing between non-fibrotic and fibrotic tissue. The mean accuracy for this classifier was 97.95±0.03% with 98.81±0.01% sensitivity and 97.16±0.01% specificity. The classifier slightly overestimated the fibrotic areas. Figure 11.5b shows the classifier performance to identify fibrosis density (non-fibrotic, 10%, 20%, 40%, and 60%) with a mean accuracy of 97.01±0.02% and 96.33±0.03% and 99.05±0.01%, for sensitivity and mean specificity, respectively. The most relevant features for classification of fibrosis density, determined by the Greedy forward algorithm, were sample entropy and spectral entropy.

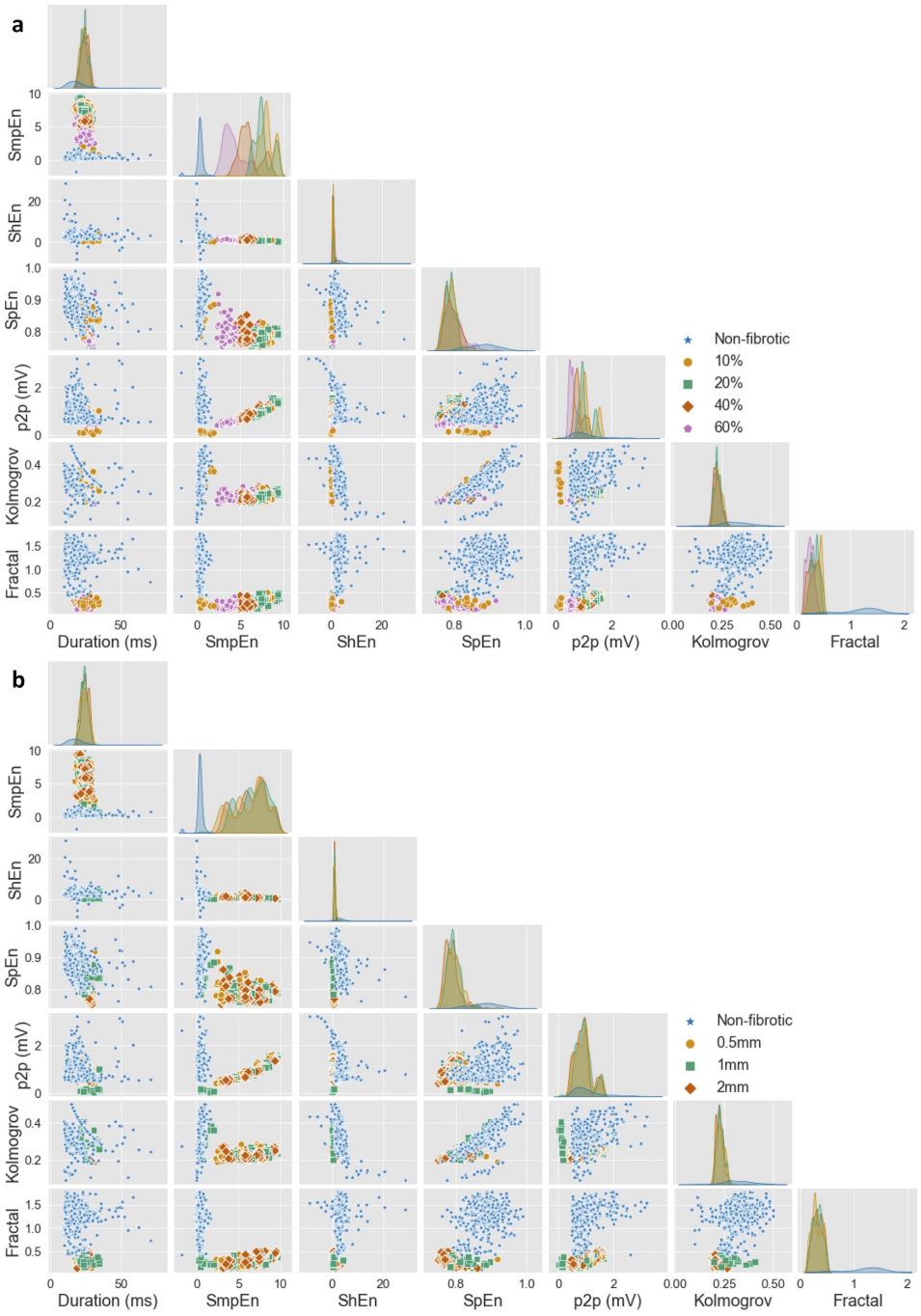

Figure 11.4: Feature distribution for all in vivo and in silico electrograms (including noise). Single feature distribution can be observed in the diagonal and the combination of two features is reflected in the scatter plots. a) Features split by different densities of fibrosis. b) Features split by different transmurality degrees. Abbreviation: Duration: Duration of the active segment (ms), SmpEn: sample entropy, ShEn: Shannon entropy, SpEn: spectral entropy, p2p: peak-to-peak amplitude (mV), Kolmogorov: Kolmogorov complexity, Fractal: Fractal dimension. Adapted from [118].

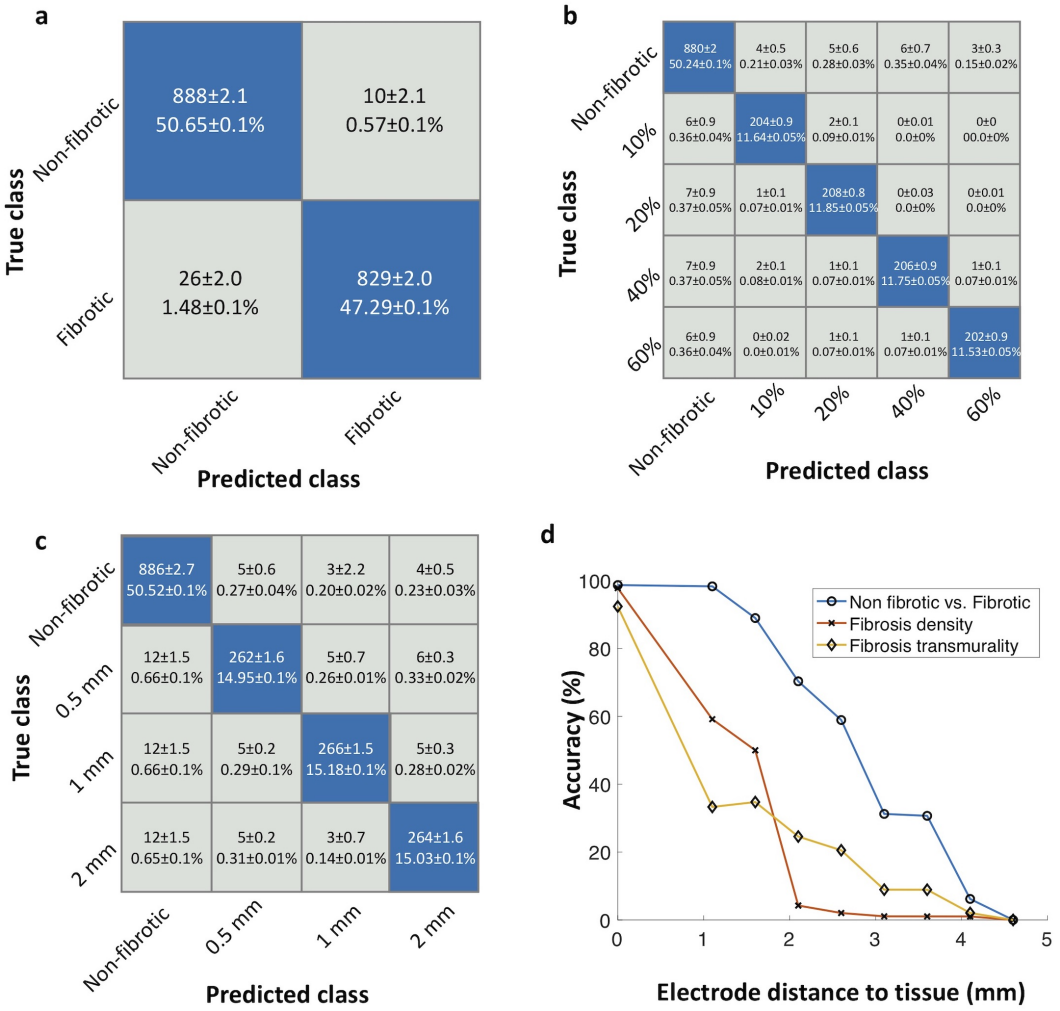

Figure 11.5: a) Confusion matrix of the decision tree classifier for identifying non-fibrotic vs. fibrotic substrate. b) Confusion matrix of the decision tree classifier showing the performance for identifying different fibrosis densities. c) Confusion matrix of the decision tree classifier showing the performance for identifying transmurality of fibrosis. d) Effect of increasing the electrode surface to tissue surface distance on the accuracy of the classifiers to distinguish fibrotic tissue, density and transmurality. Adapted from [118].

To identify transmurality of fibrosis in the tissue, the classifier yielded a mean accuracy of 94.62±0.01%, 92.99±0.02% sensitivity, and 97.86±0.01% specificity. For fibrosis transmurality, misclassification occurred for some cases. Nevertheless, it is able to distinguish all four classes (non-fibrotic, 0.5 mm, 1 mm and 2 mm). The most relevant features for classification of transmurality were sample entropy and peak-to-peak amplitude.

Furthermore, the effect of increasing the distance between the catheter and atrial endocardial surface on the classifiers' accuracy was investigated. The classifier's accuracy dropped with increasing distance, as shown in Figure 11.5. The accuracy of the classifier dropped to 0% for electrode-to-tissue distances bigger than 4.1 mm, to distinguish non-fibrotic from

fibrotic tissue. To identify different densities, the accuracy dropped to 59.17% at 1.1 mm distance of the tissue. Additionally, transmural accuracy dropped to 33.30% with a distance of the tissue of 1.1 mm (Figure 11.5d).

11.3 Discussion

With the increasing number of data available, data-driven approaches help improve patient's diagnosis and therapies. Several studies used data-driven approaches with clinical data to characterize electrocardiogram signals measured on the body surface [135–138]. Costabal et al. used a hybrid dataset approach to interpret activation times during AF[139]. In this Thesis a detailed in silico setup was developed as a perfectly controlled testing environment to understand intracardiac signals recorded with two different commercial catheters. Furthermore, a decision tree classifier using clinical and simulated data to characterize signals based on complexity measurements was trained. Decision trees offer a comprehensible structure to follow the decisions taken for the classification. All three classifiers had a high accuracy. Despite overlapping features for different degrees of transmurality (Figure 11.4b), the combined features used to train all decision tree classifiers distinguished non-fibrotic tissue, fibrosis volume fraction and all three different transmuralities of fibrosis from electrogram signals. Our results suggest that combining clinical and simulated data helps to characterize electrical tissue properties more accurately than using synthetic data alone. In future work, the classifier could be extended to include more training signals recorded directly at the surface of the tissue and at certain distances above the tissue to increase the perfomance when there is non direct contact of the catheter with the tissue surface.

Different ablation strategies target fibrotic areas by ablating or isolating them [12]. Both techniques rely on a voltage cut-off value for the identification of possible fibrotic areas. While ablating fibrotic areas tries to homogenize the fibrotic substrate, isolation encloses the fibrotic regions and connects them to the pulmonary vein isolation lines to prevent a potential proarrhythmic effect. This suggests that identifying fibrotic tissue through electroanatomic mapping is essential and the choice of a single voltage cut-off value may not be sufficient to decrease the recurrence of arrhythmia [17]. Gutbrod et al. showed the importance of fibrosis transmurality for electric propagation during AF [140]. Using a hybrid dataset approach, our findings can help standardize the identification of non-fibrotic vs. fibrotic areas and provide valuable information on the fibrotic tissue characteristics such as fibrosis density and transmurality. Several studies have shown that low-density fibrosis can modify the propagation and initiate or maintain arrhythmia [43, 141]. The border zone of high-density fibrotic areas are prone to be a point of anchor for rotational activity [108, 142–144] while low-density fibrosis micro-structure can alter the propagation pattern and maintain reentry [145, 146]. The trained classifier was used on five patients from the test set of our patient cohort to distinguish and characterize fibrotic tissue. For clinical data, not all low voltage areas were marked as fibrosis when using a single cut-off value. Areas with low-density (10%) subendocardial fibrosis (0.5 mm) were annotated as high voltage area when

using a single peak-to-peak cut-off value of 0.5 mV. Therefore, the use of hybrid datasets and data-driven approaches could help estimate fibrotic tissue characteristics to support planning of ablation therapy.

The results show that current clinical standards for substrate mapping using bipolar voltage alone are not sufficient to characterize the atrial fibrillation substrate comprehensively. Machine learning algorithms trained using hybrid datasets and multiple features obtained from intracardiac signals may overcome these limitations providing fibrosis density and transmurality maps. This may lead to optimized therapeutic approaches.

The model approach does not capture the influence of atrial anatomy, nevertheless our hybrid dataset approach tries to minimize this effect by including clinical signals. Furthermore, increasing the catheter to tissue distance decreases the accuracy of the classifier. The effect of the distance can likely be minimized if the dataset is extended by including signals that were acquired at a certain distance of the cardiac tissue. Additionally, only a homogeneous distribution of fibers from the endocardium to the epicardium was considered, which may not represent heterogenous tissue architecture observed in some regions of the atria. In this study the effect of inflammation-induced paracrine remodeling or myofibroblast interaction [36] was not included. While our approach shows promising results and highlights the essential features of intracardiac signals to characterize atrial substrate, validation through independent experimental and clinical data is desirable.

The modeling approach successfully answered the question of interest: A classifier can be trained using clinical and simulated data to characterize the cardiac substrate to support ablation therapy by providing fibrosis density and transmurality maps. Moreover, the credibility assessment showed that detailed cardiac modeling can be a valuable framework. In the future, classifiers to predict cardiac tissue characteristics could be integrated in clinical electroanatomic mapping systems. Finally, our study emphasizes the potential of in silico experimentation and data-driven approaches to characterize the patient's substrate and demonstrates the potential of software tools to support medical decisions during the procedure.

Chapter 12

Determination of wavefront direction using transfer entropy

Determining the direction of the wavefront is essential to understand the behavior of atrial electrical activity. Van Nieuwenhuyse et al. [147] have recently shown the advantage of using directed graphs to understand the wavefront direction; however, the method relies on the annotation of electrograms, which is not a trivial task under AF due to the complexity of the signal. In neuroscience and more specifically in the study of the electroencephalogram, statistical approaches have emerged as a powerful tool to understand the electrical activity of the brain [148]. Statistical methods have the advantage of not relying on the electrical signal's annotation of biomarkers. This chapter explores the use of information theory measurements to understand the electrical propagation in cardiac tissue. Part of this work was presented as a conference contribution.

12.1 Methods

12.1.1 Transfer entropy

In non linear systems, statistical relationships between the process variables reveal information about the biophysical dynamics. Therefore, identification of the relevant variables and characterization of their interactions are crucial for a better understanding of the underlying mechanism in a complex system.

Different studies use mutual information, which provides a model-free approach to quantify the information overlap between two variables. However, mutual information only captures the information shared by two variables but not the flow of information between two variables. Therefore, Scheriber et al. [149] proposed transfer entropy (TE) as an information measurement.

TE is defined by Eq. 12.1, which measures the amount of uncertainty that is reduced in future values of one variable (Y) by knowing past values of another variable (X), given the past values of the first variable (Y).

$$TE(X \rightarrow Y) = \sum_{y_{t+1}, y_t^n, x_t^m} p(y_{t+1}, y_t^n, x_t^m) log \frac{p(y_{t+1}|y_t^n, x_t^m)}{p(y_{t+1}|y_t^n)} \tag{12.1}$$

where X and Y are the variables to be considered for calculating the flow of information,

12.1.2 Directed graphs

In mathematics, and more specifically in graph theory, a graph is made up of a set of vertices connected by edges (Figure 12.1a). A directed graph is when the edges have a direction associated with them.

In a directed graph (DG) (Figure 12.1b), an arrow is considered to indicate the direction from node (vertex) v1 to node (vertex) v2; where v2 is the head and v1 is the tail of the arrow. The relation of the nodes is described in the adjacency matrix. The adjacency matrix of a directed graph is unique up to identical permutation of rows and columns.

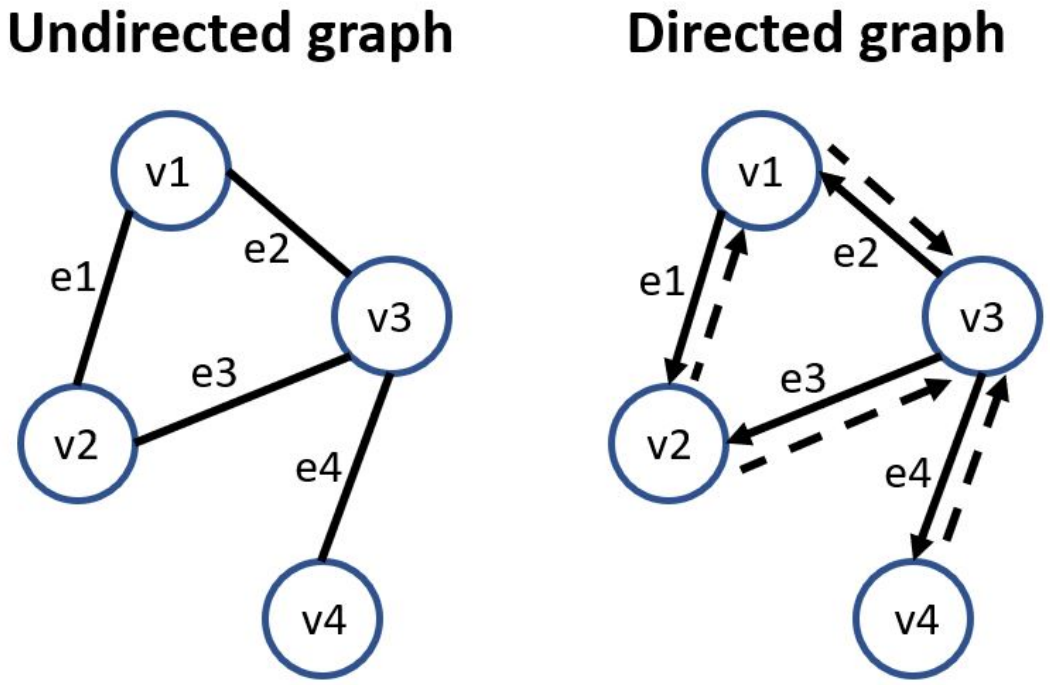

Figure 12.1: a) Undirected graph, where vertices or nodes are connected with bidirectional edges. b) Directed graph,where vertices or nodes are connected with directed edges represented by arrows. Arrow's tail points the source and the arrow's head points to the sink.

A directed graph was created using the physical electrode position and its relation with its neighbors. Electrodes will correspond to nodes of the graphs and edges are all possible connections with all its neighbors. TE values are used to add directionality to each edge of the graph. Higher TE values will indicate a higher flow of information. Therefore, for each direct neighboring node the maximum TE value was used to define the direction of the edge.

12.2 Results

Simulated electrograms had a total duration of 8 s. The length of the signal was reduced to 2.5 s which is the duration of the clinical recordings. The reduction of the signal's length had little effect on the value of TE. Signals with 8 s had a TE value of 0.4 and signals of 2.5 s had a value of 0.38.

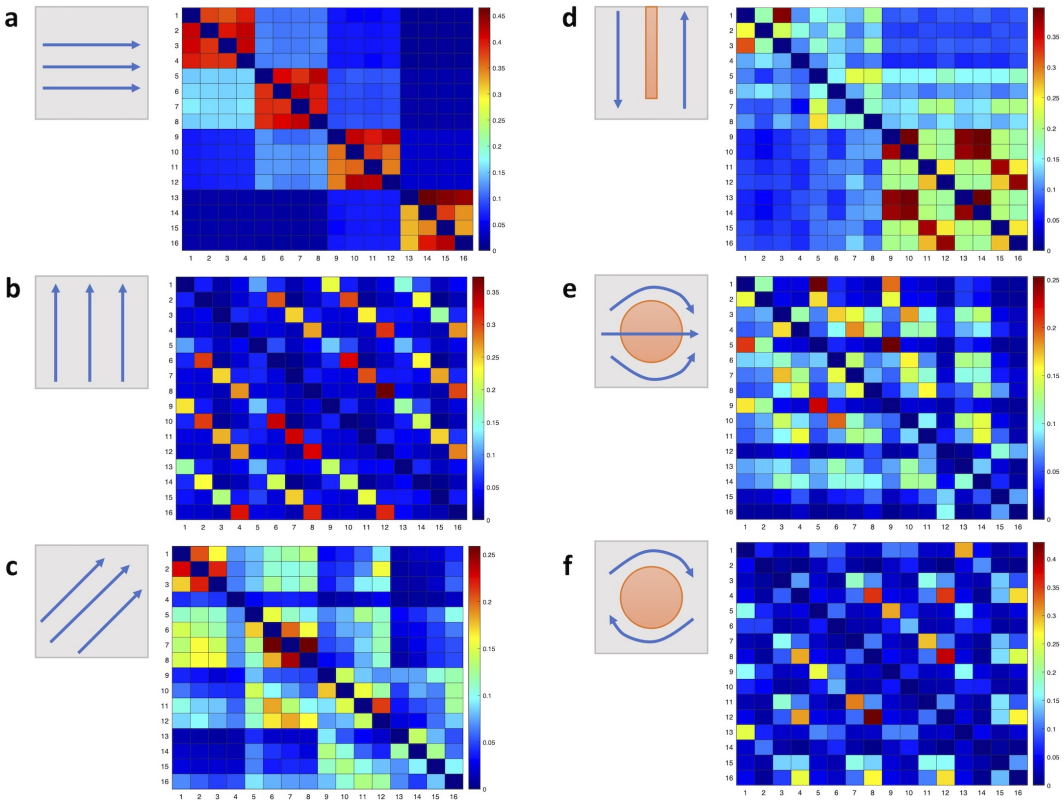

Figure 12.2: Different TE matrices patterns of calculated TE. a) TE pattern for a planar wave following the fiber direction while b) shows a planar wave transversal to the fiber direction and c) a radial planar wave. When conduction block modifies the propagation direction. d) shows a u-turn of the wave propagation due to a line of block. e) shows a fibrotic area where the propagation can travel across, and d) shows a reentry activity around a fibrotic area where the pattern is sparse but organized.

Transfer entropy was calculated for each electrode with all the others. Values of transfer entropy were then shown as a matrix where the diagonal is the TE value with its self (Figure 12.2). Different wave front propagation arises different matrices patterns. Planar waves patterns are organized blocked pattern matrix with a maximum transfer entropy value of 0.45 (Figure 12.2a). When a reentry is generated, the matrix pattern is now disorganized with a maximum transfer entropy value of 0.4 (Figure 12.2f).

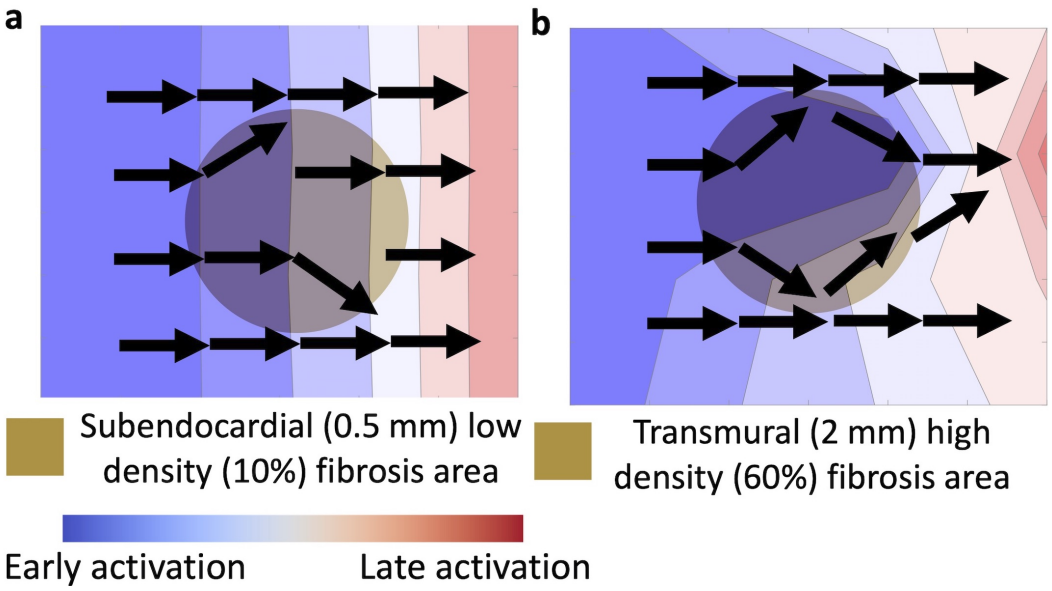

Figure 12.3: Directed graph calculated using a directed graph from an HD-grid. a) Subendocardial low-density fibrosis alters the wave propagation locally. DG-TE can locate the local block while activation times fail to distinguish local blocks. b) DG-TE map shows a block due to a transmural high-density fibrotic area and shows the wave front's local direction. In contrast, local activation times show a delay on the activation but not a conduction block.

Directed graphs help to visualize local and global directionality of the depolarization wave in the cardiac tissue. In the case of a planar depolarization wavefront, TE in a combination of DG shows the propagation direction. When reentry was induced, DG shows the direction of the rotational activity, and the disconnection of nodes identifies the conduction block where the reentry was anchored. Moreover, under the presence of low fibrosis density (10%) in the cardiac tissue (Figure 12.3a), DG shows the global direction of the wavefront and reveals local alteration in the directionality of the wave front propagation due to the presence of collagen. Increasing the amount of fibrosis (40% - 60%) in the tissue alters the global and local propagation (Figure 12.3b), indicating a high level of accuracy in the presence of collagen deposits in the tissue.

12.3 Discussion

Transfer entropy has shown to be a robust measurement to characterize the flow of information between two neighboring signals and to characterize the direction of the wave front propagation. Directed graphs help to preserve the spatial relation of each node, while providing the electrophysiology information between them. This information is of great importance during a clinical electrophysiology study to understand the wavefront propagation and the dynamics of an arrhythmia. The results presented in this chapter are in agreement with the finding from Rodrigo et al. [150] that showed that causality relations between electrograms could help guiding ablation therapies.

Van Nieuwenhuyse et al. [147] have shown the advantage of using directed graphs to determine reentry circuits during atrial flutter. However, the algorithm provides global direction of the wave front and macroreentry paths. The combined DG-TE has the advantage of showing local and global direction of the wave front which provides a more detailed information of possible micro structural block due to low density fibrosis (10%) and bigger structural blocks which occur with higher densities of fibrosis (40% and 60%). DG-TE helps to understand the mechanism of conduction block and provide useful spatial information

PART IV

CLINICAL APPLICATIONS

Chapter 13

Clinical fibrosis maps

Beyond pulmonary vein isolation, targeting the substrate has been proposed as another ablation strategy with promising results. However, the determination of low-voltage areas that define fibrotic substrate is based on a cut-off voltage value of 0.5 mV. The amplitude of electrograms is strongly affected by the angle of incidence of the wavefront, the electrode size, the thickness of cardiac tissue, and the distance of the recording electrodes to the cardiac tissue. In this chapter, the trained machine learning classifier was used in patient recordings as a proof of concept to overcome the use of a single cut-off voltage value to determine the fibrotic susbtrate and its composition. Part of this work was presented as a part of a prepint [118].

13.1 Methods

This study includes five patients recruited at Städtisches Klinikum Karlsruhe with the diagnosis of persistent AF. The five patients recordings were used as a proof of concept to test our approach to characterize the atrial tissue from clinical electrograms. Electroanatomical maps were acquired during sinus rhythm using the CARTO3 mapping system (Biosense Webster, Diamond Bar, CA, USA) with the Lasso catheter (Biosense Webster) or with the Rhytmia mapping system (Boston Scientific, Cambridge, MA, USA) with the Orion mini-basket catheter (Boston Scientific, Cambridge, MA, USA).

Fibrosis maps were created from a high density of electrogram recordings. However, missing data were interpolated using a radial basis function kernel (RBF). The RBF function computes the similarity for two points x_1 and x_2 (Eq. 13.1).

$$K(x_1, x_2) = exp(-\frac{||x_1 - x_2||^2}{2\sigma^2}) \tag{13.1}$$

where $||x_1 - x_2||^2$ is the Euclidean distance and σ^2 is the variance of the distribution.

13.2 Results

We applied the trained classifier to intracardiac signals measured in five patients of the test set of our cohort, which were not used to train the classifier, to create maps of atrial substrate characteristics. Figure 13.1 presents representative results for patient 1. The yellow dot (Figure 13.1a, posterior view) shows a signal annotated as high voltage and identified as non-fibrotic tissue by the classifier.

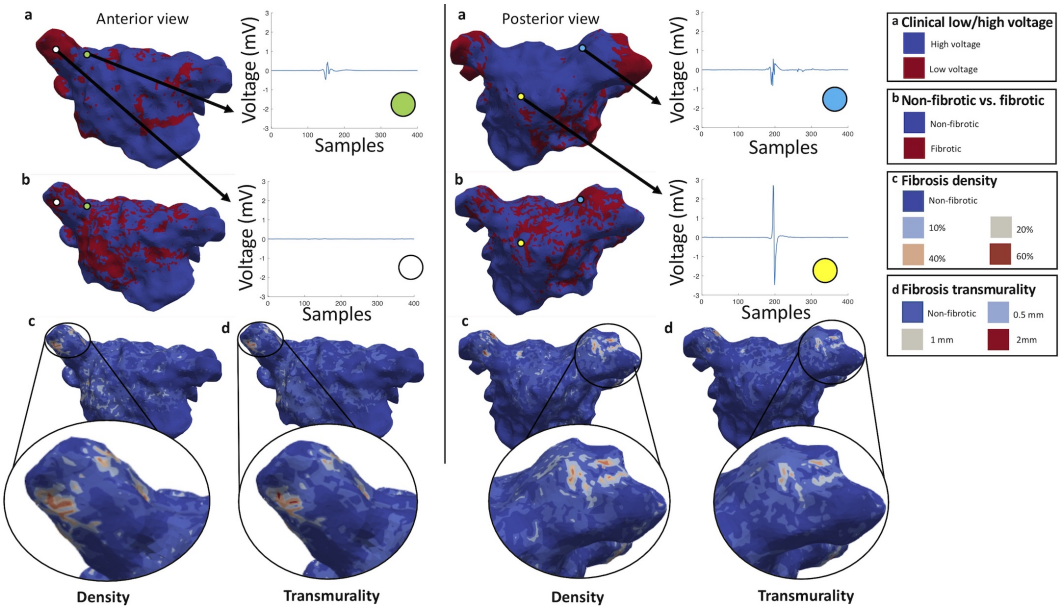

Figure 13.1: Anterior and posterior view of patient 1 maps for clinical low/high voltage (a) and classification results for non-fibrotic vs. fibrotic (b), fibrosis density (c), and fibrosis transmurality (d). The green dot represents a signal at the base of the pulmonary vein which was marked as high voltage and classified as subendocardial (0.5 mm) low density (10%) fibrotic tissue. The white dot refers to a signal recorded in the pulmonary vein classified as low voltage and high density (60%), transmural (2 mm) fibrotic tissue. The yellow dot represents a high voltage area identified as non-fibrotic and the light blue dot indicates a signal collected in the pulmonary vein annotated as high voltage and classified as low density (20%), partially transmural (1 mm) fibrotic tissue. Modified from [118].

Low voltage and high voltage areas determined by the clinical system using a cut-off value of 0.5 mV are shown in Figure 13.1a. The low voltage areas showed a mean dice similarity coefficient of 69.84±0.03% with the predicted fibrotic areas for the five patients. Patients 1, 3, and 4 showed fibrotic areas mostly within the low voltage areas. Figure 13.1b shows the classified fibrotic areas based on the signal features by the machine learning approach, where electrogram signals were fractionated and exhibited a longer activity duration independent from their peak-to-peak amplitude (Figure 13.1a, anterior view, green and white dot). Regions annotated as high voltage areas partly exhibited fractionated electrograms with a peak-to-peak voltage (1.4 mV) above the cut-off value of

0.5 mV (Figure 13.1a, posterior view, light blue dot) where these areas were classified as low density (20%) and partially transmural (1 mm) fibrosis. Fibrotic volume fraction was estimated using patient electrograms as input for the classifier (Figure 13.1c). In general for this patient cohort, high density was located at the core of fibrotic areas. Furthermore, Figure 13.1d shows the classification of different transmuralities. Fully transmural fibrosis was predominantly found in areas of high fibrotic density. Thus, not all high-density fibrotic areas are entirely transmural. In contrast to patients 1,3, and 4, patient 2 and patient 5 had a low similarity (55.74% and 58.76%, respectively) of low voltage and fibrotic areas due to a generally low peak-to-peak voltage in the electrograms.

13.3 Discussion

In this chapter, a novel approach was presented to characterize the patient's fibrotic substrate using the trained machine learning algorithm developed in chapter 11 using the recorded electrograms. Currently, voltage and activation time maps are used to guide ablation therapies [151]; however, they rely on manual annotation of the electrograms and do not provide information about the cardiac substrate. The generated fibrosis maps add additional information about the cardiac substrate and especially the fibrotic density and transmurallity, which could help to guide ablation procedures. The data-driven approach presented in this chapter overcomes the use of a single cut-off value to characterize the atrial fibrotic substrate. Although the model needs further validation, the present study is a proof of concept on how machine learning could help improve clinical treatments.

Chapter 14

Direct graph - Transfer entropy flow maps

Understanding the electrical propagation during atrial fibrillation (AF) is crucial for an optimal ablation strategy. Technologies like Coherent mapping [152] and STAR mapping [153] estimate the electrical propagation relying on the annotation of local activation time (LAT) of electrograms, which is hard to determine in complex signals. Transfer entropy (TE) measures the amount of information flow between two processes, and allows the study of the propagation's spatio-temporal dynamics without electrogram annotation.

14.1 Methods

This study includes five patients recruited at Städtisches Klinikum Karlsruhe with the diagnosis of persistent AF. The five patients recordings were used as a proof of concept to test our approach to characterize the atrial tissue from clinical electrograms. Patiens' electroanatomical maps and recordings were the same as used in chapter 13.

Electrograms were imported and stored in a standard structure where data from the geometry, recorded signals coordinates and time of recording were collected to create the directed graph and calculate TE. Recording time was used to overcome the limitation of non-sequential recording characteristic of the electrograms collected during an electrophysiology study. Afterwards, a directed graph (DG) was created to obtain the propagation direction. Regions of the atria where data were not collected was interpolated using the RBF described in Eq. 13.1.

The available recordings were mapped non sequentially. Therefore, a weighting coefficient was introduced to resolve the global direction of the wave front based on the recording time without the need of annotating local activation times on the acquired electrograms.

14.2 Results

Local and global direction is depicted in Figure 14.1. Electrograms collected from a close area showed local conduction direction (black arrow). White arrows indicate the global direction of the wave front. Red areas correspond with late activation times which in which global direction was going around. However, there were areas of late activation time where local direction was altered but followed the global direction. According to the results shown in Chapter 12 this might correspond with areas of low density fibrosis (10%).

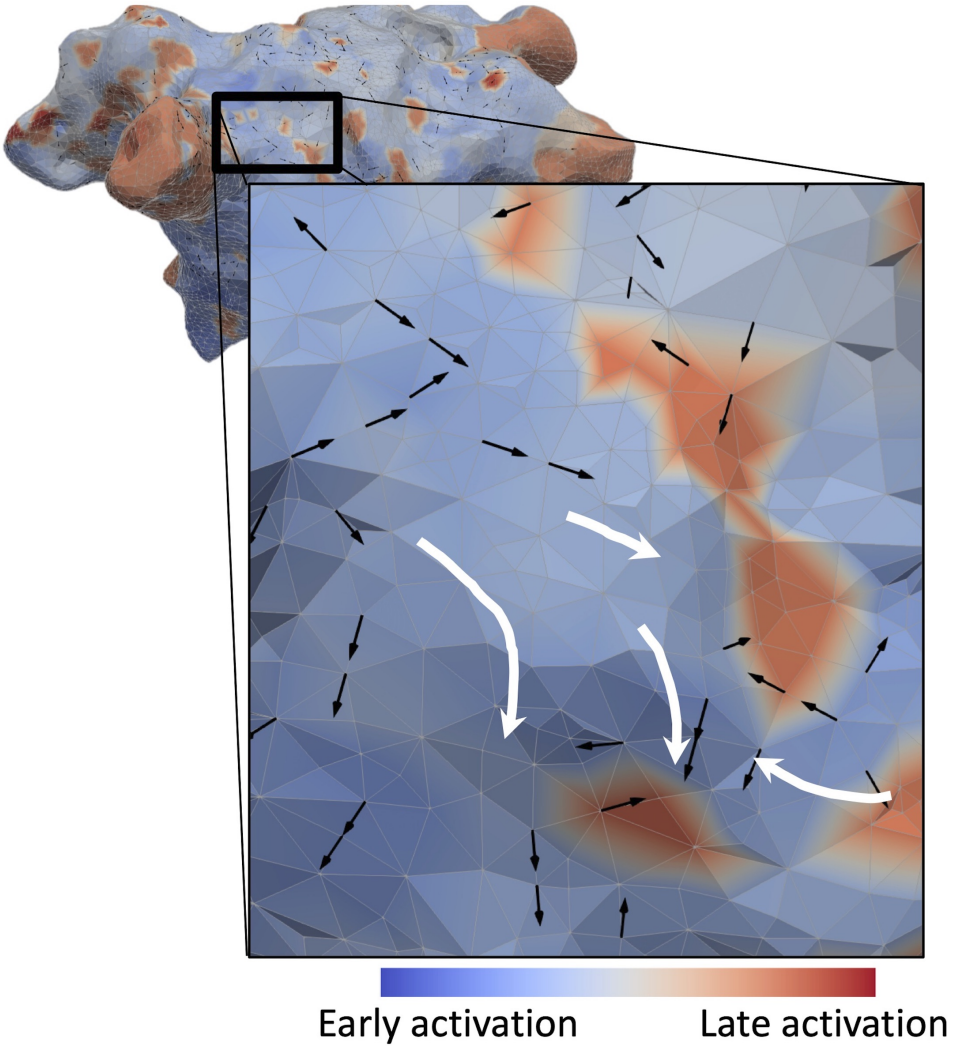

Figure 14.1: DG-TE flow map showing the local and global direction of the propagation during fibrillation. Black arrows indicate the local wave front propagation and white arrow indicate the global propagation. Local activation times are in the background as a reference.

14.3 Discussion

Current technologies such as Coherent map (Biosense) or STAR mapping [153] and other studies have shown the possibility to determine the wavefront direction and using a graph approach [154, 155]. Most of these methods rely on the annotation of LAT on the electrograms, which is not a trivial task under peAF due to fractionation of the signal.

In this proof of concept, we proposed a method that does not rely on the annotation of clinical electrograms and overcomes the limitation of nonsequential mapping by introducing a weighting coefficient to resolve the wavefront's global direction.

Chapter 15

Conclusion

This chapter summarizes and briefly discusses the main contributions of the present thesis, that go beyond the state of the art in translating computational modeling to clinical applications. The main conclusions corresponding to the specific objectives defined in this thesis are summarized as follows:

1. Characterization of the fibroblast/myofibroblast electrophysiology and its impact on myocyte action potential
Cardiac structural remodeling is a complex process that involves the interaction of different types of cells that are present in the cardiac tissue. During persistent atrial fibrillation, the presence of fibrosis modifies electrical propagation in cardiac tissue. However, in this thesis, the fibrotic tissue composition was explored using computational models at different scales. Fibroblast differentiation to myofibroblast is a key factor in understanding the dynamics of electrical propagation. In this thesis, the characterization of the electrophysiology of human atrial myofibroblast was assessed by fitting the model parameters to existing experimental data. Moreover, the RMP and sodium current of myofibroblast is of great importance in cardiac propagation.

2. Analysis of the role of calcium channels in myofibroblast electrophysiology and its intracellular calcium handling system
Additionally, in silico experiments allowed to go beyond the limitations of in vitro experiments and explore more in detail the electrophysiogy of isolated cells. In this thesis, we explored the presence of ionic calcium channels in the membrane of the myofibroblast and the intracellular handling. These results are in accordance with the literature and could explain the wide range of data due to the fibroblasts' ability to differentiate and express different ionic currents.

3. Quantification of the impact on arrhythmogenicity of myofibroblast infiltration in atrial tissue during atrial fibrillation
At the tissue level, a high density of myofibroblasts will lead to a block of conduction, and reentry activity that is anchored to the border of the area where myofibroblasts were present.

Interestingly, in case of myofibroblasts' low density this allows the reentry to meander inside the area defined as fibrotic, changing the dynamics of the fibrillatory event. Increased myofibroblast density induces a biphasic behavior of the tissues vulnerability where the reentry activity progresses from functional to an anatomical due to the conduction block.

4. Investigation of fibrosis composition and the effect on electrogram signals
The study of tissue fibrosis was carried out, looking at how fibrosis increases the tissue's vulnerability to trigger a reentry event and how the composition alters the intracardiac signal collected at the surface of the tissue. Longer duration of electrograms was observed when fibrosis was composed of myofibroblast; however, by introducing a third component such as collagen electrograms where fractionated due alteration of the wave propagation.

5. Analysis of the use of electrogram signals to characterize fibrotic substrate
Simulated electrograms were compared with clinical signals from healthy tissue to validate the modeling methodology. Realistic modeling of the catheter and a clinical noise model was used to create realistic signals compared with in vivo recordings. To further verify and validate the proposed modeling in this Thesis, the ASME V&V40 recommendations were followed. After the validation of the model and the creation of 1048 different simulations, a machine learning algorithm was used to characterize the fibrotic substrate. This study showed that machine learning provides information about the cardiac fibrotic substrate without the need to set a single cut-off value to distinguish healthy tissue from pathological tissue.

6. Investigation of the use of non-parametric measurements to understand the electrical propagation in cardiac tissue
Throughout this Thesis, it was shown that fibrosis alters the propagation of the depolarization wavefront. Therefore, transfer entropy in a combination of directed graphs was used to indicate the depolarization wavefront's direction. Transfer entropy does not need annotation of the electrograms, which is advantageous when the signals are fractioned. As a proof of concept, fibrosis maps and DG-TE maps were created to characterize the patients' fibrotic substrate and the direction of the wavefront from clinical recordings.

General conclusion
In conclusion, in silico experiments help to study and understand the electrophysiology of isolated cells. Moreover, in silico experiments can be extended to tissue level simulation to study how different cells and collagen interact and change the depolarization wavefront. In addition, in silico data were used to synergistically create a dataset with in vivo recordings to train machine learning algorithms that can be used to guide ablation therapies. During electrophysiology studies, knowing the depolarization wavefront direction helps understand the dynamics of the reentrant activity. DG-TE flow allows to create a map that indicates the wavefront direction with no need of electrogram annotation.

Chapter 16

Outlook

At the cellular level, the investigation of calcium ionic currents and intracellular calcium handling can be further extended to validate the results. Additionally, the main hypothesis for including calcium dynamics in the myofibroblasts electrophysiology is under the assumption that myofibroblasts are cells that can mechanically contract. Therefore, coupled simulations of electrophysiology and mechanics can be carried out to fully understand intracellular calcium handling at the cellular level. Additionally, at the tissue level, coupled simulations can assess the effect of heterogeneous contraction during atrial fibrillation.

The model of the atria which included the catheter's model can be further developed to create a more realistic setup that better reflects clinical recordings. Furthermore, exploring the advantage of the open code of openCARP a simulated electrogram reference electrode can be extended to use an external signal that corresponds to the Wilson central terminal, which is used in clinical setups as a reference signal. Additionally, the Discontinuous Galerkin method can be implemented in openCARP to study the cardiac tissue's fibrotic composition at a microscale resolution.

Further studies can be carried out to improve the machine learning algorithm to characterize the atrial substrate better. From the created matrices of TE, machine learning algorithm can be trained to characterize the depolarization pattern and identify regions that are driving the reentry activity.

With the increase of high-density electro-anatomical recordings, further investigation of the DG-TE can be developed to detect micro reentry loops and global macro loops that better support ablation therapies.

References

[1] G. Hindricks, T. Potpara, N. Dagres, et al., "2020 ESC Guidelines for the diagnosis and management of atrial fibrillation developed in collaboration with the European Association for Cardio-Thoracic Surgery (EACTS)," *European Heart Journal*, 8 2020.

[2] P. Camelliti, T. K. Borg, and P. Kohl, "Structural and functional characterisation of cardiac fibroblasts," *Cardiovascular Research*, vol. 65, no. 1, pp. 40–51, 2005.

[3] G. Gaudesius, M. Miragoli, S. P. Thomas, et al., "Coupling of cardiac electrical activity over extended distances by fibroblasts of cardiac origin," *Circulation Research*, vol. 93, no. 5, pp. 421–428, 2003.

[4] M. Hulsmans, S. Clauss, L. Xiao, et al., "Macrophages Facilitate Electrical Conduction in the Heart," *Cell*, vol. 169, no. 3, pp. 510–522, 2017.

[5] T. A. Quinn, P. Camelliti, E. A. Rog-Zielinska, et al., "Electrotonic coupling of excitable and nonexcitable cells in the heart revealed by optogenetics," *Proceedings of the National Academy of Sciences*, vol. 113, no. 51, pp. 14 852–14 857, 2016.

[6] Y. Xie, A. Garfinkel, P. Camelliti, et al., "Effects of fibroblast-myocyte coupling on cardiac conduction and vulnerability to reentry: A computational study," *Heart Rhythm*, vol. 6, no. 11, pp. 1641–1649, 11 2009.

[7] R. Bosch, X. Zeng, J. Grammer, et al., "Ionic mechanisms of electrical remodeling in human atrial fibrillation." *Cardiovascular research*, vol. 44, no. 1, pp. 121–31, 1999.

[8] S. Rohr, "Myofibroblasts in diseased hearts: New players in cardiac arrhythmias?" *Heart Rhythm*, vol. 6, no. 6, pp. 848–856, 2009.

[9] C. Yao, T. Veleva, and E. Al, "Enhanced Cardiomyocyte NLRP3 Inflammasome Signaling," *Circulation*, 2018.

[10] G. Chen, M. G. Chelu, D. Dobrev, et al., "Cardiomyocyte Inflammasome Signaling in Cardiomyopathies and Atrial Fibrillation: Mechanisms and Potential Therapeutic Implications," *Frontiers in Physiology*, vol. 9, no. August, pp. 1–7, 8 2018.

[11] S. Zahid, H. Cochet, P. M. Boyle, et al., "Patient-derived models link re-entrant driver localization in atrial fibrillation to fibrosis spatial pattern," *Cardiovascular Research*, vol. 110, no. 3, pp. 443–454, 2016.

[12] S. Hinderer and K. Schenke-layland, "Cardiac fi brosis – A short review of causes and therapeutic strategies," *Advanced Drug Delivery Reviews*, vol. 146, pp. 77–82, 2019.

[13] N. Salvarani, A. Maguy, S. A. De Simone, et al., "TGF-β1(Transforming Growth Factor-β1) Plays a Pivotal Role in Cardiac Myofibroblast Arrhythmogenicity," *Circulation: Arrhythmia and Electrophysiology*, vol. 10, no. 5, 2017.

[14] F. Jousset, A. Maguy, S. Rohr, et al., "Myofibroblasts electrotonically coupled to cardiomyocytes alter conduction: Insights at the cellular level from a detailed in silico tissue structure model," *Frontiers in Physiology*, vol. 7, no. OCT, pp. 1–23, 2016.

[15] M. Miragoli, G. Gaudesius, and S. Rohr, "Electrotonic modulation of cardiac impulse conduction by myofibroblasts," *Circulation Research*, vol. 98, no. 6, pp. 801–810, 2006.

[16] M. S. Dzeshka, G. Y. Lip, V. Snezhitskiy, et al., "Cardiac Fibrosis in Patients With Atrial Fibrillation: Mechanisms and Clinical Implications," *Journal of the American College of Cardiology*, vol. 66, no. 8, pp. 943–959, 2015.

[17] A. S. Jadidi, H. Lehrmann, C. Keyl, et al., "Ablation of Persistent Atrial Fibrillation Targeting Low-Voltage Areas with Selective Activation Characteristics," *Circulation: Arrhythmia and Electrophysiology*, vol. 9, no. 3, pp. 1–11, 2016.

[18] G. Yang, B. Yang, Y. Wei, et al., "Catheter Ablation of Nonparoxysmal Atrial Fibrillation Using Electrophysiologically Guided Substrate Modification during Sinus Rhythm after Pulmonary Vein Isolation," *Circulation: Arrhythmia and Electrophysiology*, vol. 9, no. 2, pp. 1–11, 2016.

[19] A. S. Jadidi, H. Cochet, A. J. Shah, et al., "Inverse relationship between fractionated electrograms and atrial fibrosis in persistent atrial fibrillation: Combined magnetic resonance imaging and high-density mapping," *Journal of the American College of Cardiology*, vol. 62, no. 9, pp. 802–812, 2013.

[20] F. O. Campos, T. Wiener, A. J. Prassl, et al., "Electroanatomical Characterization of Atrial Microfibrosis in a Histologically Detailed Computer Model," *IEEE Transactions on Biomedical Engineering*, vol. 60, no. 8, pp. 2339–2349, 8 2013.

[21] B. S. Handa, X. Li, K. K. Aras, et al., "Granger Causality–Based Analysis for Classification of Fibrillation Mechanisms and Localization of Rotational Drivers," *Circulation: Arrhythmia and Electrophysiology*, vol. 13, no. 3, 3 2020.

[22] T. A. Gokhale, E. Medvescek, and C. S. Henriquez, "Modeling dynamics in diseased cardiac tissue: Impact of model choice," *Chaos*, vol. 27, no. 9, 2017.

[23] C. Mendonca Costa, F. O. Campos, A. J. Prassl, et al., "An Efficient Finite Element Approach for Modeling Fibrotic Clefts in the Heart," *IEEE Transactions on Biomedical Engineering*, vol. 61, no. 3, pp. 900–910, 3 2014.

[24] C. H. Roney, C. D. Cantwell, J. D. Bayer, et al., "Spatial Resolution Requirements for Accurate Identification of Drivers of Atrial Fibrillation," *Circulation: Arrhythmia and Electrophysiology*, vol. 10, no. 5, p. e004899, 2017.

[25] M. Saha, C. H. Roney, J. D. Bayer, et al., "Wavelength and fibrosis affect phase singularity locations during atrial fibrillation," *Frontiers in Physiology*, vol. 9, no. SEP, 2018.

[26] E. Vigmond, A. Pashaei, S. Amraoui, et al., "Percolation as a mechanism to explain atrial fractionated electrograms and reentry in a fibrosis model based on imaging data," *Heart Rhythm*, vol. 13, no. 7, pp. 1536–1543, 2016.

[27] C. H. Roney, J. D. Bayer, S. Zahid, et al., "Modelling methodology of atrial fibrosis affects rotor dynamics and electrograms," *EP Europace*, vol. 18, no. suppl_4, pp. iv146–iv155, 12 2016.

[28] M. W. Keller, S. Schuler, M. Wilhelms, et al., "Characterization of radiofrequency ablation lesion development based on simulated and measured intracardiac electrograms," *IEEE Transactions on Biomedical Engineering*, vol. 61, no. 9, pp. 2467–2478, 2014.

[29] Y. J. Lin, M. T. Lo, S. L. Chang, et al., "Benefits of Atrial Substrate Modification Guided by Electrogram Similarity and Phase Mapping Techniques to Eliminate Rotors and Focal Sources Versus Conventional Defragmentation in Persistent Atrial Fibrillation," *JACC: Clinical Electrophysiology*, vol. 2, no. 6, pp. 667–678, 2016.

[30] L. Staerk, J. A. Sherer, D. Ko, et al., "Atrial Fibrillation," *Circulation Research*, vol. 120, no. 9, pp. 1501–1517, 2017.

[31] I. A. POLEJAEVA, R. RANJAN, C. J. DAVIES, et al., "Increased Susceptibility to Atrial Fibrillation Secondary to Atrial Fibrosis in Transgenic Goats Expressing Transforming Growth Factor-β1," *Journal of Cardiovascular Electrophysiology*, vol. 27, no. 10, pp. 1220–1229, 10 2016.

[32] S. Kirubakaran, R. A. Chowdhury, M. C. Hall, et al., "Fractionation of electrograms is caused by colocalized conduction block and connexin disorganization in the absence of fibrosis as AF becomes persistent in the goat model," *Heart Rhythm*, vol. 12, no. 2, pp. 397–408, 2 2015.

[33] C. McGann, N. Akoum, A. Patel, et al., "Atrial Fibrillation Ablation Outcome Is Predicted by Left Atrial Remodeling on MRI," *Circulation: Arrhythmia and Electrophysiology*, vol. 7, no. 1, pp. 23–30, 2 2014.

[34] A. L. Hodgkin and A. F. Huxley, "A quantitative description of membrane current and its application to conduction and excitation in nerve," *The Journal of Physiology*, vol. 117, no. 4, pp. 500–544, 8 1952.

[35] B. F. Nielsen, T. S. Ruud, G. T. Lines, et al., "Optimal monodomain approximations of the bidomain equations," *Applied Mathematics and Computation*, vol. 184, no. 2, pp. 276–290, 1 2007.

[36] J. Sánchez, J. F. Gomez, L. Martinez-Mateu, et al., "Heterogeneous Effects of Fibroblast-Myocyte Coupling in Different Regions of the Human Atria Under Conditions of Atrial Fibrillation," *Frontiers in Physiology*, vol. 10, 7 2019.

[37] J. Sánchez, M. Nothstein, A. Neic, et al., "openCARP: An Open Sustainable Framework for In-Silico Cardiac Electrophysiology Research," in *2020 Computing in Cardiology Conference (CinC)*, 12 2020.

[38] E. J. Vigmond, M. Hughes, G. Plank, et al., "Computational tools for modeling electrical activity in cardiac tissue," *Journal of Electrocardiology*, vol. 36, pp. 69–74, 12 2003.

[39] D. Nairn, D. Hunyar, J. Sánchez, et al., "Impact of Electrode Size on Electrogram Voltage in Healthy and Diseased Tissue," 12 2020.

[40] S. Schuler, M. W. Keller, T. Oesterlein, et al., "Influence of Catheter Orientation, Tissue Thickness and Conduction Velocity on the Intracardiac Electrogram," *Biomedical Engineering / Biomedizinische Technik*, 1 2013.

[41] Y. Kim, S. Chen, S. Ernst, et al., "2019 APHRS expert consensus statement on three-dimensional mapping systems for tachycardia developed in collaboration with HRS, EHRA, and LAHRS," *Journal of Arrhythmia*, vol. 36, no. 2, pp. 215–270, 4 2020.

[42] F. E. Marchlinski, D. J. Callans, C. D. Gottlieb, et al., "Linear Ablation Lesions for Control of Unmappable Ventricular Tachycardia in Patients With Ischemic and Nonischemic Cardiomyopathy," *Circulation*, vol. 101, no. 11, pp. 1288–1296, 3 2000.

[43] A. Jadidi, M. Nothstein, J. Chen, et al., "Specific Electrogram Characteristics Identify the Extra-Pulmonary Vein Arrhythmogenic Sources of Persistent Atrial Fibrillation – Characterization of the Arrhythmogenic Electrogram Patterns During Atrial Fibrillation and Sinus Rhythm," *Scientific Reports*, vol. 10, no. 1, p. 9147, 12 2020.

[44] D. D. Spragg, I. Khurram, S. L. Zimmerman, et al., "Initial experience with magnetic resonance imaging of atrial scar and co-registration with electroanatomic voltage mapping during atrial fibrillation: Success and limitations," *Heart Rhythm*, vol. 9, no. 12, pp. 2003–2009, 12 2012.

[45] J. T. Koivumaki, J. Takalo, T. Korhonen, et al., "Modelling sarcoplasmic reticulum calcium ATPase and its regulation in cardiac myocytes," *Philosophical Transactions of the Royal Society A: Mathematical, Physical and Engineering Sciences*, vol. 367, no. 1896, pp. 2181–2202, 2009.

[46] M. Krueger, G. Seemann, K. Rhode, et al., "Personalization of Atrial Anatomy and Elelectophysiology as a Basis for Clinical Modeling of Radio-Frequency-Ablation of Atrial Fibrillation," *Medical Imaging, IEEE Transactions on*, vol. 32, no. 99, pp. 1–12, 2012.

[47] A. Ferrer, R. Sebastián, D. Sánchez-Quintana, et al., "Detailed anatomical and electrophysiological models of human atria and torso for the simulation of atrial activation," *PLoS ONE*, vol. 10, no. 11, pp. 1–29, 2015.

[48] J. T. Koivumäki, G. Seemann, M. M. Maleckar, et al., "In Silico Screening of the Key Cellular Remodeling Targets in Chronic Atrial Fibrillation," *PLoS Computational Biology*, vol. 10, no. 5, 2014.

[49] M. L. Koller, M. L. Riccio, and R. F. G. Jr., "Dynamic restitution of action potential duration during electrical alternans and ventricular fibrillation," *American Journal of Physiology-Heart and Circulatory Physiology*, vol. 275, no. 5, 11 1998.

[50] openCARP project, "Single-cell APD restitution," 4 2020.

[51] A. J. Workman, K. A. Kane, A. C. Rankin, et al., "The contribution of ionic currents to changes in refractoriness of human atrial myocytes associated with chronic atrial fibrillation." *Cardiovascular research*, vol. 52, no. 2, pp. 226–35, 2001.

[52] D. Dobrev and U. Ravens, "Remodeling of cardiomyocyte ion channels in human atrial fibrillation." *Basic research in cardiology*, vol. 98, no. 3, pp. 137–48, 2003.

[53] N. Voigt, J. Heijman, A. Trausch, et al., "Impaired Na+-dependent regulation of acetylcholine-activated inward-rectifier K+ current modulates action potential rate dependence in patients with chronic atrial fibrillation," *Journal of Molecular and Cellular Cardiology*, vol. 61, pp. 142–152, 2013.

[54] C. Sánchez, A. Bueno-Orovio, E. Wettwer, et al., "Inter-subject variability in human atrial action potential in sinus rhythm versus chronic atrial fibrillation," *PLoS ONE*, vol. 9, no. 8, 2014.

[55] D. Dobrev, E. Graf, E. Wettwer, et al., "Molecular Basis of Downregulation of G-Protein–Coupled Inward Rectifying K ⁺ Current (I _{K,ACh}) in Chronic Human Atrial Fibrillation," *Circulation*, vol. 104, no. 21, 11 2001.

[56] H. Katoh, T. Shinozaki, S. Baba, et al., "Monophasic action potential duration at the crista terminalis in patients with sinus node disease." *Circulation journal : official journal of the Japanese Circulation Society*, vol. 69, no. 11, pp. 1361–1367, 2005.

[57] L. Skibsbye, T. Jespersen, T. Christ, et al., "Refractoriness in human atria: Time and voltage dependence of sodium channel availability." *Journal of molecular and cellular cardiology*, vol. 101, pp. 26–34, 2016.

[58] T. J. Cha, J. R. Ehrlich, L. Zhang, et al., "Atrial tachycardia remodeling of pulmonary vein cardiomyocytes: Comparison with left atrium and potential relation to arrhythmogenesis," *Circulation*, vol. 111, no. 6, pp. 728–735, 2005.

[59] M. A. Colman, O. V. Aslanidi, S. Kharche, et al., "Pro-arrhythmogenic effects of atrial fibrillation-induced electrical remodelling: insights from the three-dimensional virtual human atria." *The Journal of physiology*, vol. 591, no. 17, pp. 4249–72, 2013.

[60] M. Krüger, *Personalized Multi-Scale Modeling of the Atria*, vol. 19, 2012.

[61] M. Varela, M. A. Colman, J. C. Hancox, et al., "Atrial Heterogeneity Generates Re-entrant Substrate during Atrial Fibrillation and Anti-arrhythmic Drug Action: Mechanistic Insights from Canine Atrial Models," *PLoS Computational Biology*, vol. 12, no. 12, pp. 1–22, 2016.

[62] U. M. R. Avula, J. Abrams, A. Katchman, et al., "Heterogeneity of the action potential duration is required for sustained atrial fibrillation," *JCI Insight*, vol. 4, no. 11, 6 2019.

[63] C. H. Roney, J. D. Bayer, H. Cochet, et al., "Variability in pulmonary vein electrophysiology and fibrosis determines arrhythmia susceptibility and dynamics," *PLoS Computational Biology*, vol. 14, no. 5, 2018.

[64] D. E. Krummen, J. D. Bayer, J. Ho, et al., "Mechanisms of Human Atrial Fibrillation Initiation," *Circulation: Arrhythmia and Electrophysiology*, vol. 5, no. 6, 12 2012.

[65] K. A. MacCannell, H. Bazzazi, L. Chilton, et al., "A mathematical model of electrotonic interactions between ventricular myocytes and fibroblasts." *Biophysical journal*, vol. 92, no. 11, pp. 4121–32, 2007.

[66] R. Morgan, M. A. Colman, H. Chubb, et al., "Slow conduction in the border zones of patchy fibrosis stabilizes the drivers for atrial fibrillation: Insights from multi-scale human atrial modeling," *Frontiers in Physiology*, vol. 7, no. OCT, pp. 1–15, 2016.

[67] M. M. Maleckar, J. L. Greenstein, W. R. Giles, et al., "Electrotonic coupling between human atrial myocytes and fibroblasts alters myocyte excitability and repolarization," *Biophysical Journal*, vol. 97, no. 8, pp. 2179–2190, 2009.

[68] J. Koivumäki, R. B. Clark, D. Belke, et al., "Na+ current expression in human atrial myofibroblasts: Identity and functional roles," *Frontiers in Physiology*, vol. 5 JUL, no. August, pp. 1–14, 2014.

[69] C. Poulet, S. Künzel, E. Büttner, et al., "Altered physiological functions and ion currents in atrial fibroblasts from patients with chronic atrial fibrillation." *Physiological reports*, vol. 4, no. 2, p. e12681, 2016.

[70] M. Kumar, M. Husain, N. Upreti, et al., "Genetic Algorithm: Review and Application," *SSRN Electronic Journal*, 2010.

[71] B. Burstein and S. Nattel, "Atrial Fibrosis: Mechanisms and Clinical Relevance in Atrial Fibrillation," *Journal of the American College of Cardiology*, vol. 51, no. 8, pp. 802–809, 2008.

[72] M. M. Maleckar, J. L. Greenstein, W. R. Giles, et al., "Electrotonic coupling between human atrial myocytes and fibroblasts alters myocyte excitability and repolarization," *Biophysical Journal*, vol. 97, no. 8, pp. 2179–2190, 2009.

[73] S. Sridhar, N. Vandersickel, and A. V. Panfilov, "Effect of myocyte-fibroblast coupling on the onset of pathological dynamics in a model of ventricular tissue," *Scientific Reports*, vol. 7, no. September 2016, p. 40985, 2017.

[74] V. Jacquemet and C. S. Henriquez, "Loading effect of fibroblast-myocyte coupling on resting potential, impulse propagation, and repolarization: insights from a microstructure model," *AJP: Heart and Circulatory Physiology*, vol. 294, no. 5, pp. H2040–H2052, 2008.

[75] V. Jacquemet and C. S. Henriquez, "Modelling cardiac fibroblasts: interactions with myocytes and their impact on impulse propagation." *Europace : European pacing, arrhythmias, and cardiac electrophysiology : journal of the working groups on cardiac pacing, arrhythmias, and cardiac cellular electrophysiology of the European Society of Cardiology*, vol. 9 Suppl 6, 2007.

[76] K. S. McDowell, F. Vadakkumpadan, R. Blake, et al., "Mechanistic inquiry into the role of tissue remodeling in fibrotic lesions in human atrial fibrillation," *Biophysical Journal*, vol. 104, no. 12, pp. 2764–2773, 2013.

[77] M. Funken, T. Bruegmann, and P. Sasse, "Selective optogenetic stimulation of fibroblasts enables quantification of hetero-cellular coupling to cardiomyocytes in a three-dimensional model of heart tissue," *EP Europace*, vol. 22, no. 10, pp. 1590–1599, 10 2020.

[78] S. O. Rahaman, L. M. Grove, S. Paruchuri, et al., "TRPV4 mediates myofibroblast differentiation and pulmonary fibrosis in mice," *Journal of Clinical Investigation*, vol. 124, no. 12, pp. 5225–5238, 12 2014.

[79] H. Bae, T. Kim, and I. Lim, "Effects of nitric oxide on apoptosis and voltage-gated calcium channels in human cardiac myofibroblasts," *Clinical and Experimental Pharmacology and Physiology*, vol. 47, no. 1, pp. 16–26, 1 2020.

[80] T. De Coster, P. Claus, I. V. Kazbanov, et al., "Arrhythmogenicity of fibro-fatty infiltrations," *Scientific Reports*, vol. 8, no. 1, pp. 1–9, 2018.

[81] M. Courtemanche, R. J. Ramirez, and S. Nattel, "Ionic mechanisms underlying human atrial action potential properties: insights from a mathematical model," *American Journal of Physiology-Heart and Circulatory Physiology*, vol. 275, no. 1, pp. H301–H321, 7 1998.

[82] F. J. Ramires, Y. Sun, and K. T. Weber, "Myocardial Fibrosis Associated with Aldosterone or Angiotensin II Administration: Attenuation by Calcium Channel Blockade," *Journal of Molecular and Cellular Cardiology*, vol. 30, no. 3, pp. 475–483, 3 1998.

[83] J. T. Colston, B. Chandrasekar, and G. L. Freeman, "A Novel Peroxide-induced Calcium Transient Regulates Interleukin-6 Expression in Cardiac-derived Fibroblasts," *Journal of Biological Chemistry*, vol. 277, no. 26, pp. 23 477–23 483, 6 2002.

[84] I. Kiseleva, A. Kamkin, A. Pylaev, et al., "Electrophysiological Properties of Mechanosensitive Atrial Fibroblasts From Chronic Infarcted Rat Heart," *Journal of Molecular and Cellular Cardiology*, vol. 30, no. 6, pp. 1083–1093, 6 1998.

[85] G. C. Bett, A. D. Kaplan, A. Lis, et al., "Electronic "expression" of the inward rectifier in cardiocytes derived from human-induced pluripotent stem cells," *Heart Rhythm*, vol. 10, no. 12, pp. 1903–1910, 12 2013.

[86] G. M. Kostecki, Y. Shi, C. S. Chen, et al., "Optogenetic current in myofibroblasts acutely alters electrophysiology and conduction of co-cultured cardiomyocytes," *Scientific Reports*, vol. 11, no. 1, p. 4430, 12 2021.

[87] J. Sánchez, B. Trénor, J. Saiz, et al., "In Silico Analysis of the Effects of Fibroblasts Coupling to Atrial Myocytes under Conditions of Atrial Fibrillation Remodeling Materials and methods," vol. 44, pp. 1–4, 2017.

[88] K. Ten Tusscher, D. Noble, P. J. Noble, et al., "A model for human ventricular tissue," *American Journal of Physiology-Heart and Circulatory Physiology*, vol. 286, no. 4, p. H1573, 2004.

[89] M. A. Sabir, F. W. Sosulski, and A. J. Finlayson, "Chlorogenic Acid-Protein Interactions in Sunflower," *Journal of Agricultural and Food Chemistry*, vol. 22, no. 4, pp. 575–578, 1974.

[90] R. A. Gray, A. M. Pertsov, and J. Jalife, "Spatial and temporal organization during cardiac fibrillation," *Nature*, vol. 392, no. 6671, pp. 75–78, 3 1998.

[91] M. Warren, P. K. Guha, O. Berenfeld, et al., "Blockade of the inward rectifying potassium current terminates ventricular fibrillation in the guinea pig heart," *Journal of Cardiovascular Electrophysiology*, vol. 14, no. 6, pp. 621–631, 2003.

[92] M. Yamazaki, S. Mironov, C. Taravant, et al., "Heterogeneous atrial wall thickness and stretch promote scroll waves anchoring during atrial fibrillation," *Cardiovascular Research*, vol. 94, no. 1, pp. 48–57, 2012.

[93] M. Wilhelms, H. Hettmann, M. M. Maleckar, et al., "Benchmarking electrophysiological models of human atrial myocytes," *Frontiers in Physiology*, vol. 3 JAN, no. January, pp. 1–16, 2013.

[94] I. Fernandez-Lozano, J. Toquero-Ramos, C. Escudero-Vela, et al., "[Left atrial posterior wall and pulmonary vein refractory periods are associated with atrial fibrillation inducibility in a swine model]," *Rev Esp Cardiol*, vol. 59, no. 7, pp. 653–661, 2006.

[95] F. B. Sachse, A. P. Moreno, and J. A. Abildskov, "Electrophysiological modeling of fibroblasts and their interaction with myocytes," *Annals of Biomedical Engineering*, vol. 36, no. 1, pp. 41–56, 2008.

[96] H.-q. Zhan, L. Xia, G.-f. Shou, et al., "Fibroblast proliferation alters cardiac excitation conduction and contraction: a computational study," *Journal of Zhejiang University SCIENCE B*, vol. 15, no. 3, pp. 225–242, 2014.

[97] L. Yue, J. Xie, and S. Nattel, "Molecular determinants of cardiac fibroblast electrical function and therapeutic implications for atrial fibrillation," *Cardiovascular Research*, vol. 89, no. 4, pp. 744–753, 2011.

[98] K. Tanaka, S. Zlochiver, K. L. Vikstrom, et al., "Spatial distribution of fibrosis governs fibrillation wave dynamics in the posterior left atrium during heart failure," *Circulation Research*, vol. 101, no. 8, pp. 839–847, 2007.

[99] T. P. Nguyen, Y. Xie, A. Garfinkel, et al., "Arrhythmogenic consequences of myofibroblastmyocyte coupling," *Cardiovascular Research*, vol. 93, no. 2, pp. 242–251, 2012.

[100] R. Gaspo, R. F. Bosch, M. Talajic, et al., "Functional Mechanisms Underlying Tachycardia-Induced Sustained Atrial Fibrillation in a Chronic Dog Model," *Circulation*, vol. 96, no. 11, pp. 4027–4035, 12 1997.

[101] T. H. Everett and J. E. Olgin, "Atrial fibrosis and the mechanisms of atrial fibrillation," *Heart Rhythm*, vol. 4, no. 3, pp. S24–S27, 3 2007.

[102] S. Verheule, J. Eckstein, D. Linz, et al., "Role of endo-epicardial dissociation of electrical activity and transmural conduction in the development of persistent atrial fibrillation," *Progress in Biophysics and Molecular Biology*, vol. 115, no. 2-3, pp. 173–185, 8 2014.

[103] M. A. Colman, *Mechanisms of Atrial Arrhythmias*, Springer Theses. Cham: Springer International Publishing, 2014.

[104] T. Ashihara, R. Haraguchi, K. Nakazawa, et al., "The role of fibroblasts in complex fractionated electrograms during persistent/permanent atrial fibrillation: Implications for electrogram-based catheter ablation," *Circulation Research*, vol. 110, no. 2, pp. 275–284, 2012.

[105] J. F. Gomez, K. Cardona, L. Romero, et al., "Electrophysiological and structural remodeling in heart failure modulate arrhythmogenesis. 1D simulation study," *PLoS ONE*, vol. 9, no. 9, 2014.

[106] J. W. Waks and M. E. Josephson, "Mechanisms of Atrial Fibrillation – Reentry, Rotors and Reality," *Arrhythmia & Electrophysiology Review*, vol. 3, no. 2, p. 90, 2014.

[107] J. F. Gomez, K. Cardona, L. Romero, et al., "Heterogeneous Electrical Remodeling of the Failing Heart Modulates the Arrhythmogenic Substrate," *Computing in Cardiology*, pp. 49–52, 2013.

[108] S. P. Krul, W. R. Berger, N. W. Smit, et al., "Atrial fibrosis and conduction slowing in the left atrial appendage of patients undergoing thoracoscopic surgical pulmonary vein isolation for atrial fibrillation," *Circulation: Arrhythmia and Electrophysiology*, vol. 8, no. 2, pp. 288–295, 2015.

[109] F. O. Campos, Y. Shiferaw, R. Weber dos Santos, et al., "Microscopic Isthmuses and Fibrosis Within the Border Zone of Infarcted Hearts Promote Calcium-Mediated Ectopy and Conduction Block," *Frontiers in Physics*, vol. 6, no. June, pp. 1–14, 2018.

[110] R. Morgan, M. Colman, M. Kruger, et al., "Evaluating Effects of Fibrosis in Atrial Arrhythmogenesis using 3D Computational Modelling," *Computing in Cardiology*, pp. 765–768, 2014.

[111] J. Greiner, A. C. Sankarankutty, G. Seemann, et al., "Confocal Microscopy-Based Estimation of Parameters for Computational Modeling of Electrical Conduction in the Normal and Infarcted Heart," *Frontiers in Physiology*, vol. 9, 4 2018.

[112] J. Sánchez, M. Nothstein, L. Unger, et al., "Influence of Fibrotic Tissue Arrangement on Intracardiac Electrograms During Persistent Atrial Fibrillation," in *2019 Computing in Cardiology (CinC)*, 2019, pp. 1–4.

[113] C. Schilling, M. P. Nguyen, A. Luik, et al., "Non-linear energy operator for the analysis of intracardial electrograms," *IFMBE Proceedings*, vol. 25, no. 4, pp. 872–875, 2009.

[114] C. E. Shannon, "A Mathematical Theory of Communication," *Bell System Technical Journal*, vol. 27, no. 4, pp. 623–656, 10 1948.

[115] C. Sánchez, A. Bueno-Orovio, E. Pueyo, et al., "Atrial Fibrillation Dynamics and Ionic Block Effects in Six Heterogeneous Human 3D Virtual Atria with Distinct Repolarization Dynamics," *Frontiers in Bioengineering and Biotechnology*, vol. 5, 5 2017.

[116] B. Abdi, R. C. Hendriks, A.-J. van der Veen, et al., "Improved local activation time annotation of fractionated atrial electrograms for atrial mapping," *Computers in Biology and Medicine*, vol. 117, p. 103590, 2 2020.

[117] B. Lim, J. Kim, M. Hwang, et al., "In situ procedure for high-efficiency computational modeling of atrial fibrillation reflecting personal anatomy, fiber orientation, fibrosis, and electrophysiology," *Scientific Reports*, vol. 10, no. 1, p. 2417, 12 2020.

[118] J. Sánchez, G. Luongo, M. Nothstein, et al., "Using Machine Learning to Characterize Atrial Fibrotic Substrate from Intracardiac Signals using a Hybrid in silico and in vivo Dataset," 2021.

[119] L. Clerc, "Directional differences of impulse spread in trabecular muscle from mammalian heart." *The Journal of Physiology*, vol. 255, no. 2, pp. 335–346, 2 1976.

[120] M. J. Bishop and G. Plank, "Representing cardiac bidomain bath-loading effects by an augmented monodomain approach: Application to complex ventricular models," *IEEE Transactions on Biomedical Engineering*, vol. 58, no. 4, pp. 1066–1075, 2011.

[121] N. Pilia, C. Nagel, G. Lenis, et al., "ECGdeli - An open source ECG delineation toolbox for MATLAB," *SoftwareX*, vol. 13, p. 100639, 1 2021.

[122] G. Luongo, S. Schuler, A. Luik, et al., "Non-Invasive Characterization of Atrial Flutter Mechanisms Using Recurrence Quantification Analysis on the ECG: a Computational Study," *IEEE Transactions on Biomedical Engineering*, pp. 1–1, 2020.

[123] M. Lown, M. Brown, C. Brown, et al., "Machine learning detection of Atrial Fibrillation using wearable technology," *PLOS ONE*, vol. 15, no. 1, 1 2020.

[124] A. Y. Hannun, P. Rajpurkar, M. Haghpanahi, et al., "Cardiologist-level arrhythmia detection and classification in ambulatory electrocardiograms using a deep neural network," *Nature Medicine*, vol. 25, no. 1, pp. 65–69, 1 2019.

[125] M. F. McGillivray, W. Cheng, N. S. Peters, et al., "Machine learning methods for locating re-entrant drivers from electrograms in a model of atrial fibrillation," *Royal Society Open Science*, vol. 5, no. 4, p. 172434, 4 2018.

[126] C. Schilling, M. Keller, D. Scherr, et al., "Fuzzy decision tree to classify complex fractionated atrial electrograms," *Biomedical Engineering / Biomedizinische Technik*, vol. 60, no. 3, 1 2015.

[127] M. Viceconti, F. Pappalardo, B. Rodriguez, et al., "In silico trials: Verification, validation and uncertainty quantification of predictive models used in the regulatory evaluation of biomedical products," *Methods*, 1 2020.

[128] M. Hwang, J. Kim, B. Lim, et al., "Multiple factors influence the morphology of the bipolar electrogram: An in silico modeling study." *PLoS computational biology*, vol. 15, no. 4, p. e1006765, 2019.

[129] ASME V&V 40, "Assessing Credibility of Computational Models Through Verification and Validation: Application to Medical Devices," 2018.

[130] S. A. Niederer, E. Kerfoot, A. P. Benson, et al., "Verification of cardiac tissue electrophysiology simulators using an N -version benchmark," *Philosophical Transactions of the Royal Society A: Mathematical, Physical and Engineering Sciences*, vol. 369, no. 1954, pp. 4331–4351, 11 2011.

[131] J. S. Richman and J. R. Moorman, "Physiological time-series analysis using approximate entropy and sample entropy," *American Journal of Physiology-Heart and Circulatory Physiology*, vol. 278, no. 6, pp. H2039–H2049, 6 2000.

[132] A. Vanluchene, H. Vereecke, O. Thas, et al., "Spectral Entropy as an Electroencephalographic Measure of Anesthetic Drug Effect: A Comparison with Bispectral Index and Processed Midlatency Auditory Evoked Response," *Anesthesiology*, vol. 101, no. 1, pp. 34–42, 7 2004.

[133] A. N. Kolmogorov, "Three approaches to the quantitative definition of information," *International Journal of Computer Mathematics*, vol. 2, no. 1-4, pp. 157–168, 1968.

[134] P. Y. Muller, N. Contento, and H. Rix, "Fractal dimension on ECG," in *1992 14th Annual International Conference of the IEEE Engineering in Medicine and Biology Society*, vol. 3, 10 1992, pp. 977–978.

[135] F. Yaghouby, A. Ayatollahi, R. Bahramali, et al., "Towards Automatic Detection of Atrial Fibrillation: A Hybrid Computational Approach," *Comput. Biol. Med.*, vol. 40, no. 11–12, p. 919–930, 11 2010.

[136] J. Zhang, S. Gajjala, P. Agrawal, et al., "Fully Automated Echocardiogram Interpretation in Clinical Practice," *Circulation*, vol. 138, no. 16, pp. 1623–1635, 2018.

[137] J. Rodrigues, D. Belo, and H. Gamboa, "Noise detection on ECG based on agglomerative clustering of morphological features," *Computers in Biology and Medicine*, vol. 87, pp. 322–334, 2017.

[138] G. Petmezas, K. Haris, L. Stefanopoulos, et al., "Automated Atrial Fibrillation Detection using a Hybrid CNN-LSTM Network on Imbalanced ECG Datasets," *Biomedical Signal Processing and Control*, vol. 63, p. 102194, 1 2021.

[139] F. Sahli Costabal, J. A. B. Zaman, E. Kuhl, et al., "Interpreting Activation Mapping of Atrial Fibrillation: A Hybrid Computational/Physiological Study," *Annals of Biomedical Engineering*, vol. 46, no. 2, pp. 257–269, 2018.

[140] S. R. Gutbrod, R. Walton, S. Gilbert, et al., "Quantification of the Transmural Dynamics of Atrial Fibrillation by Simultaneous Endocardial and Epicardial Optical Mapping in an Acute Sheep Model," *Circulation: Arrhythmia and Electrophysiology*, vol. 8, no. 2, pp. 456–465, 4 2015.

[141] I. V. Kazbanov, K. H. Ten Tusscher, and A. V. Panfilov, "Effects of Heterogeneous Diffuse Fibrosis on Arrhythmia Dynamics and Mechanism," *Scientific Reports*, vol. 6, no. February, pp. 1–14, 2016.

[142] S. Alonso and M. Bär, "Reentry Near the Percolation Threshold in a Heterogeneous Discrete Model for Cardiac Tissue," *Physical Review Letters*, vol. 110, no. 15, p. 158101, 4 2013.

[143] A. Roy, M. Varela, and O. Aslanidi, "Image-based computational evaluation of the effects of atrial wall thickness and fibrosis on re-entrant drivers for atrial fibrillation," *Frontiers in Physiology*, vol. 9, no. OCT, pp. 1–16, 10 2018.

[144] D. Deng, M. J. Murphy, J. B. Hakim, et al., "Sensitivity of reentrant driver localization to electrophysiological parameter variability in image-based computational models of persistent atrial fibrillation sustained by a fibrotic substrate," *Chaos*, vol. 27, no. 9, 2017.

[145] G. Balaban, B. P. Halliday, C. Mendonca Costa, et al., "Fibrosis Microstructure Modulates Reentry in Non-ischemic Dilated Cardiomyopathy: Insights From Imaged Guided 2D Computational Modeling," *Frontiers in Physiology*, vol. 9, no. December, pp. 1–13, 2018.

[146] F. O. Campos, J. Whitaker, R. Neji, et al., "Factors Promoting Conduction Slowing as Substrates for Block and Reentry in Infarcted Hearts," *Biophysical Journal*, vol. 117, no. 12, pp. 2361–2374, 2019.

[147] E. Van Nieuwenhuyse, T. Strisciuglio, G. Lorenzo, et al., "Evaluation of Directed Graph-Mapping in Complex Atrial Tachycardias," *JACC: Clinical Electrophysiology*, 3 2021.

[148] R. Vicente, M. Wibral, M. Lindner, et al., "Transfer entropy—a model-free measure of effective connectivity for the neurosciences," *Journal of Computational Neuroscience*, vol. 30, no. 1, pp. 45–67, 2 2011.

[149] T. Schreiber and A. Schmitz, "Surrogate time series," *Physica D: Nonlinear Phenomena*, vol. 142, no. 3-4, pp. 346–382, 8 2000.

[150] M. Rodrigo, A. M. Climent, A. Liberos, et al., "Identification of Dominant Excitation Patterns and Sources of Atrial Fibrillation by Causality Analysis," *Annals of Biomedical Engineering*, vol. 44, no. 8, pp. 2364–2376, 2016.

[151] N. M. de Groot, M. J. Schalij, K. Zeppenfeld, et al., "Voltage and Activation Mapping," *Circulation*, vol. 108, no. 17, 10 2003.

[152] E. Anter, M. Duytschaever, C. Shen, et al., "Activation Mapping With Integration of Vector and Velocity Information Improves the Ability to Identify the Mechanism and Location of Complex Scar-Related Atrial Tachycardias," *Circulation: Arrhythmia and Electrophysiology*, vol. 11, no. 8, 8 2018.

[153] S. Honarbakhsh, R. J. Schilling, M. Finlay, et al., "Prospective STAR-Guided Ablation in Persistent Atrial Fibrillation Using Sequential Mapping With Multipolar Catheters," *Circulation: Arrhythmia and Electrophysiology*, vol. 13, no. 10, 10 2020.

[154] S. Zahid, K. N. Whyte, E. L. Schwarz, et al., "Feasibility of using patient-specific models and the ???minimum cut??? algorithm to predict optimal ablation targets for left atrial flutter," *Heart Rhythm*, vol. 13, no. 8, pp. 1687–1698, 2016.

[155] N. Vandersickel, E. Van Nieuwenhuyse, N. Van Cleemput, et al., “Directed Networks as a Novel Way to Describe and Analyze Cardiac Excitation: Directed Graph Mapping,” *Frontiers in Physiology*, vol. 10, 9 2019.

List of publications and supervised theses

Journal Articles

- **Jorge Sánchez**, Juan F. Gomez, Laura Martinez-Mateu, Lucia Romero, Javier Saiz, Beatriz Trenor, *Heterogeneous Effects of Fibroblast-Myocyte Coupling in Different Regions of the Human Atria Under Conditions of Atrial Fibrillation*, Frontiers in Physiology 2019;10:847.
- **Jorge Sánchez**, Giorgio Luongo, Mark Nothstein, Laura Unger, Javier Saiz, Beatriz Trenor, Armin Luik, Olaf Dössel, Axel Loewe, *Using Machine Learning to Characterize Atrial Fibrotic Substrate from Intracardiac Signals using a Hybrid in silico and in vivo Dataset*, under review.
- Laura A Unger, Luca Azzolin, Mark Nothstein, **Jorge Sánchez**, Armin Luik, Gunnar Seemann, Srinath Yeshwant, Tobias Oesterlein, Olaf Dössel, Claus Schmitt, Peter Spector, Axel Loewe, *Cycle length statistics during human atrial fibrillation reveal refractory properties of the underlying substrate: a combined in silico and clinical test of concept study*, EP Europace, 2021;23:i133–i142.
- Mark Nothstein, Armin Luik, Amir Jadidi, **Jorge Sánchez**, Laura Anna Unger, Eike M Wülfers, Olaf Doessel, Gunnar Seemann, Claus Schmitt and Axel Loewe, *CVAR-Seg: An Automated Conduction Velocity and Amplitude Restitution Signal Segmentation Pipeline*, Accepted.

Refereed Conference Articles

- **Jorge Sánchez**, Beatriz Trénor, Javier Saiz, *In silico analysis of the effects of fibroblasts coupling to atrial myocytes under conditions of atrial fibrillation remodeling*, Computing in Cardiology (CinC) 2017
- **Jorge Sánchez**, Mark Nothstein, Laura Unger, Javier Saiz, Beatriz Trénor, Olaf Dössel, Axel Loewe,*Influence of Fibrotic Tissue Arrangement on Intracardiac Electrograms During Persistent Atrial Fibrillation*, Computing in Cardiology (CinC) 2019

- **Jorge Sánchez**, Mark Nothstein, Aurel Neic, Yung-Lin Huang, Anton J. Prassl, Jochen Klar, Robert Ulrich, Felix Bach, Philipp Zschumme, Michael Selzer, Gernot Plank, Edward Vigmond, Gunnar Seemann, Axel Loewe, *openCARP: An Open Sustainable Framework for in-silico Cardiac Electrophysiology Research*, Computing in Cardiology (CinC) 2020

Refereed Conference Abstracts

- **Jorge Sánchez**, Beatriz Trenor, Javier Saiz, Olaf Dössel, Axel Loewe, *In-silico adaptation of a myofibroblast electrophysiology model including intracellular calcium handling*, Deutsche Gesellschaft für Biomedizinische Technik (DGBMT) 2020

Conference Presentations

- **Jorge Sánchez**, Tiago Almeida, Diogo Soriano, André Ng, Beatriz Trénor, Javier Saiz, Armin Luik, Olaf Dössel, Axel Loewe, *Directed Graph Information Flow Mapping for Characterizing Cardiac Electrical Propagation from Unannotated Unipolar Electrograms*, Heart Rhythm Society (HRS) 2021
- **Jorge Sánchez**, Beatriz Trénor, Javier Saiz, *In silico analysis of the effects of fibroblasts coupling to atrial myocytes under conditions of atrial fibrillation remodeling*, Computing in Cardiology (CinC) 2017
- **Jorge Sánchez**, Mark Nothstein, Laura Unger, Javier Saiz, Beatriz Trénor, Olaf Dössel, Axel Loewe,*Influence of Fibrotic Tissue Arrangement on Intracardiac Electrograms During Persistent Atrial Fibrillation*, Computer in Cardiology (CinC) 2019
- Deborah Nairn, Daniel Hunyar, **Jorge Sánchez**, Olaf Dössel, Axel Loewe, *Impact of Electrode Size on Electrogram Voltage in Healthy and Diseased Tissue*, Computing in Cardiology (CinC) 2020
- **Jorge Sánchez**, Mark Nothstein, Aurel Neic, Yung-Lin Huang, Anton J. Prassl, Jochen Klar, Robert Ulrich, Felix Bach, Philipp Zschumme, Michael Selzer, Gernot Plank, Edward Vigmond, Gunnar Seemann, Axel Loewe, *openCARP: An Open Sustainable Framework for in-silico Cardiac Electrophysiology Research*, Computing in Cardiology (CinC) 2020
- **Jorge Sánchez**, Beatriz Trenor, Javier Saiz, Olaf Dössel, Axel Loewe, *In-silico adaptation of a myofibroblast electrophysiology model including intracellular calcium handling*, Deutsche Gesellschaft für Biomedizinische Technik (DGBMT) 2020
- **Jorge Sánchez**, Mark Nothstein, Aurel Neic, Yung-Lin Huang, Anton J. Prassl, Jochen Klar, Robert Ulrich, Felix Bach, Philipp Zschumme, Michael Selzer, Gernot Plank, Edward Vigmond, Gunnar Seemann, Axel Loewe, *openCARP: An Open Sustainable Framework for Cardiac Electrophysiology Research*, Virtual Physiology Human (VPH) 2020

- **Jorge Sánchez**, Beatriz Trenor. javier Saiz, *Estudio mediante Simulacion Computacional del Acoplamiento Eléctrico entre Miocitos Auriculares y Fibroblastos en Condiciones Fisiologicas y de Fibrilación Auricular Crónica*, CASEIB 2017
- **Jorge Sánchez**,Mark Nothstein, Laura Unger, Javier Saiz, Beatriz Trénor, Olaf Dössel, Axel Loewe, *Effect of the atrial fibrosis composition on the electrogram signal*, Atrial Signals 2019
- **Jorge Sánchez**, Beatriz Trenor, Javier Saiz, *Effects of fibrosis on atrial electrophysiology under chronic atrial fibrillation*, Atrial Signals 2017
- **Jorge Sánchez**, Beatriz Trenor, Javier Saiz, Olaf Dössel, Axel Loewe, *Influence of the fibrotic tissue arrangement during persistent atrial fibrillation*, Towards an integrated numerical heart model, Coupling the relevant physics the right way 2019
- **Jorge Sánchez**,Javier Saiz, Beatriz Trenor, *In Silico Analysis of the Effects of Fibroblasts Coupling to Atrial Myocytes Under Conditions of Atrial Fibrillation Remodeling*, Centro Nacional de Investigaciones Cardiovasculares Carlos III (CniC) 2017

Invited Talks

- **Jorge Sánchez**, *A detailed model of fibrotic tissue and corresponding electrograms*, Atrial Signals 2021

Supervised Student Theses

- Leonie Schicketanz, *Separation of atrial near and far field components in electrograms during atrial tachycardia*, Bachelor Thesis, Institute of Biomedical Engineering, Karlsruhe Institute of Technology (KIT), 2019
- Faten Bettaieb, *The effect of fibrosis transmurality on electrogram morphology and atrial fibrillation dynamics*, Bachelor Thesis, Institute of Biomedical Engineering, Karlsruhe Institute of Technology (KIT), 2020
- Tianbao Zheng, *Automatic patient-specific atrial model generation to study arrhythmia vulnerability*, Master Thesis, Institute of Biomedical Engineering, Karlsruhe Institute of Technology (KIT), 2021
- Pascual Tejero Cervera, *Source estimation of the cardiac fibrotic substrate from intracardiac signals*, Master Thesis, Institute of Biomedical Engineering, Karlsruhe Institute of Technology (KIT), 2021

Awards & Grants

- Networking Scholarship, Karlsruhe House of Young Scientists (KHYS), 2019
- Aspirant grant, Karlsruhe House of Young Scientists (KHYS), 2020
- Finalist Rosanna Degani Young Investigator Award, Computing in Cardiology (CinC), 2020
- Participation award, Virtual Physiology Human (VPH), 2020
- Summer school travel grant, Simula, 2020
- Cardiac electrophysiology summer school travel grant, Lyric Institute, 2019
- Image-based Biomedical Modeling summer school travel grant, University of Utah, 2017